

博士論文

**Study on the drilling process with the
hydraulic percussion rock drill**

(打撃式油圧さく岩機の穿孔過程に関する研究)

梁 英宗

Acknowledgements

This paper was completed with the help of many people. Firstly, I would like to show my great appreciation to my supervisor, Prof. Fukui, for his patient guidance and valuable advice on my study. Without his profound knowledge and sincere assistance I would not have quickly found my research.

I am also deeply grateful to Prof. Hashiba. He always took his precious time to instruct me how to carry out my research and to write a good paper. In addition, I appreciate him again for correcting mistakes and improving the contents of this dissertation. I would also like to give my thanks to Mr. Hatakeyama, who taught me how to operate the equipment in our laboratory and to Dr. Kataoka, who was very kind to give me valuable suggestions. I appreciate Mr. Yasukagawa for performing parts of numerical simulation concerning the study.

I would also like to express my gratitude to Mr. Koizumi, Mr. Matsuda and Mr. Hirano of Fukurawa Rock Drill Co., Ltd. for their valuable comments on this study.

I am also thankful to my friends who encouraged me to go on the study when I was in trouble. Finally, I would like to express my greatest thanks to my beloved parents and relatives who always support and encourage me no matter where I am.

Abstract

This doctoral dissertation has been performed at the University of Tokyo, Japan from October 2013 through November 2016. It is a cooperation research on improvement of hydraulic percussion rock drill between the Fukui Lab and the Furukawa Rock Drill Co., Ltd. The modern hydraulic rock drill has been continuously improved by many researchers and engineers and become more and more complicated. Development and modification of the rock drill based on test data are time-consuming and costly. In this study, it aims at constructing a new realistic numerical model of consecutive percussive drilling for further accurate improving the performance and efficiency of hydraulic rock drills. The new numerical model of consecutive percussive drilling was based on and modified from the Okubo-Nishimatsu's model. In particular, the aspects of the stress wave propagation in rods and rod joints as well as the bit-rock interaction were mainly improved in the study.

In Chapter 1, the background, problems existed in the modern hydraulic percussion rock drills, motivations, aims and outline of the study were introduced. Percussive drilling is an important process involved in mining, oil and water well drilling, and civil engineering. The performance and efficiency of the rock drill critically affect the construction speed and the cost. Thus, how to improve the performance by experimental and numerical methods has been focused by many researchers.

In Chapter 2, the basic knowledge and previous study concerning the percussive drilling were reviewed. The basic knowledge included the classification of drilling methods, the basic mechanism of the percussive drilling, as well as experimental and the two-point-strain measurement methods.

In Chapter 3, the aspects of stress wave generation, propagation and attenuation in the Okubo-Nishimatsu's model were improved. In the improved Okubo-Nishimatsu's model, the acoustic impedances of the piston, shank rod and rod were set to be consistent with their actual shape and size, as well as the rod joint was modeled as the CI +spring model. In addition, the 1D and axisymmetric finite element models of percussive drilling were built to calculate stress waves. The numerical waves calculated with both models were compared with the measured waves. It is shown that the numerical results calculated with the axisymmetric finite element model were better than those calculated with 1D theory of elastic waves on reproducing the

lateral-inertia effect but they were very close to each other. The numerical results of the axisymmetric finite element models were sensitive to the mesh scale and the time step size. A too small time step did not improve the simulation accuracy, but cause undesirable high-frequency vibrations in numerical results for the coarse-mesh scale. Thus, it is recommended to use the improved model for simulating stress wave propagation, that contribute to decreasing computational complexity and saving computational time.

In Chapter 4, the impact penetration behavior of the button-bit with the diameter of 64 mm on Inada granite was investigated. Single-blow-impact-penetration (SBIP) tests provided highly reproducible results under constant blow conditions and with tightening of the threads after each blow. Unnatural fluctuations appeared in the force-penetration curves calculated with the two-point-strain-measurement (TPSM) method. This is probably due to not only the differences in the rod stresses measured at the two points on the rod, but also to the mismatch between the actual bit and the calculation model. The data correction method was obtained, in which the bit force calculated in the Free-bit-end (FBE) test is subtracted from that in the SBIP test using a numerical simulation. The correction method was applied to the measured rod stresses, and the force-penetration curves were improved remarkably. However, the slopes of the curves changed unnaturally just before the peaks, which was probably due to the change in the contact conditions at the rod-bit connection in the SBIP and FBE tests. Thereafter, the bit force calculated in the simulation of the FBE test was subtracted from the bit force calculated from the measured rod stresses in the SBIP test when the bit force was high. The additional correction with threaded bit model is just for the threaded rod-bit connection used in this study. The corrected force-penetration curves are smoother in the SBIP tests than those in static penetration tests in previous studies, which indicate that impact penetration is not accompanied by large rock chipping. The variations in the force-penetration curves obtained from the more than 40 SBIP tests are probably caused by the contact conditions between the bit and rock, the rock properties and damage to the rock with each blow.

In Chapter 5, the impact penetration behavior of button bits into rock was investigated for modeling the bit-rock interaction under different rod-bit configurations. Impact penetration tests on Inada granite were carried out with six rod-bit configurations which were composed of four kinds of button bits and two kinds of rods. In the calculation of force-penetration curves from the measured rod strains, the bit model constructed from the acoustic impedances was simplified, and the empirical data correction method proposed in Chapter 4 was applied to all the rod-bit configurations. The

force-penetration curves for the six rod-bit configurations showed that the bit force in loading phase was approximately proportional to the square of the penetration. The curves in unloading phase had a linear relation between the bit force and the penetration. The final penetration of each blow had a linear relation with the maximum penetration, and the measured changes in borehole depth with each blow were proportional to the maximum penetration. The effect of rod diameter on the force-penetration curves was not clearly observed. However, the bit force corresponding to the same penetration increased and the specific energy decreased with the increase in bit diameter or in numbers of button tips on the bit.

In Chapter 6, the new consecutive percussive drilling model which was based on the 1D theory of elastic waves and modified from the Okubo-Nishimatsu's model was proposed. The aspects of the original model involved in stress wave generation, propagation and attenuation, as well as the bit-rock interaction were improved on the basis of the results of Chapters 3, 4 and 5. The variation in the force-penetration curves and the change in the borehole depth with each blow were also considered for reproducing the variable bit-rock contact condition during consecutive percussive drilling improvements. Any interest parameters can be constantly monitored and the p-v diagram can be accurately simulated. The new consecutive percussive drilling model will make it possible to evaluate the effect of thrust force and the effectiveness of the damper system on the bit-rock contact condition, because it can consider the change in the borehole depth while drilling.

Contents

Acknowledgements	i
Abstract	ii
Chapter 1 Introduction	1
1.1 Background	1
1.2 Problems in the hydraulic percussion rock drill	1
1.3 Motivations and aims.....	2
1.4 Outline of the dissertation.....	3
References	5
Chapter 2 Percussive drilling (Literature review)	6
2.1 History of percussive drilling	6
2.2 Rock drilling methods	6
2.3 Mechanism of top-hammer drilling.....	7
2.3.1 Stress wave propagation within rods	8
2.3.2 Stress wave attenuation at rod joints	9
2.3.3 Bit-rock interaction.....	10
2.4 Experimental studies of percussive drilling	12
2.4.1 Quasi-static penetration test.....	12
2.4.2 Stress wave propagation and dissipation test with rod joints	13
2.4.3 Percussive long-hole drilling test	13
2.4.4 Single-blow impact penetration (SBIP) test.....	15
2.4.5 Two-point strain measurement (TPSM) method.....	16
2.5 Numerical studies of percussive drilling	18
References	20
Chapter 3 Stress wave propagation in rods during percussive drilling	37
3.1 Introduction	37
3.2 Numerical models and methods.....	38
3.2.1 Improved model based on the 1D theory of elastic waves	38
3.2.2 Finite element method	39
3.2.3 1D finite element model of percussive drilling	40
3.2.4 Axisymmetric finite element model of percussive drilling	41
3.3 Numerical results	41
3.3.1 Calculated results of the improved model	41
3.3.2 Calculated results of the 1D finite element model.....	43
3.3.3 Calculated results of the axisymmetric finite element model.....	44
3.4 Discussion.....	45
3.5 Conclusions.....	46
References	48
Chapter 4 Force-penetration curves of a button bit generated during impact penetration into rock	67
4.1 Introduction	67

4.2 Problems in the calculation of a force-penetration curve	68
4.3 Consideration of the calculation method of a force-penetration curve with numerical simulation.....	70
4.4 Results and discussion of the SBIP tests	72
4.4.1 Force-penetration curves.....	72
4.4.2 Impact penetration behavior	74
4.5 Conclusions	75
References	77
Chapter 5 Effect of bit configuration in impact penetration tests with button bits	92
5.1 Introduction	92
5.2 Impact penetration tests with various rod-bit configurations	93
5.3 Simplified modeling method for button bits	93
5.4 Experimental results	94
5.5 Discussion.....	97
5.6 Conclusions	99
References	101
Chapter 6 Numerical simulation of consecutive percussive drilling	117
6.1 Introduction	117
6.2 Modeling of consecutive percussive drilling	117
6.2.1 Modeling of the rock drill body	118
6.2.2 Modeling of the piston	118
6.2.3 Modeling of the shank rod, rod and the bit.....	118
6.2.4 Modeling of the bit-rock interaction.....	119
6.2.5 Modeling of the variation in force-penetration curves with blows..	120
6.2.6 Modeling of the change u_b in the borehole depth with each blow .	121
6.3 Calculation conditions and procedures.....	122
6.4 Calculation results	122
6.5 Conclusions.....	124
References	125
Chapter 7 Conclusions.....	143
7.1 Conclusions.....	143
7.2 Future work.....	145

Chapter 1 Introduction

1.1 Background

Percussive drilling has been extensively used to drill holes for blasting or rock bolting in open pit mines, quarries and construction sites. It is also used to drill sounding holes in the advance of a tunnel front, which is an effective way to reduce operational risks and avoid unexpected rock problems (Schunnesson 1996). Percussive drilling (even without rotary) has potential to provide faster penetration rate than conventional rotary drilling or diamond drilling, especially in some hard formations such as granite, sandstone, limestone, dolomite, etc. (Whiteley and England 1985; Pratt 1987; Melamed et al. 2000). However, there are many unknowns needed to be solved for further improving the efficiency and penetration rate of percussive drilling.

1.2 Problems in the hydraulic percussion rock drill

The main components involved in percussive drilling with a hydraulic rock drill, top-hammer drilling, are a rock drill body, a piston, a shank rod, rods, rod joints, a bit and a rock. The components mutually affect each other and self-induced oscillation occurs. The piston in the rock drill body is reciprocated by hydraulic pressure and repeatedly impacts on the shank rod a few thousand times per minute. Stress waves generated by the impact of the piston on the shank rod propagate and attenuate in the rods and rod joints, and then arrive at the bit-rock interface. The compressive stress wave corresponds to a bit force between the bit and the rock. Once the bit force exceeds a certain value, the rock begins to break and debris is created around and below the bit. The debris is flushed out of the borehole by a flushing fluid delivered to the bit via an axial hole through the rods. After each blow, the rods are rotated a certain angle in order to turn the bit over the hole bottom so that the entire surface can be worked on by the button tips. The detail of the basic mechanism of the percussive drilling will be introduced in Chapter 2.

The movement direction of the piston is determined by the relative position between the piston and the rock drill body. The impact velocity of the piston is affected by percussive pressure and hydraulic circuits, which adjust the length of the piston stroke. If the waves reflected from the bit propagate into the piston when the piston is in contact with the shank rod, the return velocity of the piston will increase and result in the impact velocity of the piston in the next blow increases and further change the blow frequency. Fukui et al. (2007) reported that the blow frequency of the piston increased 7

percent.

The total length of the drilling system is about 5 m. The velocity of elastic waves in a steel rod is almost 5 km/s. The shuffle time is about 2 ms. The interval between two adjacent blows is 15 ~ 40 ms. The waves implement about 10 round trips before the next waves come. If there is no damping system, the vibration caused by the reflected waves will continue and the collision position between the piston and the shank rod will change.

The bit-rock contact condition is mainly affected by the thrust force from the rock drill body, and varies with the vibration of the drill string, which is caused by the reflected wave from the bit. In addition, the bit-rock contact position varies with the bit rotation. Thus, it is difficult to achieve a stable drilling process and results in low drilling efficiency. For instance, in the case when the bit is not in contact with the rock, the incident compression wave is reflected from the free bit end as a tension wave with the whole percussive energy, which results in low drilling efficiency. It is also likely that the incident compression wave drives the bit to move forward and then contact with the rock, which causes a complicated reflected wave consisting of tension wave and compression wave. If the reflected wave as a tension wave passes through the sleeve, the threads of the sleeve will suffer high temperature and easily be broken (Mikami 1986).

Previous studies pointed out there exists a most appropriate thrust force. The penetration rate tends to increase with the increase in thrust before the thrust arrives the appropriate value. Once the thrust force increases over the appropriate value, abrasion in accessories become severe and accessories are destroyed. It is necessary to set the thrust force to the appropriate value. However, the value varies with the bit-rock contact condition during the drilling process (Hustrulid and Fairhurst 1971). A damper system was developed in order to solve the problem. Most of the reflected wave from the bit is absorbed by the damper system. As a result, the vibration of the drilling string is reduced. Moreover, the bit-rock contact condition is improved by the variable thrust which is adjusted by the damper system. The drilling efficiency is getting better. However, it is also needed to be considered how to set an appropriate damper system depending on the bit-rock contact condition, because the essential mechanism of the damper system absorbs the vibration energy. Too much enhance the absorbing effect of the damper system will decrease the drilling efficiency.

1.3 Motivations and aims

The efficiency and penetration rate of blast hole drilling with the hydraulic

percussion rock drills significantly affect the speed and cost of tunnels and underground excavations. In the case of a tunnel advance, generally, about 30 percent of the construction time is used for drilling several tens to one hundred and several tens of blast holes. The use of hydraulic percussion rock drills with a good penetration rate can achieve a fast tunnel advance rate. Meanwhile, the total costs consist of labor costs and various rental fees. Most of them are proportional to the time. That is, shortening the construction time can achieve cost reduction.

Performance improvements of the hydraulic percussion rock drill based on test data are time-consuming and costly. Hence it is essential to make effective use of numerical simulation. However, most of the numerical models proposed in previous studies were too simple in comparison with the actual drilling process with a hydraulic percussion rock drill. The aim of the study is to construct a new numerical model for consecutive percussive drilling, which is based on the previous Okubo-Nishimatsu's model (Okubo and Nishimatsu, 1991) and much more realistic than it.

1.4 Outline of the dissertation

This dissertation consists of seven chapters.

In Chapter 1, the introduction was described as well as a basic knowledge of percussive drilling, the research purpose and composition of this research.

In Chapter 2, the mechanism of the percussive drilling with a hydraulic rock drill was introduced in detail. Related previous studies and experimental methods were reviewed.

In Chapter 3, an improved numerical model based on the theory of one-dimensional elastic waves and modified from the Okubo-Nishimatsu's model was proposed. Compared to the Okubo-Nishimatsu's model, the acoustic impedance of the piston, shank rod and rod was set to the same values as actual products and a new numerical model for a sleeve-type rod joint was combined into the improved model. In addition, numeral models based on one- and three-dimensional finite element method for simulating the stress wave propagation in rods and rod joints during percussive drilling were also constructed. The calculated waves with these numerical models were compared to each other and to the measured wave in impact penetration tests performed by Fukui et al. (2007, 2010).

In Chapter 4, the impact penetration behavior of a button bit with a diameter of 64 mm was investigated by means of laboratory tests. The

force-penetration curves were calculated from the measured rod strains with the two-point strain measurement (TPSM) method. However, unnatural fluctuations were observed in the curves. Thereafter the reason for this was elucidated, and a data correction method was proposed using a numerical simulation. The force-penetration curves of the impact penetration tests with the button bit were accurately calculated with the correction method.

In Chapter 5, to evaluate the data correction method proposed in Chapter 4, it is extended to calculate force-penetration curves of the single blow impact penetration (SBIP) tests with other rod-bit configurations. In the calculation of force-penetration curves from the measured rod strains, the bit model constructed from the acoustic impedance was simplified. Based on the obtained force-penetration curves for all rod-bit configurations, the effects of shape of rod and bit (e.g., rod diameter, bit diameter) on the impact penetration behavior of button bits was discussed. A new numerical bit-rock interaction model for the button bits penetration into Inada granite was proposed.

In Chapter 6, a new consecutive percussive drilling model was proposed, which was based on the 1D theory of elastic waves and modified from the Okubo-Nishimatsu's model. Compared to the Okubo-Nishimatsu's model, the aspects of the stress wave propagation in rods and rod joints and the bit-rock interaction were improved based on the results of Chapters 3, 4 and 5. The variation in the bit-rock contact condition with each blow during consecutive percussive drilling was modeled and combined into the new model to make the simulation as close as possible to the actual drilling conditions.

In Chapter 7, the conclusions from each chapter and the future work are summarized.

References

Fukui K., Abe H., Koizumi M., Tomosada H., Okubo S. (2007): Attenuation of rod stress in percussive long-hole drilling, J. of MMIJ, vol. 123, pp. 152-157 (in Japanese).

Fukui K., Okubo S., Koizumi M., Shioda A., Matsuda T., Fukuda S. (2010): Force-penetration curves with a button bit in the percussive drilling. J. of MMIJ, vol. 126, pp. 512-518 (in Japanese).

Hustrulid W. A., Fairhurst C. (1972): A theoretical and experimental study of the percussive drilling of rock part IV - application of the model to actual percussion drilling, Int. J. of Rock Mech. Min. Sci., vol. 9, pp. 431-449.

Melamed Y., Kiselev A., Dreesen D., Blacic J. (2000): Hydraulic hammer drilling technology: developments and capabilities, Journal of Energy Resources Technology, vol. 122, pp. 1-7.

Mikami Y. (1986): Studies on the sleeve heating of rock drill, doctoral dissertation, the University of Tokyo (in Japanese).

Okubo S., Nishimatsu Y. (1991): Computer simulation of percussive drilling, J. of MMIJ, vol. 107, pp. 209-214 (in Japanese).

Pratt C. A. (1987): Modifications to and experience with percussion air drilling, SPE/IADC Drilling Conference, 16166, pp. 15-18.

Schunnesson H. (1996): RQD predictions based on drill performance parameters. Tunneling and Underground Space Technology, vol. 11, pp. 345-351.

Whiteley M. C., England W. P. (1985): Air drilling operations improved by percussion-bit/hammer-tool tandem, SPE/IADC Drilling Conference, Society of Petroleum Engineers.

Chapter 2 Percussive drilling (Literature review)

2.1 History of percussive drilling

Percussive drilling was first developed by the Chinese more than 4,000 years ago, and in its early stage entailed raising and dropping a heavy piercing tool to cut and loosen earth material. A cutting head was secured to bamboo rods, which were linked together to drill to 3,000-foot (915 m) depths. The raising and dropping of the bamboo drill string allowed it to impact and fracture the less dense rock formations. It was reported to always take two to three generations of workers to complete large wells (Treadway 1997). The earliest stream-driven rock drill was invented by Richard Trevithick in 1813 (Weston 1910) for drilling in limestone. In 1849, J. J. Couch, American inventor, made the first percussion rock drill, which was powered by steam. In 1866, pneumatic rock drill of which hammer was driven by compressed air became practical. In the late 1880s, C. H. Shaw devised a hammer drill in which the piston was separated from the rod and hammered it each cycle, thereby increasing the blow frequency and the penetration rate.

In 1897, J. G. Leyner patented a hollow rod through which air was pumped and flushed out the cuttings. Then, water soon replaced air, which reduced the dust. In the 1940s, drill rods with sintered tungsten carbides bits came onto the market, which had a profound effect on the logistics of hard rock drilling. In the early 1970s, the French firm of Montabert developed the first working hydraulic percussive rock drills and took the lead in producing and marketing the hydraulic drills. Since the 1980s, percussive drilling also gained more and more interests in oil and gas industries with increasing potential in hard rock formations. However, poor understanding of drilling fundamentals and economical uncertainties greatly jeopardize the acceptance of percussive drilling technology into oil and gas industries.

2.2 Rock drilling methods

Fig. 2.1 shows the rock drilling methods, which are mainly divided into two types—rotary drilling and rotary percussive drilling. Both of them are used in mining, oil and water well drilling and civil engineering, etc.

Fig. 2.1 (a) shows the rotary drilling of which bit is rotated in the hole by a drilling column driven from a rotary table on the surface. Commonly, it is applied to drill holes with diameters larger than 152 mm, and the deeper the hole, the more applicable the method. It is subdivided into rotary cutting and rotary crushing. Rotary cutting creates a hole by shear forces and breaks the rock's tensile strength, while rotary crushing breaks the rock by high point

load accomplished by a toothed bit which is pushed downwards with high force (Fernberg 2008).

Rotary percussive drilling breaks a rock by repeated impacts transferred from a rock drill to a bit at the bottom of the hole. Compared to the rotary drilling, the rotary percussive drilling is used to drill small to medium diameter holes in all kind of rocks for both surface and underground (Haq 2010). The rotary percussive drilling is also classified into two large groups depending upon where the piston is mounted.

Fig. 2.1 (b) shows the top hammer drilling of which rock drill is mounted on a crawler or a jumbo and indirectly connected with a bit through rods and rod joints (Jimeno et al. 1995). The rods (see Fig. 2.2) transfer both the impact energy and the rotation to the bit (see Fig. 2.3). With an increase in the borehole depth, the rods are coupling to each other by rod joints (see

Fig. 2.4). One weakness with the drilling system is that it is limited by drilling depth. Because almost 10 % of the impact energy is lost by one rod joint (Fukui et al. 2007).

Fig. 2.1 (c) illustrates the down-the-hole (DTH) drilling of which rock drill is indirectly connected to a bit. The rock drill is piston shape mounted in a cylinder, which is pushed down to the bottom of the hole. The bit rotation is performed by a rotation unit located outside the hole. The rotation is transferred by pipes, to which the rock drill is connected. The advantage of the DTH drilling is that there is no power loss caused by rod joints, thus no need to worry about the power loss with the borehole depth. The DTH's greatest disadvantage is corrosion so it must be kept well lubricated at all times. The DTH drilling is used for drilling holes with diameters larger than 120 mm.

2.3 Mechanism of top-hammer drilling

In this study, the drilling process with the hydraulic percussion rock drill which will be discussed later is the top-hammer drilling. The top-hammer drilling system is mainly composed of a rock drill body, rods and rod joints, and a bit. The rock drill body generates elastic stress waves, rods and rod joints transfer and attenuate the waves, and a bit transmits the stress wave energy to rock. The mechanism of the drilling system is divided into four actions: percussion, rotation, thrust force, and flushing;

Percussion of the piston generates stress waves in the drilling process with a hydraulic rock drill. The kinetic energy of the piston is transmitted to the bit, through the rods and rod joints in the form of stress waves. When the waves

reach the bit, part of the kinetic energy is transformed into work, part radiates into the rock, and the rest is reflected from the bit and returns to rods. The work performed on the rock goes into new surface energy, elastic strain energy, kinetic energy, heat and other forms of energy, in proportions that vary during the bit-rock interaction (Lundberg and Collet 2010).

Rotation turns the bit between consecutive blows so that the bit can impact on different positions of the rock in the bottom of the borehole. There exists an optimum rotational speed which produces large-sized cuttings for each rock type. Thus, the rotational speed needs to be set to suit the rock hardness of the rock.

Thrust force is supplied by a motor in order to ensure the bit in permanent contact with the rock. The size of the thrust force should match the rock and bit types because insufficient or excessive thrust force can lead to negative effects. In the case of the insufficient thrust force, the penetration rate drops down while wears on rods and rod joints are intensified and the rod thread are loosened and heated. In the case of the excessive thrust force, the penetration rate decreases while the rotation resistance increases, which leads to the rod be jammed, wear on the bit and vibration on the equipment be increased, and causes boreholes to be deviated (Jimeno et al. 1995).

Flushing is used to clear the rock debris from the borehole. If evacuating drill cutting not maintaining the clean by as soon as they appear, a large quantity of energy will be consumed in regrinding. Borehole flushing is carried out with a flow of air, water or foam that is injected by pressure to the bottom through an opening in the center of the rod and flushing holes in the bit. Air flushing is used for surface drilling while water flushing for underground drilling.

2.3.1 Stress wave propagation within rods

Fig. 2.5 shows that the kinetic energy of the piston is transmitted to the bit through the rods and the rod joints, in the form of elastic waves. Fig. 2.5 (a) shows stress wave propagation in rod after the impact of the piston on the rod end. The piston and the rod are simplified as two simple circular cylinders, which have uniform cross-sectional area and acoustics impedance. Initially, the left end of the rod is static. In Fig. 2.5 (b), the wave has already transmitted to the bit end. In the case of a free end, the compressive incident wave reflects as a tension wave. The stress state of the overlapped part of the incident and reflected waves is zero, and the particle velocity of the overlapped part is doubled and equal to the impact velocity of the piston. The advancement Δd of the bit is calculated as follows;

$$\Delta d = 2 \times 2l_p \times \varepsilon = 4l_p \frac{\sigma}{E} \quad (2.1)$$

where ε and σ are stress and strain, respectively. l_p is the length of the piston and E is Young's modulus. Thus, the wavelength of the compressive incident wave is $2l_p$ and the length of the compressed portion is $2l_p \times \varepsilon$. The elongation, that is, the advancement Δd of the bit, is the double length of compressed portion.

Fig. 2.5 (c) illustrates the stress waves reflect from soft and hard rocks, respectively. At the beginning, there exists a gap between the bit and the rock. When the advancement Δd of the bit is less than the size of the gap g , the energy completely reflects from the bit as tensile waves. The stress wave energy converts into crushing work with the bit penetration into rock. However, in the case of hard rock, it is difficult for the bit to penetrate into rock due to the large resistance from the rock, thus, the energy almost reflects from the bit as compressive wave.

It can be seen that the performance and efficiency of the rock drill are affected by the shape of the stress wave and by the bit-rock contact condition. In actual percussive drilling, the wave is more complicated than the above one. Dutta (1968) used a computer code to determine the shape of the stress wave produced by a percussive piston of complex geometry. Chiang and Elias (2008) modeled the impact of the piston on the bit and the rock fragmentation caused by the bit penetration into rock with three-dimensional isoparametric elements. They also investigated the effect of the complex piston geometry on percussive drilling.

2.3.2 Stress wave attenuation at rod joints

In percussive long-hole drilling with a hydraulic percussion rock drill, rods are jointed to each other by rod joints at their ends. A sleeve-type rod joint is a coupling sleeve (CS) with internal thread into which the threaded ends of the rods are screwed in end-to-end contact with each other. The schematic illustration of the rod joint is shown Fig. 2.6 (a). There are two major ways in which the rod joints may reduce the energy transfer efficiency, namely reflection and dissipation of stress wave energy. Reflection occurs due to the geometrical changes at the rod joints relative to the uniform rods. Dissipation is due to friction and relative slip of the threads of the rod joints.

There are various numerical models for modeling the rod joint. Fischer (1959) represented the rod joint as a swell on a one-dimensional elastic rod (characteristic impedance or CI model) shown in Fig. 2.6 (b). As shown in Fig. 2.6 (c), Lundberg (1973) represented the rod joint as a rigid mass

between one-dimensional elastic rods (rigid mass or RM model). However, the CI and RM models for a sleeve-type rod joint have several shortcomings. Some of these are the following: (i) they do not allow for axial mobility of the rod joint relative to the rods and therefore predict no dissipation. (ii) Because of their linearity they predict no dependence of relative energy transmission on incident wave amplitude. (iii) They do not allow for joint preload. In spite of these defects, the CI and RM models are able to predict energy transmission with fair accuracy under conditions which may prevail in percussive drilling (Lundberg et al. 1989). Beccu and Lundberg (1990) clarified that the efficiency along the axis-direction of energy transmission increased and energy dissipation decreased when the length of the hammer varied from relatively short to relatively long and that the efficiency of the percussive drilling process decreased with the number of joints but depends little on the joint preload. Okubo et al. (1994) also investigated the effect of the preload on the efficiency of energy transmission, and found the amplitude of the reflected waves decreases with preload of the sleeve.

As shown in Fig. 2.6 (d), Hayamizu (1974) proposed a model which consists of a rigid mass and dashpots for the rod joint with consideration of energy dissipation. On the basis of experimental observations, Lundberg et al. (1989) established a nonlinear dissipative spring (NDSM) model. The NDSM model is illustrated in Fig. 2.6 (e). The rod joint was represented by a rigid mass and the coupling through the threads between the rod joint and the rods was represented by an aggregate of springs and a friction element. Okubo et al. (1994) proposed a spring model for the rod joint. The spring model of the rod joint is illustrated in Fig. 2.6 (f). In this study, a model combining the CI model with the spring model are illustrated in Fig. 2.6 (g).

2.3.3 Bit-rock interaction

The rock behavior under percussive drilling is a complex problem because of its non-linearity, and because the bit-rock contact condition is also complex (Shah and Wong 1997). In practical application the experimentally obtained force-penetration curve is used to represent characteristics of bit-rock interaction in percussive drilling for any different bit-rock combinations. However it is difficult to directly measure the instantaneous penetration and the bit force during the percussive drilling. Fairhurst (1961) indirectly measured the incident and reflected waves on a hammer drilling system by strain gauges, and derives the force-penetration characteristic based on the fact that the resultant force on the bit must equal the force on the rock, that is,

$$A(\sigma_i + \sigma_r) = F \quad (2.2)$$

where A is the cross-sectional area of the bit, and σ_i and σ_r are the incident and reflected stress waves, respectively. Besides that, if the bit is assumed to be initially stationary, the velocity v_b of the bit can be obtained by

$$\frac{c}{E}(\sigma_i - \sigma_r) = v_b \quad (2.3)$$

where E is the Young's modulus and c is the elastic wave speed.

In the study of Fairhurst (1961), the strain was only measured at one cross-section, which resulted in the gauges could not be attached too close to the bit end in order to ensure the incident and reflected waves do not overlap each other at the measurement point. Yanagihara (1977), and Lundberg and Henchoz (1977) improved the measurement method with adding another measurement point. The restriction disappears once the strains are measured at two cross-sections: the waves do not need to be separated while measuring, since they can be separated in the analysis of the measured strains. The method is called the two-point strain measurement (TPSM) method, which will be later discussed in Chapters 4 and 5. The original TPSM method was used for uniform rods (Lundberg and Henchoz 1997) and further extended for non-uniform rods (Lundberg et al. 1990). Carlsson et al. (1990) used the method to calculate the force-penetration curve in a DTH drilling system.

The force-penetration curve measured in the single-blow impact penetration was shown in Fig. 4.3 of Chapter 4 with the blue color. It shows that the curve consists of two successive phases, one associated with the loading and the other with the unloading. In previous studies (Lundberg 1982; Karlsson et al. 1989; Lundberg and Okrouhlik 2001; Chiang and Elias 2008; Saksala 2011, 2013; Depouhon et al. 2015), the curve was simplified as a bilinear model shown in Fig. 2.7 and expressed as the following mathematical equation:

$$F = \begin{cases} Ku & \text{for loading} \\ F_{max} - \gamma K(u_{max} - u) & \text{for unloading} \end{cases} \quad (2.4)$$

where K is the penetration resistance and γ is the unloading rate constant. The value of γ is between 0 and 1. $\gamma = 0$ corresponds to completely inelastic behavior of the rock while $\gamma = 1$ corresponds to completely elastic behavior. The total work done on the rock W_R is calculated by

$$W_R = W_L - W_U \quad (2.5)$$

where W_L is the work done during the loading phase, and W_U is the energy returned to the rock drill during the unloading phase. W_U is found by

$$W_U = \gamma W_L \quad (2.6)$$

Stephenson (1963) and Ajibose (2009) pointed out the force-penetration curve is rate-independent, that is, it does not significantly depend on the impact velocity of the bit in the range of velocities spanned in percussive drilling. However, the experimental result of Okubo et al. (1992) reported that the slope of the force-penetration curve in impact penetration test is larger than that in quasi-static penetration test.

2.4 Experimental studies of percussive drilling

As mentioned above, many factors, including hydraulic pressure, thrust force, number of the rods, design of the bit, and mechanical properties of the rock, have remarkable influence on the efficiency of the percussive drilling. In this section, common experimental studies relevant to percussive drilling are reviewed. These experimental studies include two kinds of impact penetration tests, percussive long-hole drilling test and single-blow impact penetration (SBIP) test that are performed by Fukui et al. (2007, 2010), will be discussed in detail, because the measured results in the tests were used to build and validate numerical models of percussive drilling in this study. In Chapter 3, the rod stresses measured in the percussive long-hole drilling test with the HD 210 hydraulic percussion rock drill are used to determine the best parameter values of numerical models. The rod stresses measured in the single blow impact penetration (SBIP) test with the HD712 hydraulic percussion rock drill are used to check whether the values of parameters of the numerical model have universal nature. In Chapters 4 and 5, the rod stresses measured in the SBIP tests are used for calculation of force-penetration with the two-point strain measurement (TPSM) method.

2.4.1 Quasi-static penetration test

Quasi-static penetration test is to study rock deformation and fracture mechanism under different bits. Figs. 2.8 (a) and (b) show the schematic illustrations of the quasi-static penetration test and the impact penetration test used in Okubo et al. (1992). A one-button bit with a radius of 7 mm and nine rocks were used in the study. The difference between force-penetration curves derived from the impact penetration test and those derived from the quasi-static penetration test was observed and formulated as follows:

$$K_d \approx 1.2K_s \quad (2.7)$$

where K_d and K_s are the slopes of force-penetration curves in impact penetration test and in quasi-static penetration test, respectively.

2.4.2 Stress wave propagation and dissipation test with rod joints

The transmission and dissipation behavior of stress waves is a critical factor in percussive long-hole drilling. Stress wave transmission and dissipation test is a traditional experimental method to study on the transmission and dissipation behavior of stress waves when the waves travel through rod joints. Fig. 2.9(a) and (b) show the schematics of the tests with a hammer and with a rock drill, respectively. In Fig. 2.9, two rods are coupled to each other by a sleeve-type rod joint with internal threads into which their threaded ends are screwed in end-to-end contact with each other.

2.4.3 Percussive long-hole drilling test

Percussive long-hole drilling test as a field test was very close to the actual percussive drilling and had an advantage on controlling drilling conditions (Fukui et al. 2007). Fig. 2.10 (a) shows the overall view of the percussive long-hole drilling test, and Table 2.1 lists the used components in this test. The HD210 hydraulic percussion rock drill manufactured by Furukawa Rock Drill Co., Ltd. The piston, which is 600 mm in length, with maximum and minimum diameters of 52 mm and 38 mm, respectively, is reciprocated by hydraulic pressure. The shank rod, which is 430 mm in length, with maximum and minimum diameters of 60 mm and 41 mm, respectively, has splines for rotation at its end. The shank rod is a hollow tubular structure, except for the portion of the splines. The rod joint is a sleeve type with a T38 thread, which is 190 mm in length and 55 mm in outer diameter. The extension rod is a hollow cylinder, 3660 mm in length, with outer and inner diameters of 39 mm and 14.3 mm, respectively. The connection between the rod and bit is a T38 thread. Ten carbide button tips are embedded in the bit; four of which are face tips 9 mm in diameter, while the other six are gauge tips 11 mm in diameter. The bit, including the tips, is 64 mm in nominal diameter and 136 mm in length.

As shown in Fig. 2.10 (b), the HD210 hydraulic percussion rock drill has a damper system composed of a damping piston and a pushing piston. The thrust force was applied to rods through the pushing piston which was driven by the hydraulic pressure (damper pressure). The vibration of the rock drill body caused by stress waves reflected from the bit end was reduced with the aid of the absorption of the damping piston.

Rods were passed through predrilled holes with the diameter of 64mm in

Inada granite blocks to avoid bending. The distance between two rock blocks was equal to the length of a rod, thus a sleeve can be mounted between the two blocks. The overall length of the drilling string system varied from one-rod length (3.66 m) to ten-rod length (36.6 m) with the increase of the number of rods. Two kinds of the thrust pressure, 10 MPa and 12 MPa, were used. The percussive long-hole drilling test was carried out under 20 different kinds of experimental conditions.

Rod stresses were measured by strain gauges (KFG-2-120-D16, manufactured by Kyowa Electronic Instruments Co., Ltd.). The gauges were attached at two locations: one was 50 cm from the front end of the shank rod and the other one was 50 cm from the back end of the bit. When only one rod was used, only one location was select to measure by one strain gauge. While when more than 3 rods were used, two strain gauges were attached on the first and last rods, respectively. Other rods were inserted between them. To cancel out the bending strain, two strain gauges were attached on opposite sides of each point in the longitudinal direction of the rod. The gauges were directly connected to cables without using gauge terminals through a trial-and-error process. The part of the cable near the gauges was fixed on the rods by instant glue. The cables were easily cut during rotary percussive drilling so they were wrapped around the rod 30 turns in advance. The duration time was 25 s from rewinding 30 turns to winding 30 turns again with the rotational speed of 142 rpm. It was enough to measure strain of 10 s. Durable normal gauges were chosen because the noise in the signal was relatively low. An alternative measurement method with an accelerometer was not adopted because it is easily broken.

The hydraulic pressures (operating pressure, rotary pressure, and damper pressure) were measure with a flush diaphragm pressure transducer (Type PWF-50MPA, manufactured by Tokyo Sokki Kenkyujo Co., Ltd). The displacement of the rear end of the rock drill was measured with a laser displacement meter (3Z4M-S22, manufactured by Omron Corporation). The rate of penetration (ROP) is equal to dividing the displacement by the percussive time. All data were recorded with a data logger (Type 8826, manufactured by Hioki E. E. Corporation). The strain was recorded at a sampling frequency of 1 MHz, while other parameters at a sampling frequency of 10 kHz.

To coordinate with the operating pressure, the thrust was adjusted to 8 kN through a thrust cylinder. The average operating pressure was adjusted to 15 MPa, which was lower than that in the actual percussive drilling. The oil quantity delivered by a hydraulic motor was adjusted to ensure the rotational speed of 142 rpm. The average damper pressure was set to 10 MPa, or 12 MPa

for keeping a balance between the thrusts of the drill body and damper.

2.4.4 Single-blow impact penetration (SBIP) test

The single-blow impact penetration (SBIP) test is a special laboratory test of which test conditions are carefully controlled to implement only one impact of the piston on the rock for the rock drill. With the aid of the SBIP test, the performance comparison among different specifications of a component in the rock drill under the same drilling conditions can be accurately implemented.

Fig. 2.11 shows the impact penetration tester, and Table 2.2 lists the used components in this test. The tester consists of the same piston, shank rod, rod joint, extension rod and bit as used in an actual rock drill manufactured by Furukawa Rock Drill Co., Ltd. All the components are replaceable. The piston, which is 710 mm in length, with maximum and minimum diameters of 52 mm and 36 mm, respectively, is reciprocated by hydraulic pressure. The shank rod, which is 790 mm in length, with maximum and minimum diameters of 51 mm and 31 mm, respectively, has splines for rotation at its end. The shank rod is a hollow tubular structure, except for the portion of the splines. The rod joint is a sleeve type with a T38 thread, which is 190 mm in length and 55 mm in outer diameter. The extension rod is a hollow cylinder, 3660 mm in length, with outer and inner diameters of 39 mm and 14.3 mm, respectively. The connection between the rod and bit is a T38 thread. Twelve carbide button tips are embedded in the bit; four of which are face tips 10 mm in diameter, while the other eight are gauge tips 11 mm in diameter. The bit, including the tips, is 64 mm in nominal diameter and 136 mm in length.

As shown in Fig. 2.11 (b), strain gauges for steel (KFG-2-120-D16, manufactured by Kyowa Electronic Instruments Co., Ltd.) were attached at two points: *A* and *B* on the rod. Point *A* is 1000 mm from the back end of the rod, and point *B* is 750 mm from the front end of the rod. To cancel out the bending strain, two strain gauges were attached on opposite sides of each point in the longitudinal direction of the rod. Strain was recorded at a sampling frequency of 1 MHz on a data logger (Type 8826, manufactured by Hioki E. E. Corporation), through a strain amplifier (CDV-230C, manufactured by Kyowa Electronic Instruments Co., Ltd). The gauge factors of the strain gauges were calibrated by statically loading the rod before the tests.

The components from the shank rod to the bit are rotated in percussive drilling. To obtain force-penetration curves in rotary percussive drilling, it is necessary to measure rod stress with the cables from the strain gauges wrapped around the rod by a few dozen turns. However, these cables are

easily cut during the test. Moreover, in rotary percussive drilling, torsional stress is included in the rod stress, which is one of the error factors in measurement. To overcome these shortcomings in this study, the components from the shank rod to the bit were rotated 25.7° , which is $1/14$ rotation, by hand after each penetration.

The testing procedure is as follows;

- 1) The piston collides with the shank rod and the bit penetrates into rock, which is called a single-blow impact penetration (SBIP) test.
- 2) Rock debris is removed.
- 3) The threads of the rod joint and the bit are tightened.
- 4) The components from the shank rod to the bit are rotated 25.7° .
- 5) Thrust force is loaded via the thrust cylinder.
- 6) Return to 1).

The hydraulic pressure used to move the piston was set to 15 MPa, at which pressure the piston velocity was 10.4 m/s just prior to collision with the shank rod. The tightening torque was set to 500 Nm, and the thrust force was set to 2.5 kN.

A block of Inada granite obtained in Ibaraki Prefecture, Japan, was used in the tests. The uniaxial compressive strength and Young's modulus of the granite were 148 MPa and 51.4 GPa, respectively. The block was held in place with steel jigs so that it would not move during the tests. The measured displacement of the block during the test was less than 0.02 mm, which was negligible compared with the penetration of the bit. The tests were started with the bit in the borehole, which had been drilled beforehand. The SBIP test was repeated 42 times.

2.4.5 Two-point strain measurement (TPSM) method

Bit force and penetration in percussive drilling have been calculated from the strain measured at one or two cross-sections of the rod. When the strain is only measured at one cross-section, there is a limitation for the bit length in order to avoid incident and reflected waves overlapping each other at the measurement point. When the strain is measured at two cross-sections, there is no such restriction. The method measured strain at two cross-sections of the rod is called the two-point strain measurement (TPSM) method and is reviewed in the following.

As shown in Fig. 2.12 (a), the rod and bit are subdivided into the same elements in length, and numbers are assigned from point *A*. $Z(i)$ is the average acoustic impedance (= average cross-sectional area \times Young's modulus/elastic wave velocity) of the *i*-th element. $p(t,i)$ and $n(t,i)$ are the

average forces with the elastic waves to the bit (rightward) and to the shank rod (leftward), respectively, in the i -th element at the time t . The forces are positive in tension.

In the tester shown in Fig. 2.11 (b), the distance between point B , the i_B -th element, and the bit end is not long enough in comparison with the wave length. Therefore the combination of p and n is measured at B , and this needs to be separated into p and n . If the elastic wave is assumed not to attenuate from A to B , the following formulae are obtained:

$$p(t, i_B) + n(t, i_B) = S\sigma_B(t) \quad (2.8a)$$

$$-p(t - 2t_{AB}, i_B) + n(t - 2t_{AB}, i_B) = 0 \quad (t < 2t_{AB}) \quad (2.8b)$$

$$\begin{aligned} -p(t, i_B) + n(t, i_B) &= -p(t - 2t_{AB}, i_B) + n(t - 2t_{AB}, i_B) \\ &+ S\sigma_B(t) + S\sigma_B(t - 2t_{AB}) - 2S\sigma_A(t - t_{AB}) \quad (t \geq 2t_{AB}) \end{aligned} \quad (2.8c)$$

where S is the cross-sectional area of the rod, and t_{AB} is the wave propagation time from A to B . The stresses σ_A at A and σ_B at B are calculated by multiplying the measured strains by Young's modulus, and therefore Eq. (2.8c) is calculated serially. Separated p and n at B are obtained as the solutions to the simultaneous equations of Eqs. (2.8a), (2.8b) and (2.8c). If the distance between point B and the bit end is long enough in comparison with the wave length, p and n at B are measured separately, and the other measurement point and the calculation of Eqs. (2.8a), (2.8b) and (2.8c) are not necessary.

Δt is the wave propagation time through an element. p and n at t are calculated from p and n at $t - \Delta t$ as follows:

$$p(t, i + 1) = T_p(i)p(t - \Delta t, i) + R_n(i)n(t - \Delta t, i + 1) \quad (2.9a)$$

$$n(t, i) = R_p(i)p(t - \Delta t, i) + T_n(i)n(t - \Delta t, i + 1) \quad (2.9b)$$

where R and T are the reflection and transmission ratios, respectively, and the suffixes correspond to p and n . R and T are calculated from the impedances of adjacent elements as follows:

$$R_p(i) = \frac{Z(i + 1) - Z(i)}{Z(i) + Z(i + 1)} \quad (2.10a)$$

$$R_n(i) = \frac{Z(i) - Z(i+1)}{Z(i) + Z(i+1)} \quad (2.10b)$$

$$T_p(i) = \frac{2Z(i+1)}{Z(i) + Z(i+1)} \quad (2.10c)$$

$$T_n(i) = \frac{2Z(i)}{Z(i) + Z(i+1)} \quad (2.10d)$$

The following formulae are obtained from Eq. (2.9):

$$p(t, i) = \frac{1}{T_n(i-1)} p(t - \Delta t, i-1) + \frac{R_n(i-1)}{T_n(i-1)} n(t, i-1) \quad (2.11a)$$

$$n(t, i) = -\frac{R_p(i-1)}{T_n(i-1)} p(t, i-1) + \frac{1}{T_n(i-1)} n(t + \Delta t, i-1) \quad (2.11b)$$

The temporal changes in p and n in a nearby element are calculated by Eq. (2.11) from the temporal changes p and n at B obtained with Eq. (2.8). Therefore the temporal changes in p and n in an arbitrary element between point B and the bit end are obtained with repeated calculation of Eq. (2.11).

The force-penetration curve is obtained from the temporal changes in p and n at the bit end, the i_L -th element, using the following formulae:

$$F(t) = -p(t - \Delta t, i_L) - n(t, i_L) \quad (2.12a)$$

$$u(t) = \frac{1}{Z(i_L)} \int_0^t \{-p(t - \Delta t, i_L) - n(t, i_L)\} dt \quad (2.12b)$$

where $F(t)$ is bit force positive in compression, and $u(t)$ is penetration. Fig. 2.12 (b) shows the flow chart of the calculation procedure described in this section.

2.5 Numerical studies of percussive drilling

Numerical simulation becomes more applicable to deal with complex physical problems with the rapid development of computational capabilities. Unlike experiment limited by the time and space, it can simulate a very large scale region and last an almost unlimited long period of time. It has been used to study on percussive drilling for many years. In literature, modeling percussive drilling is commonly divided into modeling the following

elementary processes: (i) collision between a piston and a rod; (ii) transmission of stress waves in rods; (iii) dissipation of stress waves at joints; and (iv) interaction between a bit and rock. Most studies separately dealt with the elementary processes because of their complex interactions. Dutta (1968) investigated the effect of the geometrical design of the piston on stress waveform with the numerical simulation. Okubo and Nishimatsu (1991) modeled the collision between the piston and the rod as a spring model. Lundberg et al. (1982, 1985) simulated the propagation of stress wave generated by repeated impacts of the piston on the rod with 1D theory of elastic waves. Chiang and Elias (2000) used an impulse-momentum principle to replace the 1D theory of elastic waves and numerically studied the stress wave transmission efficiency of the down-the-hole drilling under a variety of boundary conditions. Lundberg et al. (2001, 2006) studied the influence of 3D effects on the efficiency of percussive drilling due to the increased importance of radial inertia. A similar research using 3D finite element approach for modeling down-the-hole drilling was carried out by Chiang and Elias (2008). The rock under the percussive drilling exhibits a complex failure behavior due to its non-linearity, and the bit-rock contact condition. Fukui et al. (2010) indicated that force-penetration curves derived from experiments could be used to model the bit-rock interaction.

In this study, the stress wave propagation in rods and rod joints was reexamined in Chapter 3. An improved model, which was based on the one-dimensional theory of elastic waves and modified from the Okubo-Nishimatsu's model, was built and used to simulate stress wave propagation in rods and rod joints. One-dimensional and axisymmetric finite element models of percussive drilling were also constructed and used to simulate the stress wave propagation, and the simulated waves were compared to those of the improved model. In Chapter 5, a new non-linear bit-rock interaction model is proposed to model the impact penetration behavior of the button bits on Inada granite. In Chapter 6, the new stress wave propagation model and the new non-linear bit-rock interaction model are integrated into a new consecutive percussive drilling model.

References

Ajibose O. K. (2009): Nonlinear dynamics and contact fracture mechanics of high frequency percussive drilling, PhD Thesis, University of Aberdeen.

Beccu R., Lundberg B. (1990): Efficiency of percussive drilling of rock with dissipative joints, *Int. J. Impact Eng.*, vol. 9, pp. 277-287.

Carlsson J., Sundin K. G., Lundberg B. (1990): A method for determination of in-hole dynamic force-penetration data from two-point strain measurement on a percussive drill rod, *Int. J. Rock Mech. Min. Sci. & Geomech. Abstr.*, vol. 27, pp. 553-558.

Chiang L. E., Elias D. A. (2000): Modeling impact in down-the-hole rock drilling. *Int. J. of Rock Mech. Min. Sci.*, vol. 37, pp. 599-613.

Chiang L. E., Elias D. A. (2008): A 3D FEM methodology for simulating the impact in rock-drilling hammers, *Int. J. of Rock Mech. Min. Sci.*, vol. 45, pp. 701-711.

Depouhon A., Denoel V., Detournay E. (2013): A drifting impact oscillator with periodic impulsive loading: application to percussive drilling, *Physica D*, vol. 258, pp. 1-10.

Dutta P. K. (1968): The Determination of stress waveforms produced by percussive drill piston of various geometrical designs, *Int. J. Rock Mech. Min. Sci.*, vol. 5, pp. 501-508.

Fischer H. C. (1959): On Longitudinal Impact II, *Appl. Sci. Res.*, A8, pp. 278-308.

Fernberg H. (2008): Principles of rock drilling, *Surface Drilling*, Atlas Copco, pp. 9-11.

Fukui K., Abe H., Koizumi M., Tomosada H., Okubo S. (2007): Attenuation of rod stress in percussive long-hole drilling, *J. of MMIJ*, vol. 123, pp. 152-157.

Fukui K., Okubo S., Koizumi M., Shioda A., Matsuda T., Fukuda S. (2010): Force-penetration curves with a button bit in the percussive drilling, *J. of MMIJ*, vol. 126, pp. 512-518.

Haq N. U. (2010): Design and modelling of a piston accumulator for rock drill and its fatigue strength, Master thesis, Linkoping University.

Hayamizu H. (1974): Influence of rod-joint on strain wave propagating in drill rod, *Mining and Safety*, vol. 20, pp. 225-233.

Jimeno C. L., Jimeno E. L., Carcerero F. J. A. (1995): *Drilling and blasting of rock*, A. A. Balkema, Rotterdam.

Karlsson L. G., Lundberg B. and Sundin K. G. (1989): Experimental study of a percussive process for rock fragmentation, *Int. J. Rock Mech. Min. Sci. & Geomech. Abstr.*, vol. 26, pp. 45-50.

Lundberg B. (1973): Energy transfer in percussive rock destruction—I: comparison of percussive methods, *Int. J. Rock Mech. Min. Sci. & Geomech. Abstr.*, vol. 10, pp. 381-399.

Lundberg B., Henchoz A. (1977): Analysis of elastic waves from two-point strain measurement, *Experimental Mechanics*, vol. 17, pp. 213-218.

Lundberg B. (1982): Microcomputer simulation of stress wave energy transfer to rock in percussive drilling, *Int. J. Rock Mech. Min. Sci.*, vol. 19, pp. 229-239.

Lundberg B. (1985): Microcomputer simulation of percussive drilling, *Int. J. Rock Mech. Min. Sci.*, vol. 22, pp. 237-249.

Lundberg B., Beccu R., Nilsson A. (1989): Nonlinear dissipative spring mass model for a percussive drill rod joint of the coupling sleeve type, *Int. J. Impact Eng.*, vol. 8, pp. 303-313.

Lundberg B., Carlsson J., Sundin K. G. (1990): Analysis of elastic waves in non-uniform rods from two-point strain measurement, *J. of Sound and Vibration*, vol. 137(3), pp. 483-493.

Lundberg B., Okrouhlik M. (2001): Influence of 3D effects on the efficiency of percussive rock drilling, *Int. J. of Impact Eng.*, vol. 25(4), pp. 345-360.

Lundberg B., Okrouhlik M. (2006): Efficiency of a percussive rock drilling process with consideration of wave energy radiation into the rock, *Int. J. Impact Eng.*, vol. 32, pp. 1573-1583.

Lundberg B., Collet P. (2010): Optimal wave with respect to efficiency in percussive drilling with integral drill steel, *Int. J. of Impact Eng.*, vol. 37(8), pp. 901-906.

Okubo S., Nishimatsu Y. (1991): Computer simulation of percussive drilling, J. of MMIJ, vol. 107, pp. 209-214.

Okubo S., Nishimatsu Y., Akiyama M., Tatsumi T. (1992): Study on impact penetration test of rock, J. of MMIJ, vol. 108, pp. 134-140.

Okubo S., Ota A., Akiyama M. (1994): Transmission and dissipation of stress wave at a sleeve of percussive rock drill, J. of MMIJ, vol. 110, pp. 895-901.

Saksala T. (2011): Numerical modelling of bit-rock fracture mechanisms in percussive drilling with a continuum approach, Int. J. Numer. Anal. Meth. Geomech., vol. 35, pp. 1483-1505.

Saksala T. (2013): 3D numerical modelling of bit-rock fracture mechanisms in percussive drilling with a multiple-button bit, Int. J. Numer. Anal. Meth. Geomech., vol. 37, pp. 309-324.

Shah K. R., Wong T. F. (1997): Fracturing at contact surfaces subjected to normal and tangential loads, Int. J. Rock Mech. Min. Sci., vol. 34(5), pp. 727-739.

Stephenson B. R. (1963): Measurement of dynamic force-penetration characteristics in Indiana Limestone, Master thesis, University of Minnesota.

Treadway C. (1997): Percussion and down-the-hole hammer drilling: yesterday and today, Water Well Journal, vol. 51(7), pp. 55-57.

Weston E. M. (1910): Rock drills: design, construction, and use, McGraw-Hill Book Company, pp. 1-5.

Yanagihara N. (1977): New measuring method of impact force, J. of JSME, vol. 21, pp. 1085-1088.

Table 2.1 Specification of the apparatus used in the percussive long-hole drilling test

Rock	Inada Granite
Rock drill	HD210 (Furukawa Rock Drill Co., Ltd)
Piston	Length: 600 mm Mass: 6.08 kg
Shank rod	Length: 430 mm
Rod	Length: 3.66 m (Round section) Outer diameter: 39 mm Inner diameter: 14.3 mm
Bit	Nominal diameter: 64 mm Total tips: 10 Face tips: 4 – 9 mm Gauge tips: 6 – 11 mm
Sleeve-type rod joint	Screw type: T38 thread Length: 191mm Outer diameter: 55 mm
Hydraulic pressure	15 MPa (Maximum. 17.5 MPa)
Piston stroke	Short mode
Rotational speed	142 rpm
Damper pressure	10 MPa or 12 MPa

Table 2.2 Specification of the apparatus used in the single blow impact penetration test

Rock	Type: Inada Granite Uniaxial compressive strength: 148 MPa Young's modulus: 51.4 GPa
Rock drill	HD710 (Furukawa Rock Drill Co. Ltd)
Piston	Length: 710 mm
Shank rod	Length: 790 mm
Rod	Length: 3.66m (Round section) Outer diameter: 39mm Inner diameter: 14.5mm
Bit	Nominal diameter: 64mm Total tips: 12 Face tips: 8 – 11 mm Gauge tips: 4 – 10 mm
Sleeve-type rod joint	Type: T38 thread Length: 191mm Outer diameter: 55 mm
Hydraulic pressure	15 MPa
Rotation per blow	25.7°

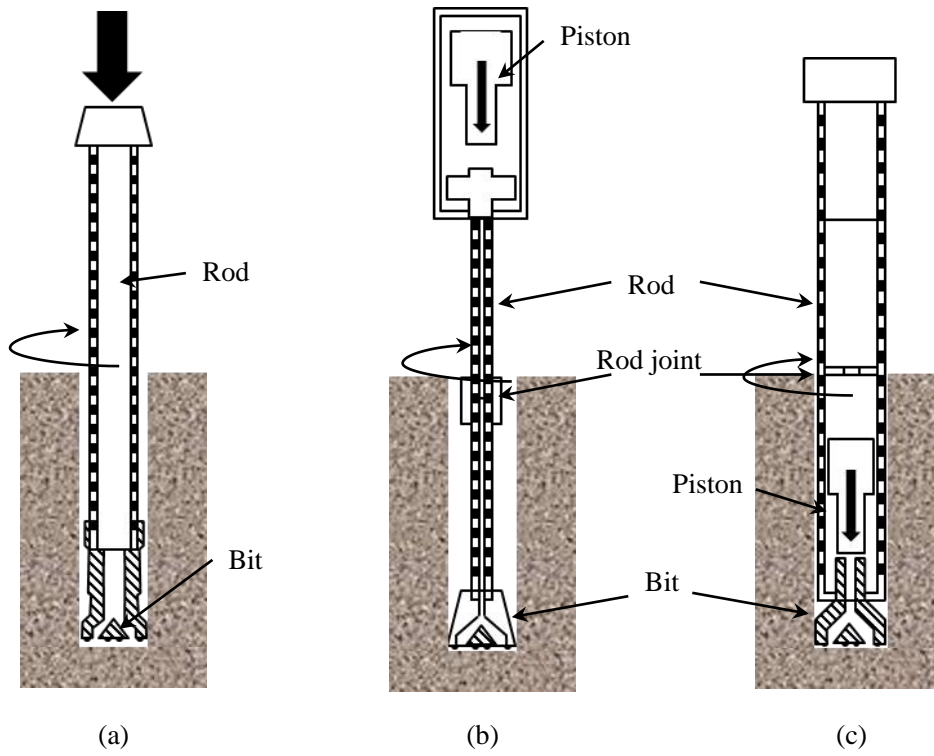


Fig. 2.1 Types of drilling methods. (a) Rotary drilling, (b) top hammer drilling and (c) down the hole drilling.

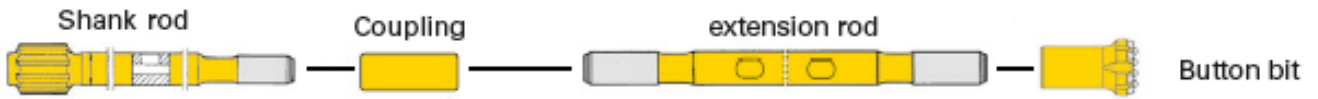


Fig. 2.2 Shank rod, coupling, extension rod and button bit in the top hammer drilling. (<http://www.atlascopco.com/>)

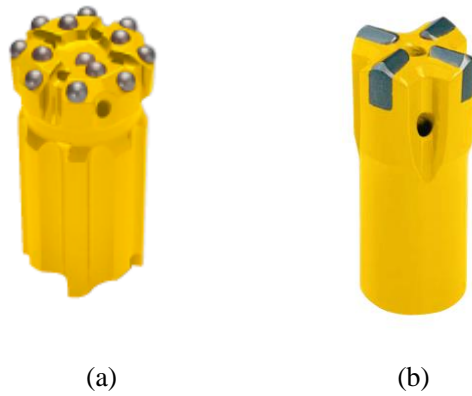
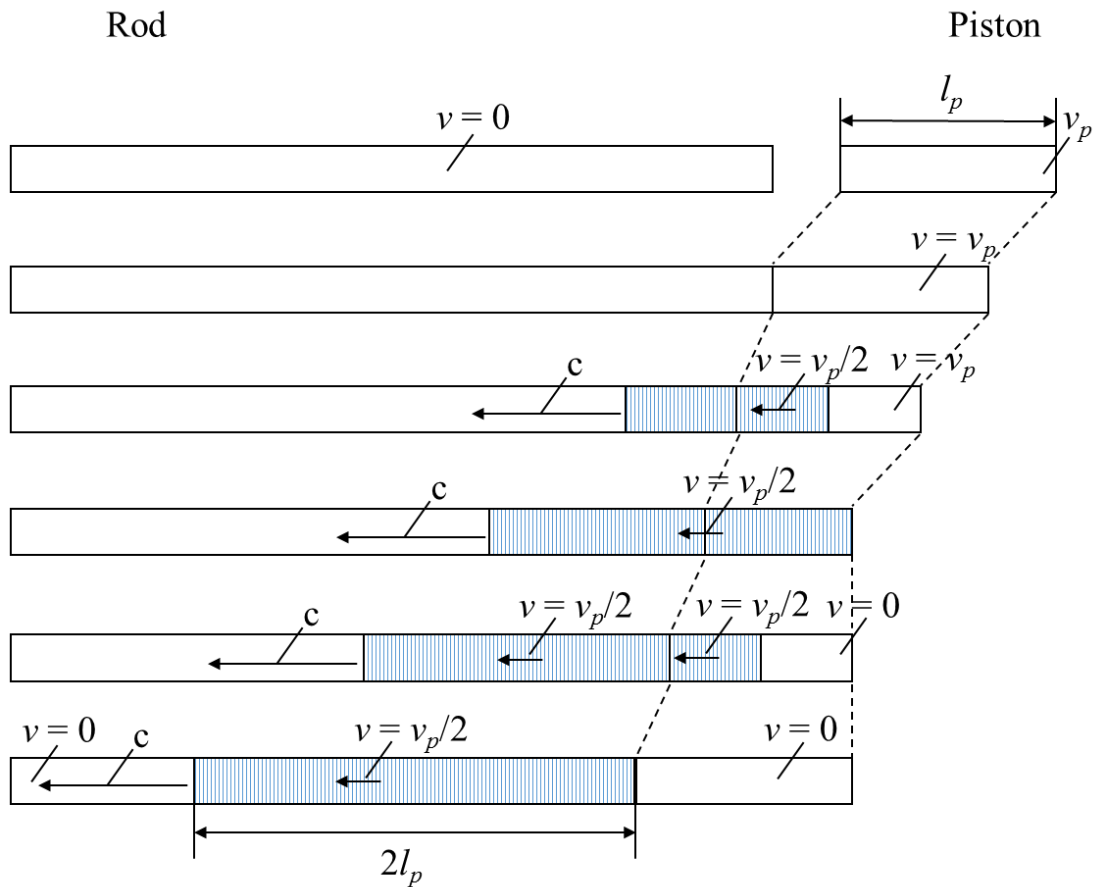


Fig. 2.3 Types of bits. (a) button bit and (b) insert bit. The insert bit is very seldom used, except when very straight holes are required. (<http://www.atlascopco.com/>)



Fig. 2.4 Extension rods with thread joints. (<http://www.atlascopco.com/>)



(a)

Fig. 2.5 Kinetic energy of the piston is transmitted to the bit through the rods in the form of elastic waves. (a) Impact of the piston on the rod. (b) Reflection of stress waves at the free bit end. (c) Reflection of stress waves from soft and hard rocks. (redrawn from Mikami 1986)

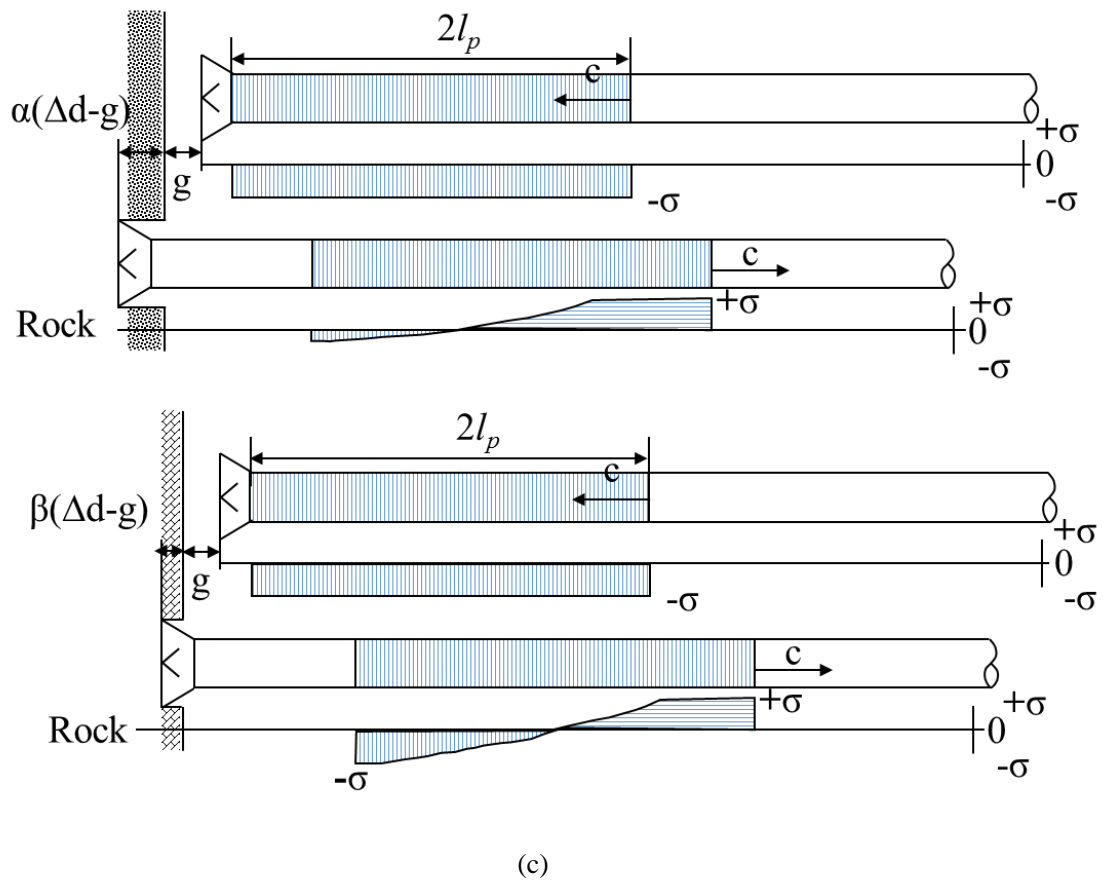


Fig. 2.5 (Continued) Kinetic energy of the piston is transmitted to the bit through the rods in the form of elastic waves (a) Impact of the piston on the rod. (b) Reflection of stress waves at the free bit end. (c) Reflection of stress waves from soft and hard rocks. (redrawn from Mikami 1986)

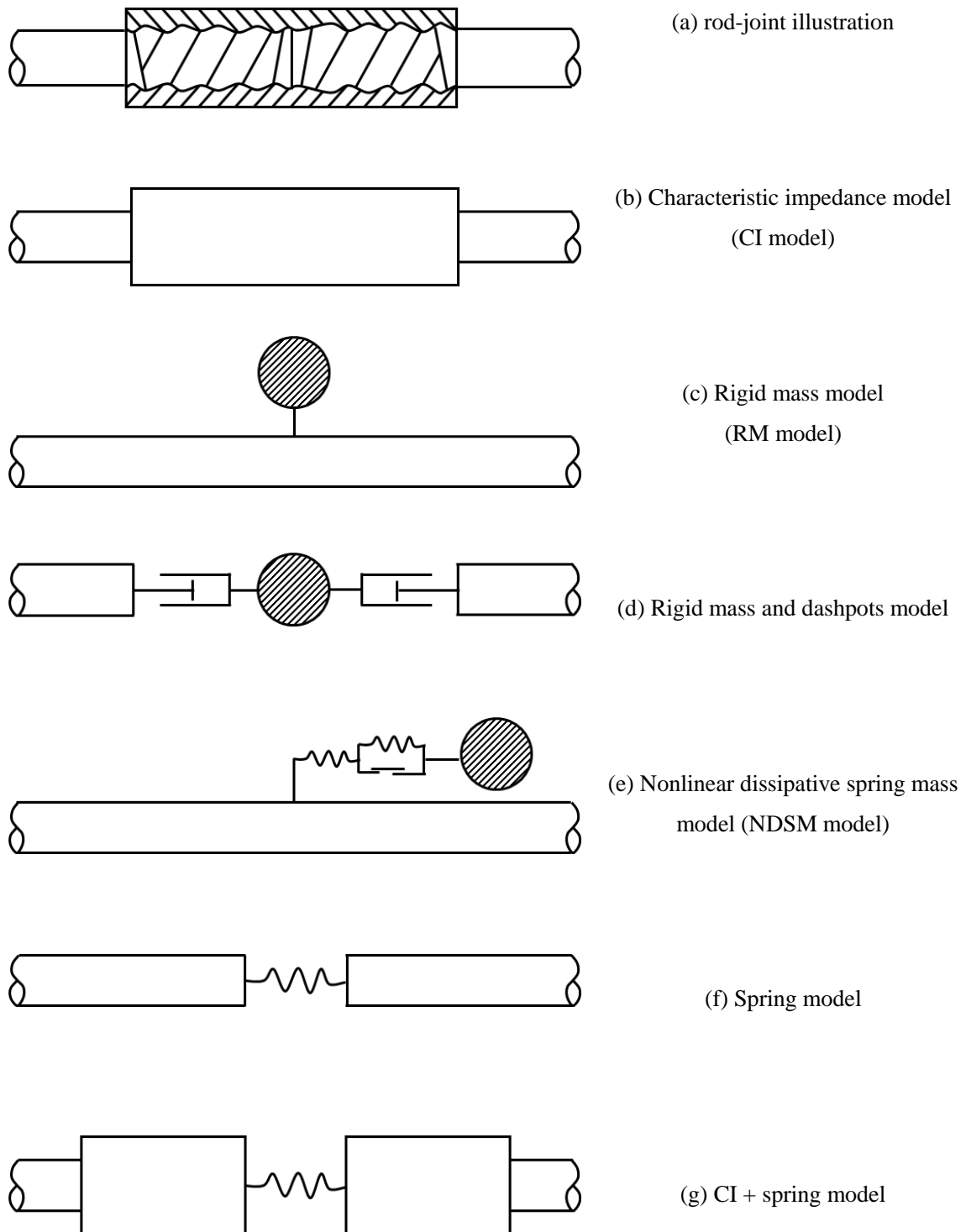


Fig. 2.6 Schematic illustration of a sleeve-type rod joint and its numerical models.

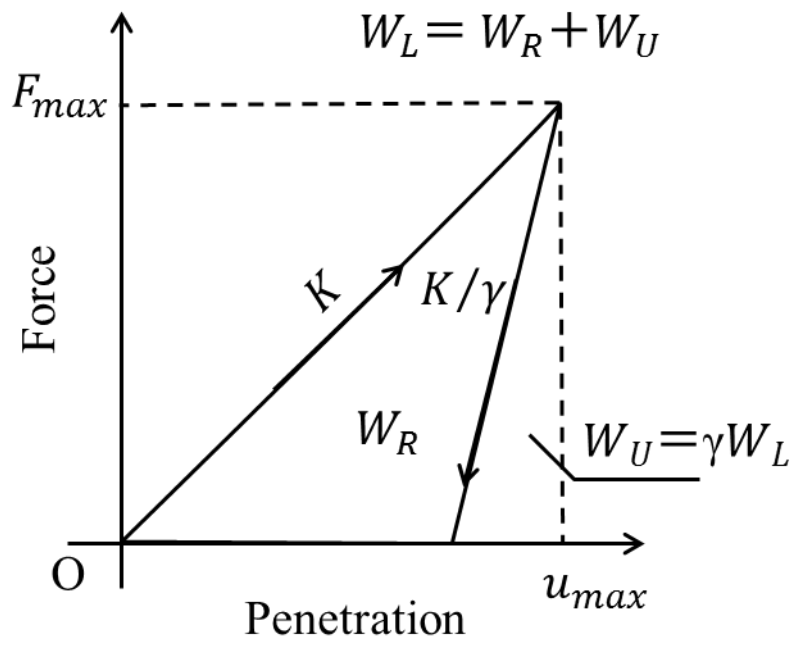


Fig. 2.7 Bilinear model for a bit-rock interaction.

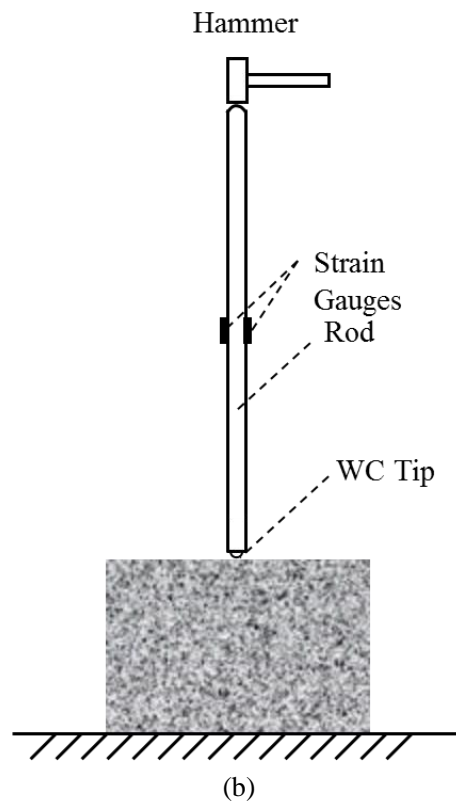
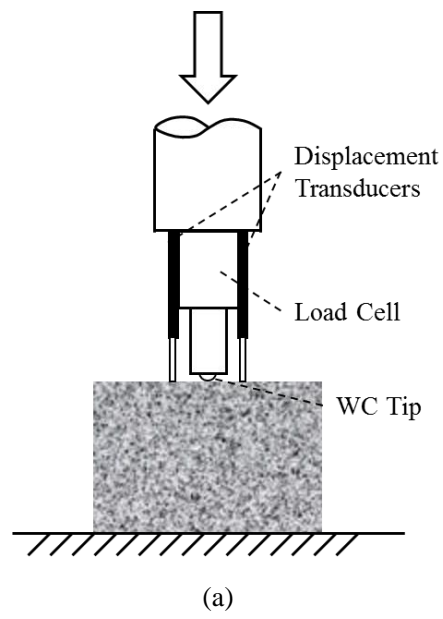
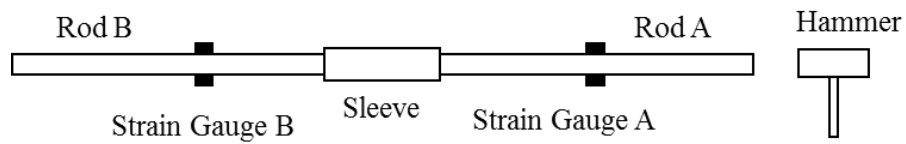
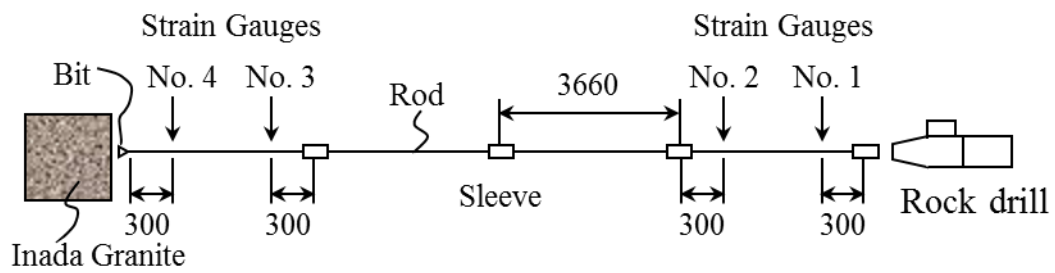


Fig. 2.8 Schematic illustrations of (a) static penetration test and (b) impact penetration test with hammer (redrawn from Okubo et al. 1992).



(a)

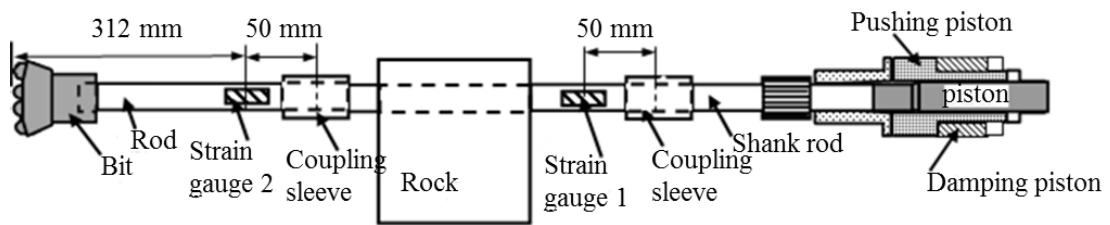


(b)

Fig. 2.9 Experimental setups for studying the energy dissipation of a rod joint in the percussive drilling with (a) a hammer and (b) a rock drill.



(a)

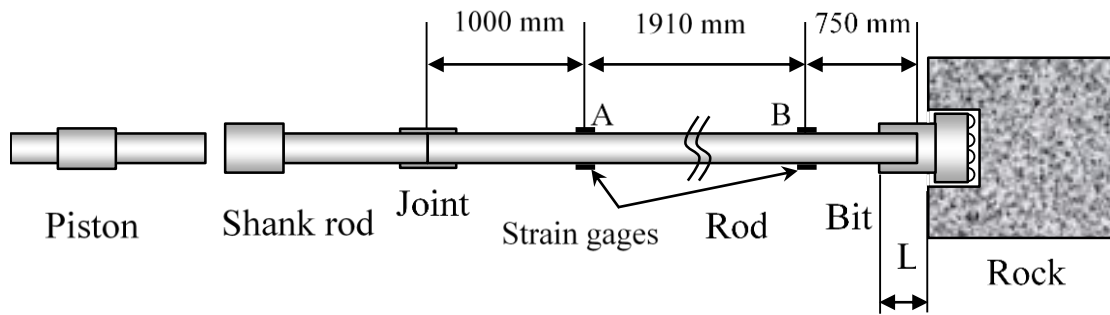


(b)

Fig. 2.10 Percussive long-hole drilling test. (a) Photograph of the test, and (b) schematic illustration of the experimental setup (Fukui et al. 2007).



(a)

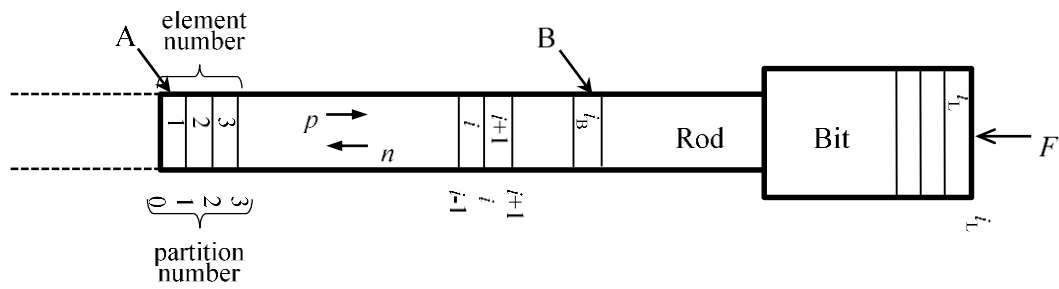


(b)

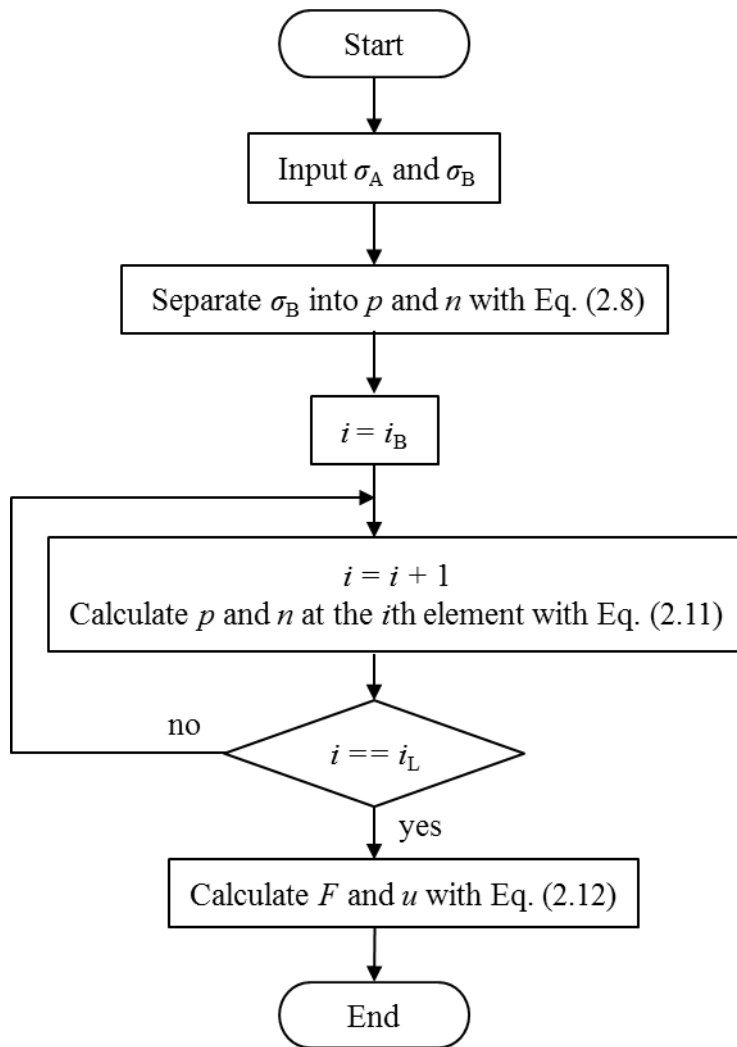


(c)

Fig. 2.11 Impact penetration tester. (a) Photograph of the single blow impact penetration (SBIP) test, (b) schematic illustration of the impact penetration tester, and (c) used button bit with the diameter of 64 mm (Fukui et al. 2010).



(a)



(b)

Fig. 2.12 Calculation of a force-penetration curve with the TPSM method. (a) Rod and bit subdivided into elements. (b) Calculation procedure.

Chapter 3 Stress wave propagation in rods during percussive drilling

3.1 Introduction

In percussive drilling with a hydraulic percussion rock drill, elastic waves play a crucial role in partial conversion of kinetic energy into crushing work (Lundberg and Okrouhlik 2001). The elastic waves generated by the repeated impacts of the piston on the shank rod, propagate along the rods and the rod joints, and then arrive at the bit. They are not free from three-dimensional (3D) effects. In an actual hydraulic rock drills, however, the generated waves are generally much longer than the transverse dimensions of the drill string. Under these conditions the three-dimensional effects can be neglected, and it is justified to consider the wave motion as one-dimensional (Kolsky 1963; Achenbach 1973). In previous studies (Donnell 1930; Takaoka and Hayamizu 1956; Fischer 1959; Fairhurst 1961; Simon 1962; Dutta 1968; Lundberg et al. 1982, 1985, 1986, 1989; Fu and Paul 1970; Nordlund 1989; Pang and Goldsmith 1990; Okubo and Nishimatsu 1991), the one-dimensional (1D) theory of elastic waves has been accepted to study the phenomena of stress wave propagation in rods during percussive drilling. However, it has become increasingly interesting to use drill tubes with relatively thin walls instead of conventional drill rods with small central hole (Lundberg and Okrouhlik 2001). Moreover, it is observed that the 3D effects, which result in obvious calculation errors when the two-point strain measurement method is used to calculate force-penetration curves. Thus, it is necessary to reexamine elastic wave propagation in rods with consideration of the 3D effects due to the increased importance of radial inertia in such systems.

In this chapter, an improved model, which is based on the 1D theory of elastic waves and modified from the Okubo-Nishimatsu's model, has been examined for simulating the stress wave propagation in rod during percussive drilling. In this new model, piston and shank rod are modeled to have the same acoustic impedance as products. Stress wave attenuation in rod joints is one of the key factors to estimate the drilling efficiency (Fukui et al. 2007). A new numerical model for a sleeve-type rod joint in which a separated CI model was connected with a spring was taken into account. In addition, one-dimensional (1D) and axisymmetric finite element models of percussive drilling with a hydraulic percussion rock drill were built for simulating stress wave propagation. The 3D effects on stress wave propagation during percussive drilling were investigated. The waves calculated with the new model were compared to the ones calculated with the 1D and axisymmetric finite element models.

3.2 Numerical models and methods

3.2.1 Improved model based on the 1D theory of elastic waves

The improved model was based on 1D theory of elastic waves and modified from the Okubo-Nishimatsu's model (Okubo and Nishimatsu 1991). It was composed of a piston, a shank rod, a rod and a rod joint. Stress wave propagation in rods is calculated in a similar way as the Okubo-Nishimatsu's model. As elastic bodies, the piston, shank rod, rod, and the rod joint were divided into elements with the uniform length Δl and the acoustic impedance of each elements Z_i was equal to $A_i \cdot E/c$. The force generated from the collision between the piston and the shank rod was calculated with Eq. (3.1).

$$F_{ps} = \begin{cases} 0 & \text{if } \delta_{ps} \geq 0 \\ -K_{ps}\delta_{ps}, & \text{if } \delta_{ps} < 0 \end{cases} \quad (3.1)$$

where K_{ps} and δ_{ps} are the spring constant and the gap between the piston and the shank rod, respectively.

In the Okubo-Nishimatsu's model, the piston and the rod were simplified into two circular cylinders. In the improved model, the acoustic impedances of the piston and the shank rod were set to be consistent with their actual shapes. The acoustic impedance of the rod was set to a constant value along its longitudinal axis. The sleeve-type rod joint was modeled as the CI + spring model and the force F_{sr} between the shank rod and rod was calculated as follows.

$$F_{sr} = -K_{sr}\delta_{sr} \quad (3.2)$$

where F_{sr} is the force acting on the contact faces of the shank rod and the rod. δ_{sr} and K_{sr} are the clearance and spring constant between the piston and the shank rod.

Other constants related to the improved model for the HD210 hydraulic percussion rock drill (Hereinafter referred to as HD210) were listed in Table 3.1. The time interval Δt was 0.2 μs , and the length of each segment was set to 1 mm because elastic waves propagate 1 mm within the time. The spring constants K_{ps} and K_{sr} , were determined with sensitivity. The calculated wave was compared to the measured one at the strain gauge 1 as shown in Fig. 2.10 (b). The components of the rock drill body, bit and the rock on stress wave propagation in rods and rod joints were neglected.

The improved model for the HD712 hydraulic percussion rock drill (Hereinafter referred to as HD712) was also prepared and used to simulate the stress wave propagation in rod during the single blow impact penetration tests with the HD712. The spring constants K_{ps} and K_{sr} for the HD712 were also identified with sensitivity analysis and compared to those of the HD210 for checking whether the spring constants were universal or not.

3.2.2 Finite element method

Analytical solutions can only be applied to impact problems for elastic solids with very simple geometries. Since the piston and the shank rod in hydraulic percussion rock drill have complex geometrical shapes, the finite element method (FEM) was used to simulate stress wave propagation in rod during percussive drilling.

The numerical simulation of stress wave propagation in rod with one dimensional (1D) and axisymmetric finite element models were performed with the aid of the commercial software ANSYS. Two methods (ANSYS User's Manual) are employed for the transient dynamic analysis in the ANSYS program: the central difference time integration method for explicit transient analyses and the Newmark time integration method (including an improved algorithm called HHT) for implicit transient analyses. Herein, the HHT method is chosen for simulating stress wave propagation in rods during percussive drilling, and the basic form of the method is given by:

$$[M]\{\ddot{u}_{n+1-\alpha_m}\} + [C]\{\dot{u}_{n+1-\alpha_f}\} + [K]\{u_{n+1-\alpha_f}\} = \{F_{n+1-\alpha_f}^a\} \quad (3.3)$$

where $[M]$, $[C]$ and $[K]$ are the mass matrix, damping matrix and stiffness matrix, respectively. $\{\ddot{u}\}$, $\{\dot{u}\}$, $\{u\}$ and $\{F\}$ are the acceleration, velocity, displacement and load vector of nodal, respectively. The detailed equations are expressed as follows:

$$\begin{aligned} \{\ddot{u}_{n+1-\alpha_m}\} &= (1 - \alpha_m)\{\ddot{u}_{n+1}\} + \alpha_m\{\ddot{u}_n\} \\ \{\dot{u}_{n+1-\alpha_f}\} &= (1 - \alpha_f)\{\dot{u}_{n+1}\} + \alpha_f\{\dot{u}_n\} \\ \{u_{n+1-\alpha_f}\} &= (1 - \alpha_f)\{u_{n+1}\} + \alpha_f\{u_n\} \\ \{F_{n+1-\alpha_f}^a\} &= (1 - \alpha_f)\{F_{n+1}^a\} + \alpha_f\{F_n^a\} \end{aligned} \quad (3.4)$$

In addition the following formulae are assumed in the Newmark method.

$$\{\dot{u}_{n+1}\} = \{\dot{u}_n\} + [(1 - \delta)\{\dot{u}_n\} + \delta\{\ddot{u}_{n+1}\}]\Delta t \quad (3.5)$$

$$\{u_{n+1}\} = \{u_n\} + \{\dot{u}_n\}\Delta t + \left[\left(\frac{1}{2} - \alpha\right)\{\ddot{u}_n\} + \alpha\{\ddot{u}_{n+1}\}\right]\Delta t^2$$

where α , δ are Newmark integration parameters, and Δt is equal to $t_{n+1} - t_n$.

In Eq. (3.4) equations it can be seen that the two successive time steps of n and $n+1$ are linearly combined in the HHT method. α_m and α_f are two extra integration parameters for the interpolation of the acceleration and the displacement, velocity and loads.

3.2.3 1D finite element model of percussive drilling

The 1D finite element model of the HD210 was prepared for simulating the stress wave propagation in rod during the percussive long-hole drilling test mentioned in Section 2.4.3. In the calculation, the time step Δt was set to 2 μs , in which stress waves pass through an element with the speed $c = (E/\rho)^{1/2}$. The rod stress at the strain gauge 1 shown in Fig. 2.10 (b) was calculated and compared to the measured one. The impact speed v of the piston was set to 9.05 m/s, which was set to the actual speed just before the piston impacts on the shank rod in the test. The shank rod and the rod were at rest before the impact. The initial gap between the piston and the shank rod was set to 1 μm . All components involved in percussive drilling were modeled with the LINK1 element. The numbers of the components and related parameters are listed in Table 3.2. In the LINK1 element, the cross-sectional area is used to express the geometrical characteristic of the components.

The collision between the piston and the shank rod was modeled with the CONTA178 element. The element is a node-to-node contact element which can handle the cases when the contact location is known beforehand. It is applicable to 3D geometries and also can be used in 2D and axisymmetric models by constraining the UZ degrees of freedom. There are four different contact algorithms implemented in the element, viz., pure penalty method, augmented Lagrange method, pure Lagrange multiplier method as well as Lagrange multiplier on contact normal and penalty on frictional direction. Here, the pure penalty method was chosen and the equation for calculating force between the piston and the shank rod was derived;

$$F_{ps} = \begin{cases} 0 & \text{if } u_{ps} > 0 \\ K_{ps}u_{ps} & \text{if } u_{ps} \leq 0 \end{cases} \quad (3.6)$$

where K_{ps} and u_{ps} are the spring constant and gap size between the piston

and the shank rod, respectively.

The sleeve-type rod joint between the shank rod and the rod was modeled by the COMBIN14 element with the spring constant K_{sr} of 1 GN/m. The element is a spring-damper element without mass and defined by two nodes, spring constant and damping coefficients. The damping capability was not used, only the spring constant needs to be set in advance.

3.2.4 Axisymmetric finite element model of percussive drilling

All components were considered to be of steel with Young's modulus E of 210 GPa, Poisson's ratio ν of 0.3 and modeled with the 8-node axisymmetric quadrilateral PLANE183 element. The collision between the piston and the shank rod was modeled as surface-to-surface contact elements. The target surface, the back end of the shank rod, was modeled with the TARGE169 element. The contact surface, the front end of the piston, was modeled with CONTA172 element. The CONTA172 element is used to represent contact and sliding between 2-D "target" surfaces and a deformable surface, defined by this element. The element is applicable to 2-D structural and coupled field contact analyses. The contact stiffness between the piston and the shank rod is a significant parameter, which directly affects the simulated waveform. Thus, the Augmented Lagrangian contact algorithm was chosen to handle the contact behavior between the piston and the shank rod. The Augmented Lagrangian method is an iterative series of penalty updates to find the Lagrange multipliers (i.e., contact tractions). Compared to the pure penalty method, the Augmented Lagrangian method usually leads to better conditioning and is less sensitive to the magnitude of the contact stiffness coefficient. In addition, the contact stiffness coefficient was set to automatically update for each iteration time step. Location of contact detection point was set to on Gauss point.

The sleeve-type rod joint between the shank rod and rod was also modeled as surface-to-surface contact elements like the aforementioned contact between the piston and the shank rod. The rod joint was divided into two parts. They were added on the front end of the shank rod and the back end of the rod, respectively. The bit and the rod were taken as a whole, and the thread connection between them was neglected. The carbide tips on the button bit were also neglected.

3.3 Numerical results

3.3.1 Calculated results of the improved model

Fig. 3.1 shows the calculated and measured rod stresses in blue and red

curves, respectively. The measured data of rod stress were from the percussive long-hole drilling test with the HD210, which was mentioned in Section 2.4.3. In the figures the time when the first wave arrived was set to the origin.

Fig. 3.1 (a) shows the calculated wave when the models of the piston and the rod were simplified as circular cylinders, that is, the acoustic impedances of the piston and the shank rod were constant values. The sleeve-type rod joint between the shank rod and the rod was not considered, and the shank rod and the rod were taken as whole in the calculation. The used parameters are listed in the case 1 of Table 3.1. The collision between the piston and the shank rod was modeled as the spring model and the spring constant K_{ps} between the two components was set to 600 MN/m, which was the same as the value reported in Okubo and Nishimatsu (1991). The amplitude of the calculated wave was consistent with that of the measured wave. However, the wavelength and small oscillations in the measured wave cannot be reproduced.

Fig. 3.1 (b) shows the calculated wave when the piston and the rod were modeled to be consistent with their actual shape. The sleeve-type rod joint was not considered and the shank rod and the rod were taken as a whole in the calculation. The used parameters are listed in the case 2 of Table 3.1. The calculated wave was closer to the measured one than that shown in Fig. 3.1 (a). However, the wavelength and small oscillations in the measured wave the simulation also cannot be reproduced.

Fig. 3.1 (c) shows the calculated wave when the piston and the rod were modeled to be consistent with their actual shape, and the sleeve-type rod joint was modeled as the spring model shown in Fig. 2.6 (f). The used parameters are listed in the case 3 of Table 3.1. The spring constant K_{ps} were set to 600 MN/m. The spring constant K_{sr} of the joint model was set to 710 MN/m, which is the same as the value of Okubo et al. (1994). The slope at the beginning of the calculated wave is smaller than the measured one, but the local shape around the peak is closer to the measured one than Figs. 3.1 (a) and (b).

Fig. 3.1 (d) shows the calculated wave when the piston and the shank rod were modeled to be consistent with their actual shape, and the sleeve-type rod joint was modeled as the spring model shown in Fig. 2.6 (f). The used parameters are listed in the case 4 of Table 3.1. The spring constant K_{ps} between the piston and the shank rod was set to 10 GN/m. K_{sr} was set to 1 GN/m based on its sensitivity analysis. The calculated wave is more

consistent with the measured one than those shown in Figs. 3.1 (a), (b) and (c). Not only the amplitude and wavelength but also the small oscillations observed in the measured wave were reproduced. However, the obvious difference between the calculated and the measured waves in the latter portion of rod stress from 0.4 ms.

Fig. 3.1 (e) shows the calculated wave when the piston and the rod were modeled to be consistent with their actual shape, and the sleeve-type rod joint was modeled as the CI model (Fischer 1959) shown in Fig. 2.6 (b). The used parameters are listed in the case 5 of Table 3.1. The spring constant K_{ps} of the collision between the piston and the shank rod was set to 10 GN/m based on its sensitivity analysis. The shape and oscillations of the calculated wave were consistent with those of the measured wave. However, the amplitude of the oscillations in the calculated wave is smaller while the frequency of the oscillations is larger than the measured one.

Fig. 3.1 (f) shows the calculated wave when the piston and the rod were modeled to be consistent with their actual shape, and the sleeve-type rod joint was modeled as the CI + spring model shown in Fig. 2.6 (g). The used parameters are listed in the case 6 of Table 3.1. The spring constant K_{ps} of the collision between the piston and shank rod was set to 10 GN/m and the spring constant K_{sr} of the joint model between the shank rod and the rod was set to 1 GN/m. The calculated wave was closer to the measured wave than the others, especially the latter portion of the wave.

Fig. 3.2 shows the calculated and measured rod stresses of the single blow impact penetration (SBIP) tests with the HD712, which was already introduced in Section 2.4.4. Blue and red curves represent the calculated and measured waves, respectively. In the figure, the time at which the waves arrived was set to the origin. In the calculation, the piston and the rod were modeled to be consistent with their actual shape. The sleeve-type rod joint was modeled as the CI + spring model. The spring constant K_{ps} of the collision between the piston and the shank rod was set to 10 GN/m and the spring constant K_{sr} of the joint model between the shank rod and the rod was set to 10 GN/m based on the sensitivity analysis. The measured wave is well reproduced by simulation under the aforementioned settings.

3.3.2 Calculated results of the 1D finite element model

Fig. 3.3 shows the calculated rod stresses of the percussive long-hole drilling test with the HD210 with 1D finite element model of percussive drilling. The models of the piston, shank rod, rod joint, rod and the bit were set to be consistent with their actual shape. The spring constant K_{ps} between the

piston and the shank rod was varied from 600 MN/m to 100 GN/m.

Fig. 3.3 (a) shows in the case of $K_{ps} = 600$ MN/m, the peak of the calculated wave is in good agreement with that of the measured wave, but many small oscillations observed in the measured wave cannot be reproduced. The calculated wave is close to a sine wave, and the wavelength is longer than the measured wave. The slope of the calculated wave from 0 ms to 0.2 ms is lower than that of the measured one. In Fig. 3.3 (b), the small oscillations still cannot be appeared in the calculated wave of $K_{ps} = 1$ GN/m. But the wavelength is closer to the measured one than that of $K_{ps} = 600$ MN/m. The slope of the calculated wave from 0 ms to 0.2 ms is in good agreement with the measured one. The peak of the calculated result is a little larger than that of the measured. In Fig. 3.3 (c), the distinct oscillations are generated in calculated wave and simultaneously the waveform gradually changes from a sine wave to a rectangle when K_{ps} is 10 GN/m. Compared to the oscillations in the measured wave, the number of the calculated oscillations is smaller but the magnitude is larger. In Fig. 3.3 (d), when K_{ps} is 100 GN/m, the simulated result is not obviously different with that of $K_{ps} = 10$ GN/m.

3.3.3 Calculated results of the axisymmetric finite element model

Fig. 3.4 shows the comparison between the calculated rod stress with the axisymmetric finite element model of percussive drilling and the measured one from the single blow impact penetration (SBIP) test. In Fig. 3.4, red and blue curves represent the measured and calculated waves, respectively. In the left-hand side, the calculated waves were computed with the coarse-mesh axisymmetric finite element models of the piston, shank rod, rod joint, rod and the bit. In the right-hand side, the calculated waves were computed with the fine-mesh axisymmetric finite element models.

Compared Fig. 3.4 (a) to Fig. 3.4 (b), it is observed that with the decrease of the time step from $1 \mu\text{s} \sim 10 \mu\text{s}$ to $0.1 \mu\text{s} \sim 1 \mu\text{s}$ the simulation accuracy is obviously improved. But no more significant improvements in Fig. 3.4 (c) are achieved with further decreasing the time step from $0.1 \mu\text{s} \sim 1 \mu\text{s}$ to $0.05 \mu\text{s} \sim 0.5 \mu\text{s}$. Instead, distinct high frequency oscillations appear in the left figure of Fig. 3.4 (c). However, the same phenomenon did not arise in the right figure of the Fig. 3.4 (c). The size of the time step should be appropriate to the mesh scale of the finite element model, otherwise unexpected high-frequency oscillations will be generated. In this study, the coarse-mesh model with the time step of $0.1 \mu\text{s} \sim 1 \mu\text{s}$ can effectively be used for simulating the axial stress responses in the extension rod.

From Fig. 3.4(b), it can also be noticed that an obvious deviation appeared

between the calculated and measured waves in stress responses of B after 0.6 ms which is because stress waves reflected from the bit end are mixed together and the calculation errors caused by the simplified bit model.

For both the measured and calculated waves in Fig. 3.4 (c), the stress responses of *B* is moved forward 0.376 ms horizontally and illustrated in Fig. 3.5. The 0.376 ms is the time that the stress waves arrived at *B* after it departed from *A*. As seen in Fig. 3.5 (a), there is a little difference between the two measured waves during the period from 0 ms to 0.35 ms, which is caused by the lateral-inertia effect. From Fig. 3.5 (b) it can be seen that the same phenomena can be reproduced by the axisymmetric finite element model of percussive drilling.

Fig. 3.6 shows that the calculated wave (blue) with the axisymmetric finite element model is closer to the measured wave (red) than the calculated wave (green) with 1D theory of elastic waves, especially after 0.5 ms. The high-frequency parts of the waves are indicated by black arrows are effectively reproduced by the axisymmetric finite element model. There are also deviation between the calculated wave of the axisymmetric finite element model and the measured wave from 0.3 ms to 0.4 ms. In addition, the differences of the calculated waves of one- and three-dimensional models are small.

3.4 Discussion

The measured waves did not have simple shape but had many small oscillations due to the non-uniform shapes of the piston and shank rod. To reproduce the oscillations, not only the acoustic impedances of the piston and the shank rod but also the spring constants K_{pr} and K_{sr} needed to be set to appropriate values. In this calculation, the calculated wave was most consistent with the measured one when the spring constant of the joint model was much smaller than that of the collision between the piston and the shank rod. Even in Fig. 3.1 (f), there is a difference between the calculated and measured waves, which may be caused by the simplified spring model of the rod joint. Therefore additional modification in the simulation will be required.

The measured waves from the percussive drilling tests with the HD210 and with the HD712 can be reproduced with the one-dimensional model when the piston and the shank rod were modeled to be consistent with their shape and the sleeve-type rod joint is modeled as the CI + spring model. The spring constant of the joint model between the shank rod and the rod were set to 10 GN/m for HD712 and 1 GN/m for HD210. The difference between the

constants is probably caused not by the difference in the products but in the drilling conditions. The SBIP test with HD712 was conducted with specially-manufactured equipment in a laboratory, and the rod joints were tightened after each blow. In contrast the percussive long-hole drilling test with the HD210 was performed in the field. The preload of the rod joint for HD210 was probably lower than that for HD712. The results indicate that the spring constant in the model of a rod joint needs to be set appropriately depending on drilling conditions.

K_{ps} needs to set an appropriate value for accurately simulating stress wave propagation in rods. In this study, the magnitude of K_{ps} is larger than that in Okubo and Nishimatsu (1991). It is found that the waveform is close to a square wave for the larger value of K_{ps} , while to a sine wave for the smaller value of K_{ps} . In addition, the oscillations caused by the complex shape of the piston and the shank rod only appeared in the simulation results when K_{ps} is large enough. However, with an increase in K_{ps} the convergence of the calculation in ANSYS becomes difficult unless the time step Δt is decreased, the meshing is refined or both of them. The magnitude of spring constant K_{ps} around 10 GN/m is recommended in this study.

Though the models are one-dimensional, differences of the calculated waves with one- and three-dimensional models seem to be insignificant, in comparison with the effects of the consistency between the models for the piston, shank rod, and rod joints and actual products.

3.5 Conclusions

The aim of the chapter is to construct a new realistic numerical model of stress wave propagation in rods and rod joints during percussive drilling. First, the improved numerical model based on 1D theory of elastic waves and modified from the Okubo-Nishimatsu's model was proposed. In the improved model, the sleeve-type rod joint was modeled as the CI + spring model, and the acoustic impedances of the piston, shank rod were set to be the same as the actual products. Stress wave propagation in rods and rod joints during the percussive long-hole drilling test with the HD210 and during the single blow impact penetration test with the HD712 were simulated with the improved model. The measured waves in the two kinds of tests can be reproduced with the improved model. The spring constant K_{ps} between the piston and the shank rod was set to the same value while the spring constant K_{sr} of the rod joint model between the shank rod and the rod was set to different values in the two simulations, which was because the drilling conditions were different in the two kinds of tests.

In addition, the stress wave propagation in rods and rod joints was also computed with the 1D and axisymmetric finite element models. The calculated waves of the finite element models also indicate that the spring constants K_{ps} and K_{sr} were important and needed to set appropriate values for accurate simulation of the stress wave propagation in rods and rod joints. Too large value of K_{ps} would cause the poor convergence of the calculation in ANSYS unless the time step further decreased. The calculated waves with the 1D finite element model are in good agreement with those computed with the improved model. The calculated waves of the axisymmetric finite element model are more appropriate than those of 1D finite element model on reproduction of lateral-inertia effect. However, there are no obvious differences on precision between the numerical results calculated with the 3D axisymmetric model and with 1D model.

References

Donnell L. H. (1930): Longitudinal wave transmission and impact, University of Michigan.

Dutta P. K. (1968): The determination of stress waveforms produced by percussive drill pistons of various geometrical designs, *Int. J. Rock Mech. Min. Sci.*, vol. 5, pp. 501-518.

Fairhurst C. (1961): Wave mechanics of percussive drilling, *Mine Quarry Engng*, vol. 27(3), pp. 120-130.

Fischer H. C. (1959): On Longitudinal Impact I-III. *Appl. Sci. Res.*, A8, pp. 105-139, A8, pp. 278-308, A9, pp. 9-42.

Fu C. C., Paul B. (1970): Energy transfer through chains of impacting rods, *International Journal for Numerical Methods in Engineering*, vol. 2, pp. 363-385.

Fukui K., Abe, H., Koizumi, M., Tomosada, H., Okubo, S. (2007): Attenuation of Rod Stress in Percussive Long-hole Drilling. *J. of MMIJ*, Vol. 123, pp. 152-157 (In Japanese).

Kolsky H. (1963): Stress waves in solids, Chapter III, New York, Dover Publications Inc.

Lundberg B. (1982): Microcomputer simulation of stress wave energy transfer to rock in percussive drilling, *Int. J. Rock Mech. Min. Sci.*, vol. 19, pp. 229-239.

Lundberg B. (1985): Microcomputer simulation of percussive drilling, *Int. J. Rock Mech. Min. Sci.*, vol. 22, pp. 237-249.

Lundberg B., (1986): Influence of geometrical design on the efficiency of a simple down-the-hole percussive drill, *Int. J. Rock Mech. Min. Sci. & Geomech. Abstr.*, vol. 23(3), pp. 281-287.

Lundberg B., Beccu R., Nilsson A. (1989): Nonlinear dissipative spring mass model for a percussive drill rod joint of the coupling sleeve type, *Int. J. Impact Eng.*, vol. 8, pp. 303-313.

Lundberg B., Okrouhlik M. (2001): Influence of 3D effects on the efficiency of percussive rock drilling, *Int. J. of Impact Eng.*, vol. 25(4), pp. 345-360.

Nordlund E. (1989): The effect of thrust on the performance of percussive rock drills, *Int. J. Rock Mech. Min. Sci. & Geomech. Abstr.*, vol. 26(1), pp 51-59.

Okubo S., Nishimatsu Y. (1991): Computer simulation of percussive drilling, *J. of MMIJ*, vol. 107, pp. 209-214 (In Japanese).

Okubo S., Ota A., Akiyama M. (1994): Transmission and dissipation of stress wave at a sleeve of percussive rock drill, *J. of MMIJ*, vol. 110, pp. 895-901 (In Japanese).

Pang S. S., Goldsmith W. (1990): *Rock mechanics and rock engineering*, vol. 23, pp. 53-63.

Simon R. (1962): Digital machine computations of the stress waves produced by striker impacts in percussive drilling machines, *Proceedings of the Fifth Symposium on Rock Mechanics*, University of Minnesota.

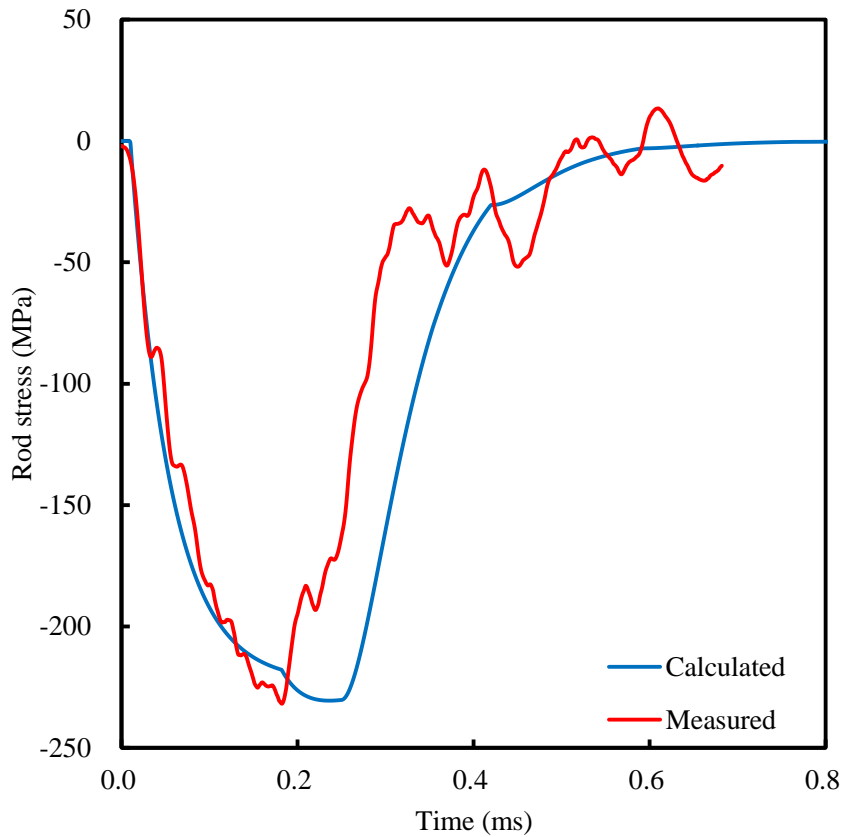
Takaoka S., Hayamizu H., (1956): Studies on the percussive deep hole drilling of rocks, *J. Min. metall. Inst.*, vol. 72, pp. 497-502 (in Japanese).

Table 3.1 Constants and parameters used in simulation cases with the improved model

	Case 1	Case 2	Case 3	Case 4	Case 5	Case 6
Time interval Δt (μs)				0.2		
Element size (mm)				1		
Initial velocity v_0 (m/s)				9.05		
Shapes of piston and rods	Circular cylinders	Actual shapes	Actual shapes	Actual shapes	Actual shapes	Actual shapes
Collison between piston and rod K_{ps} (MN/m)	600	600	600	600 ~100,000	600 ~100,000	600 ~100,000
Rod joint	None	None	Spring model	Spring model	CI model	CI + Spring model
Connection between shank rod and rod K_{sr} (MN/m)	None	None	710	600~ 100,000	None	600~ 100,000

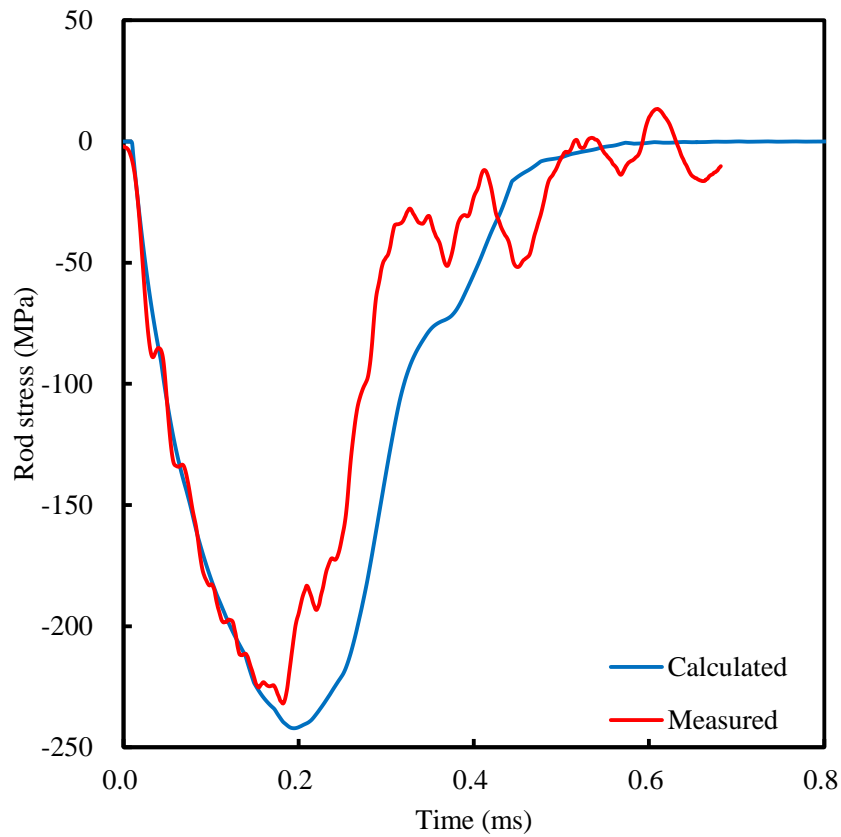
Table 3.2 Properties of the one-dimensional finite element model for the percussive long-hole drilling test in the ANSYS program.

Component	Number of elements	Element size (m)	Density (kg/m^3)	Young's modulus (GPa)
Piston	60			
Shank rod	43	0.01	7850	210
Rod	366			



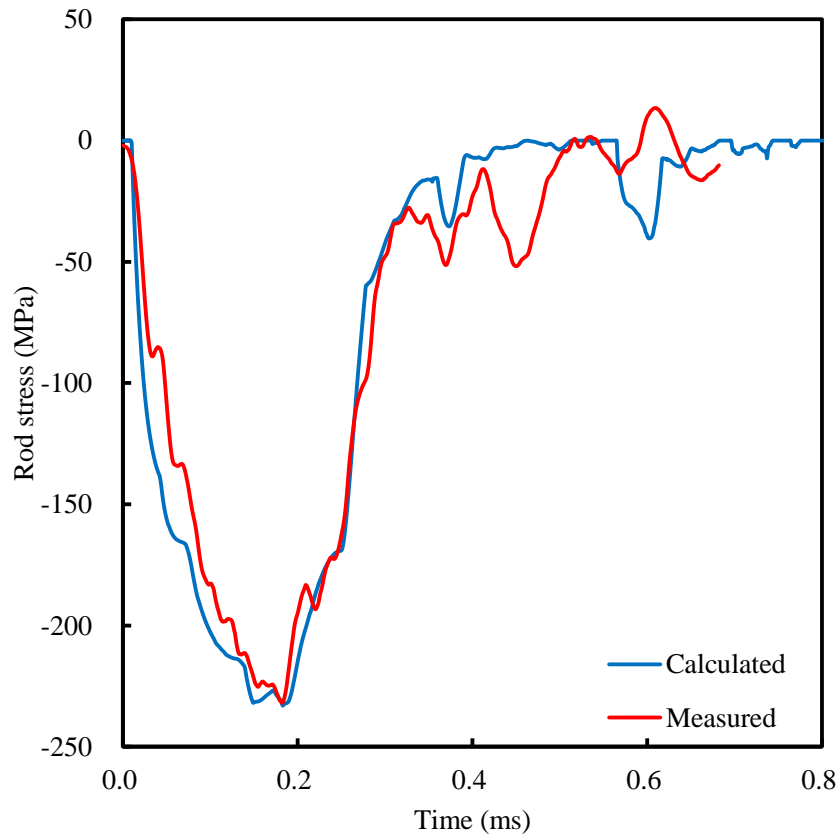
(a)

Fig. 3.1 Comparison between the calculated and measured rod stresses. The time when stress wave arrived at the strain gauge was set to be the origin. (a) $K_{ps} = 600$ MN/m, and circular cylinder models of the piston, shank rod and the rod. (b) $K_{ps} = 600$ MN/m, and actual shape models of the piston, shank rod and the rod. (c) $K_{ps} = 600$ MN/m, $K_{sr} = 710$ GN/m, actual shape models for the piston, shank rod and rod, and the spring model for the rod joint. (d) $K_{ps} = 10$ GN/m, $K_{sr} = 1$ GN/m, actual shape models for the piston, shank rod and rod, and the spring model for the rod joint. (e) $K_{ps} = 10$ GN/s, actual shape models of the piston, shank rod and the rod, and the CI model for the rod joint. (f) $K_{ps} = 10$ GN/s, $K_{sr} = 1$ GN/s, and actual shape models of the piston, shank rod and the rod, and the CI + spring model for the rod joint.



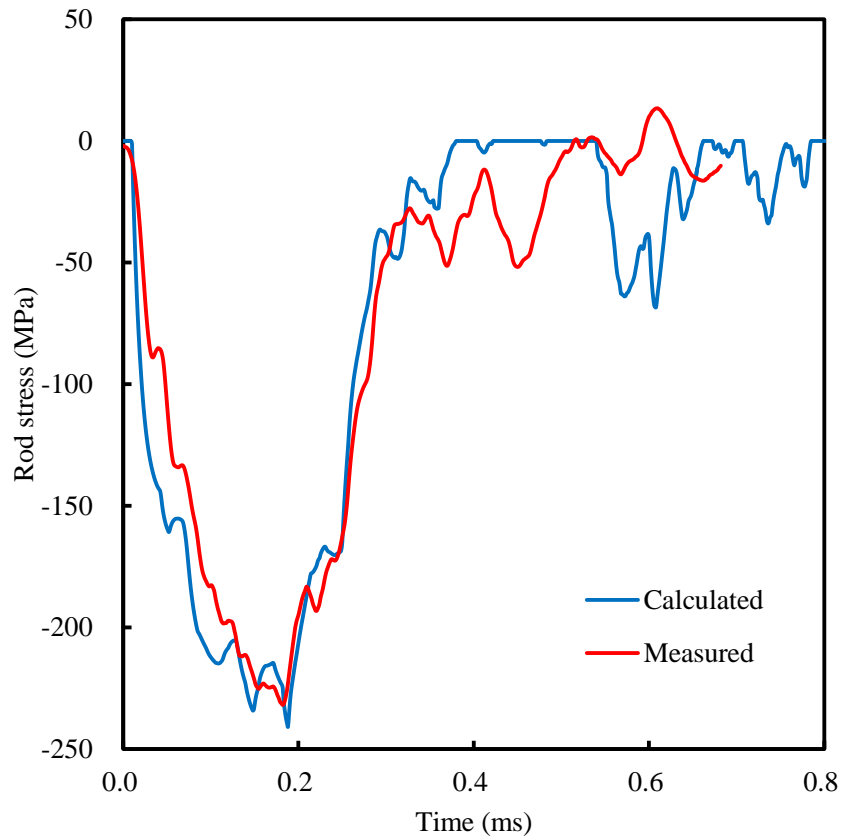
(b)

Fig. 3.1 (Continued) Comparison between the calculated and measured rod stresses. The time when stress wave arrived at the strain gauge was set to be the origin. (a) $K_{ps} = 600$ MN/m, and circular cylinder models of the piston, shank rod and the rod. (b) $K_{ps} = 600$ MN/m, and actual shape models of the piston, shank rod and the rod. (c) $K_{ps} = 600$ MN/m, $K_{sr} = 710$ GN/m, actual shape models for the piston, shank rod and rod, and the spring model for the rod joint. (d) $K_{ps} = 10$ GN/m, $K_{sr} = 1$ GN/m, actual shape models for the piston, shank rod and rod, and the spring model for the rod joint. (e) $K_{ps} = 10$ GN/s, actual shape models of the piston, shank rod and the rod, and the CI model for the rod joint. (f) $K_{ps} = 10$ GN/s, $K_{sr} = 1$ GN/s, and actual shape models of the piston, shank rod and the rod, and the CI + spring model for the rod joint.



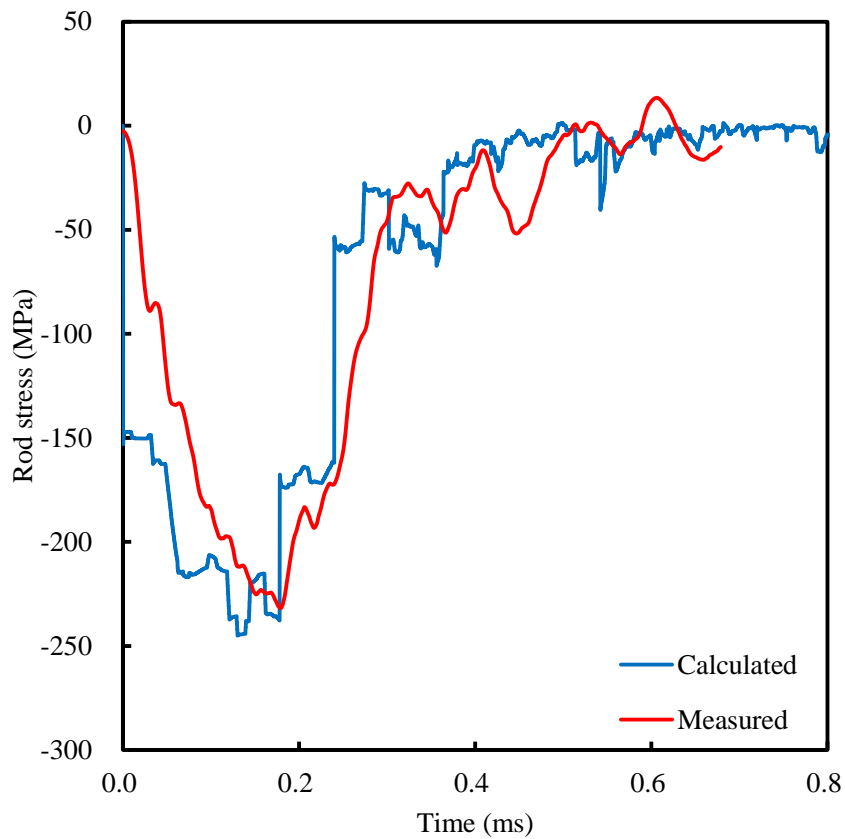
(c)

Fig. 3.1 (Continued) Comparison between the calculated and measured rod stresses. The time when stress wave arrived at the strain gauge was set to be the origin. (a) $K_{ps} = 600$ MN/m, and circular cylinder models of the piston, shank rod and the rod. (b) $K_{ps} = 600$ MN/m, and actual shape models of the piston, shank rod and the rod. (c) $K_{ps} = 600$ MN/m, $K_{sr} = 710$ GN/m, actual shape models for the piston, shank rod and rod, and the spring model for the rod joint. (d) $K_{ps} = 10$ GN/m, $K_{sr} = 1$ GN/m, actual shape models for the piston, shank rod and rod, and the spring model for the rod joint. (e) $K_{ps} = 10$ GN/s, actual shape models of the piston, shank rod and the rod, and the CI model for the rod joint. (f) $K_{ps} = 10$ GN/s, $K_{sr} = 1$ GN/s, and actual shape models of the piston, shank rod and the rod, and the CI + spring model for the rod joint.



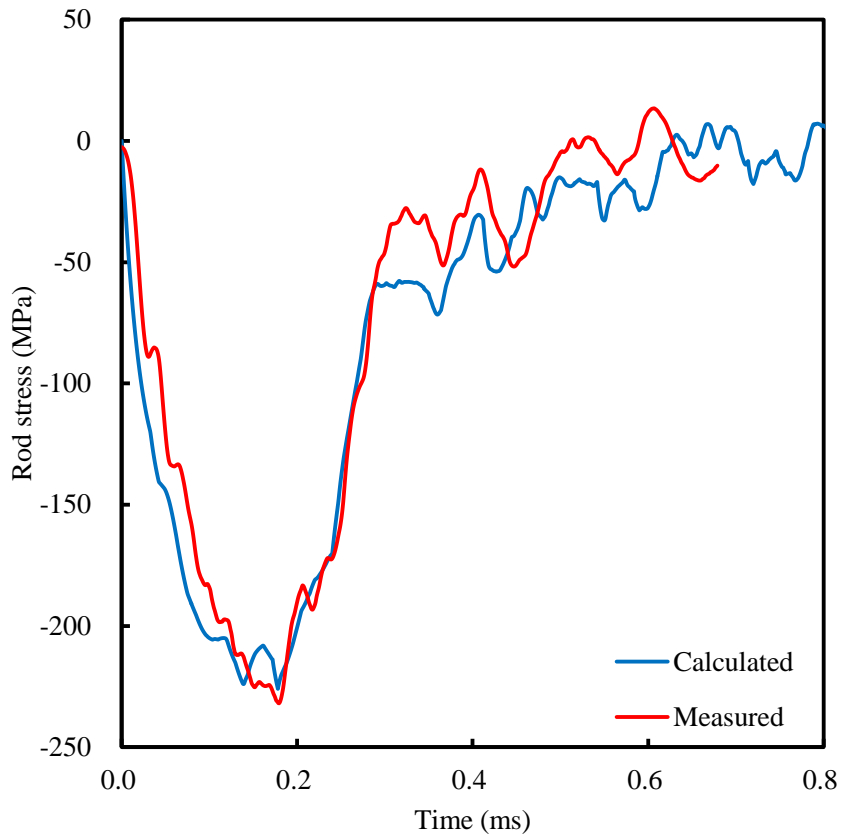
(d)

Fig. 3.1 (Continued) Comparison between the calculated and measured rod stresses. The time when stress wave arrived at the strain gauge was set to be the origin. (a) $K_{ps} = 600$ MN/m, and circular cylinder models of the piston, shank rod and the rod. (b) $K_{ps} = 600$ MN/m, and actual shape models of the piston, shank rod and the rod. (c) $K_{ps} = 600$ MN/m, $K_{sr} = 710$ GN/m, actual shape models for the piston, shank rod and rod, and the spring model for the rod joint. (d) $K_{ps} = 10$ GN/m, $K_{sr} = 1$ GN/m, actual shape models for the piston, shank rod and rod, and the spring model for the rod joint. (e) $K_{ps} = 10$ GN/s, actual shape models of the piston, shank rod and the rod, and the CI model for the rod joint. (f) $K_{ps} = 10$ GN/s, $K_{sr} = 1$ GN/s, and actual shape models of the piston, shank rod and the rod, and the CI + spring model for the rod joint.



(e)

Fig. 3.1 (Continued) Comparison between the calculated and measured rod stresses. The time when stress wave arrived at the strain gauge was set to be the origin. (a) $K_{ps} = 600$ MN/m, and circular cylinder models of the piston, shank rod and the rod. (b) $K_{ps} = 600$ MN/m, and actual shape models of the piston, shank rod and the rod. (c) $K_{ps} = 600$ MN/m, $K_{sr} = 710$ GN/m, actual shape models for the piston, shank rod and rod, and the spring model for the rod joint. (d) $K_{ps} = 10$ GN/m, $K_{sr} = 1$ GN/m, actual shape models for the piston, shank rod and rod, and the spring model for the rod joint. (e) $K_{ps} = 10$ GN/s, actual shape models of the piston, shank rod and the rod, and the CI model for the rod joint. (f) $K_{ps} = 10$ GN/s, $K_{sr} = 1$ GN/s, and actual shape models of the piston, shank rod and the rod, and the CI + spring model for the rod joint.



(f)

Fig. 3.1 (Continued) Comparison between the calculated and measured rod stresses. The time when stress wave arrived at the strain gauge was set to be the origin. (a) $K_{ps} = 600$ MN/m, and circular cylinder models of the piston, shank rod and the rod. (b) $K_{ps} = 600$ MN/m, and actual shape models of the piston, shank rod and the rod. (c) $K_{ps} = 600$ MN/m, $K_{sr} = 710$ GN/m, actual shape models for the piston, shank rod and rod, and the spring model for the rod joint. (d) $K_{ps} = 10$ GN/m, $K_{sr} = 1$ GN/m, actual shape models for the piston, shank rod and rod, and the spring model for the rod joint. (e) $K_{ps} = 10$ GN/s, actual shape models of the piston, shank rod and the rod, and the CI model for the rod joint. (f) $K_{ps} = 10$ GN/s, $K_{sr} = 1$ GN/s, and actual shape models of the piston, shank rod and the rod, and the CI + spring model for the rod joint.

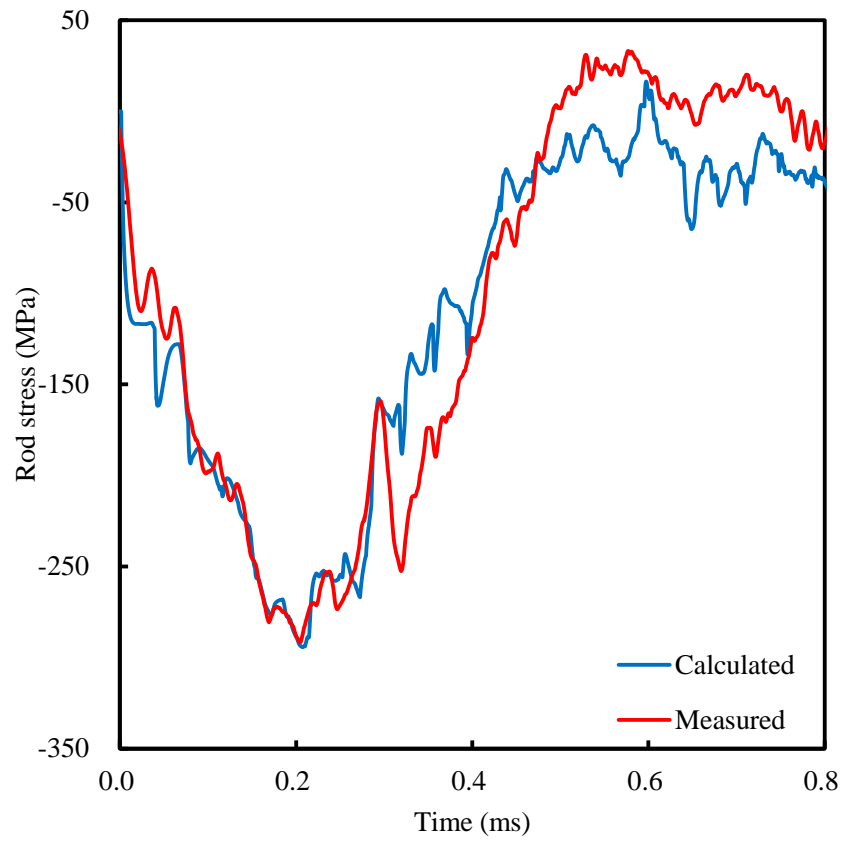
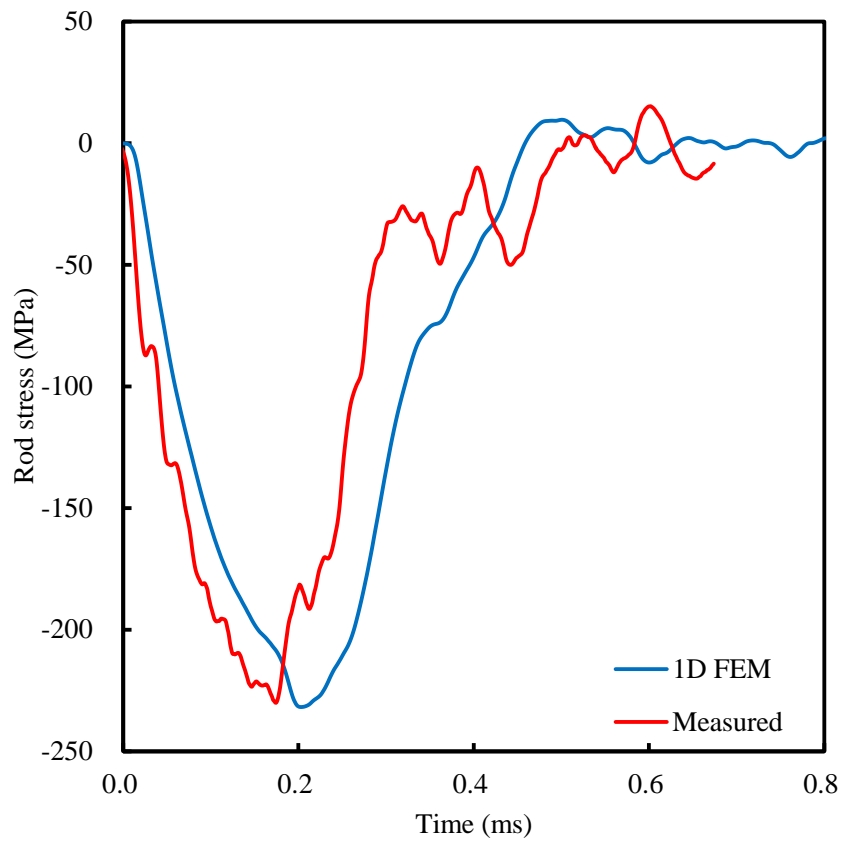
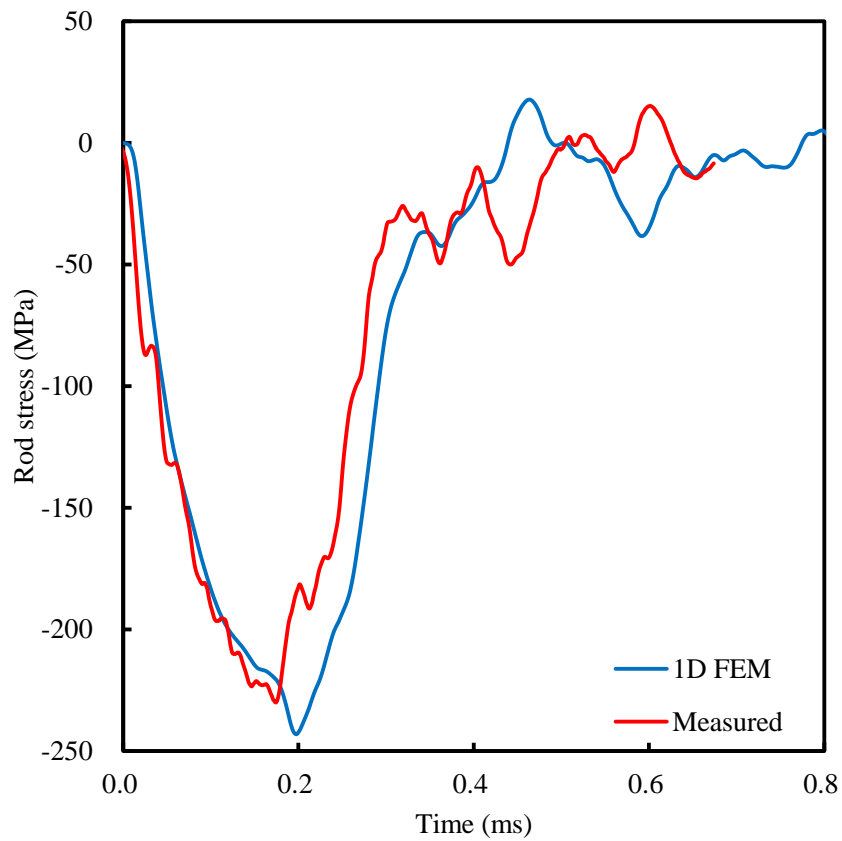


Fig. 3.2 Measured (red) and calculated (blue) rod stresses at the measurement point on the rod of HD712.



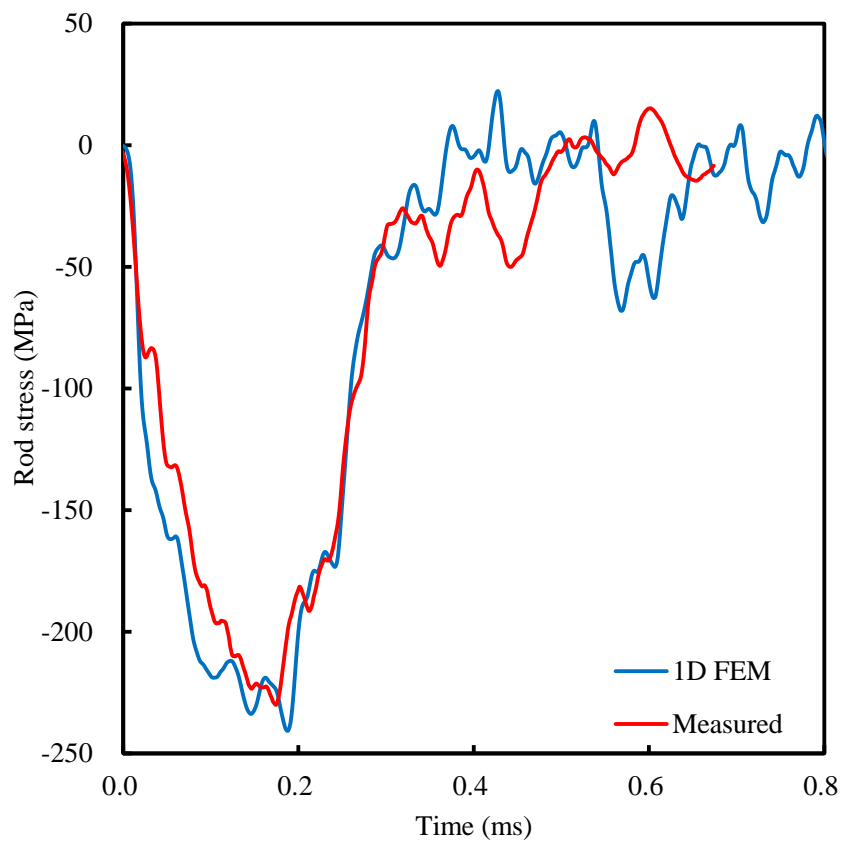
(a)

Fig. 3.3 Comparison between the measured rod stress (red) and the one (blue) calculated with 1D finite element model of percussive drilling. (a) $K_{ps} = 600$ MN/m. (b) $K_{ps} = 1$ GN/m. (c) $K_{ps} = 10$ GN/m. (d) $K_{ps} = 100$ GN/m.



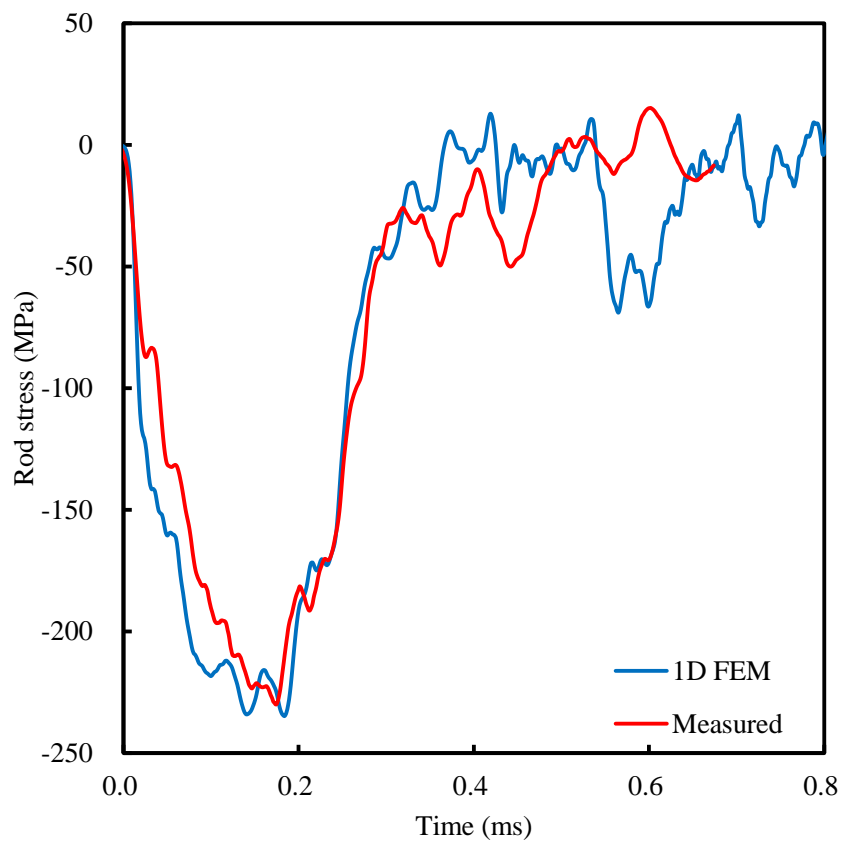
(b)

Fig. 3.3 (Continued) Comparison between the measured rod stress (red) and the one (blue) calculated with 1D finite element model of percussive drilling. (a) $K_{ps} = 600$ MN/m. (b) $K_{ps} = 1$ GN/m. (c) $K_{ps} = 10$ GN/m. (d) $K_{ps} = 100$ GN/m.



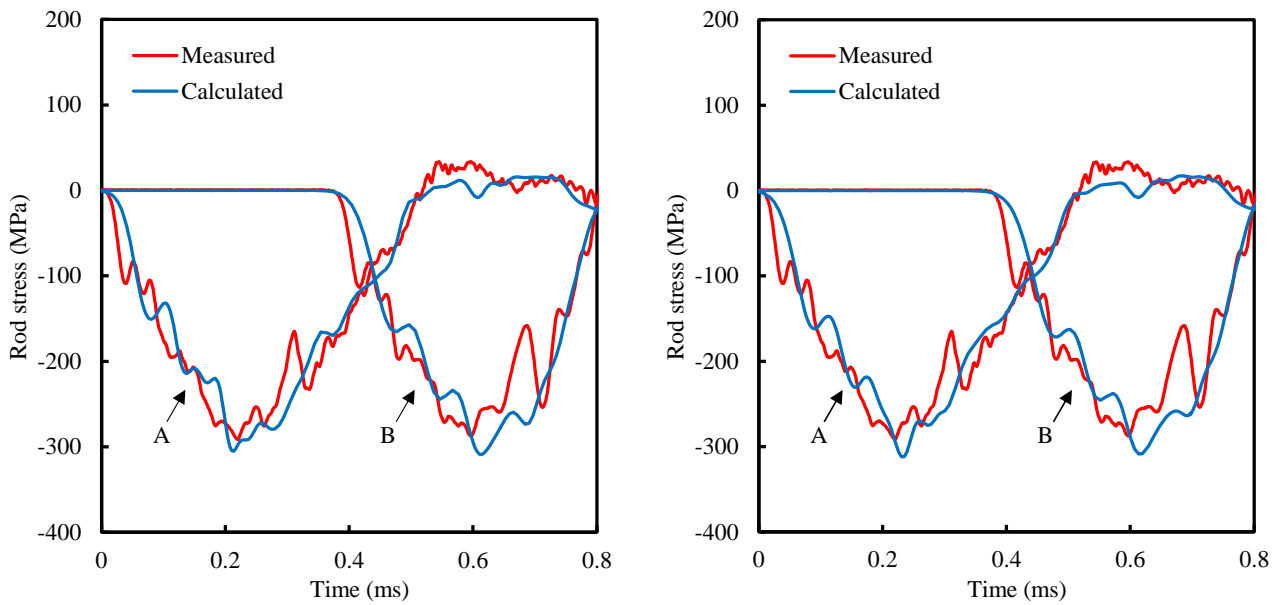
(c)

Fig. 3.3 (Continued) Comparison between the measured rod stress (red) and the one (blue) calculated with 1D finite element model of percussive drilling. (a) $K_{ps} = 600$ MN/m. (b) $K_{ps} = 1$ GN/m. (c) $K_{ps} = 10$ GN/m. (d) $K_{ps} = 100$ GN/m.



(d)

Fig. 3.3 (Continued) Comparison between the measured rod stress (red) and the one (blue) calculated with 1D finite element model of percussive drilling. (a) $K_{ps} = 600$ MN/m. (b) $K_{ps} = 1$ GN/m. (c) $K_{ps} = 10$ GN/m. (d) $K_{ps} = 100$ GN/m.



(a)

Fig. 3.4 Comparison between the measured (red) and calculated (blue) rod stresses. The used model is the axisymmetric finite element model. The calculated rod stresses in the left and right figures are computed with the coarse-mesh and fine-mesh axisymmetric finite element models, respectively. (a) Variable time step size = $1 \mu\text{s} \sim 10 \mu\text{s}$. (b) Variable time-step size = $0.1 \mu\text{s} \sim 1 \mu\text{s}$. (c) Variable time-step size = $0.05 \mu\text{s} \sim 0.5 \mu\text{s}$.

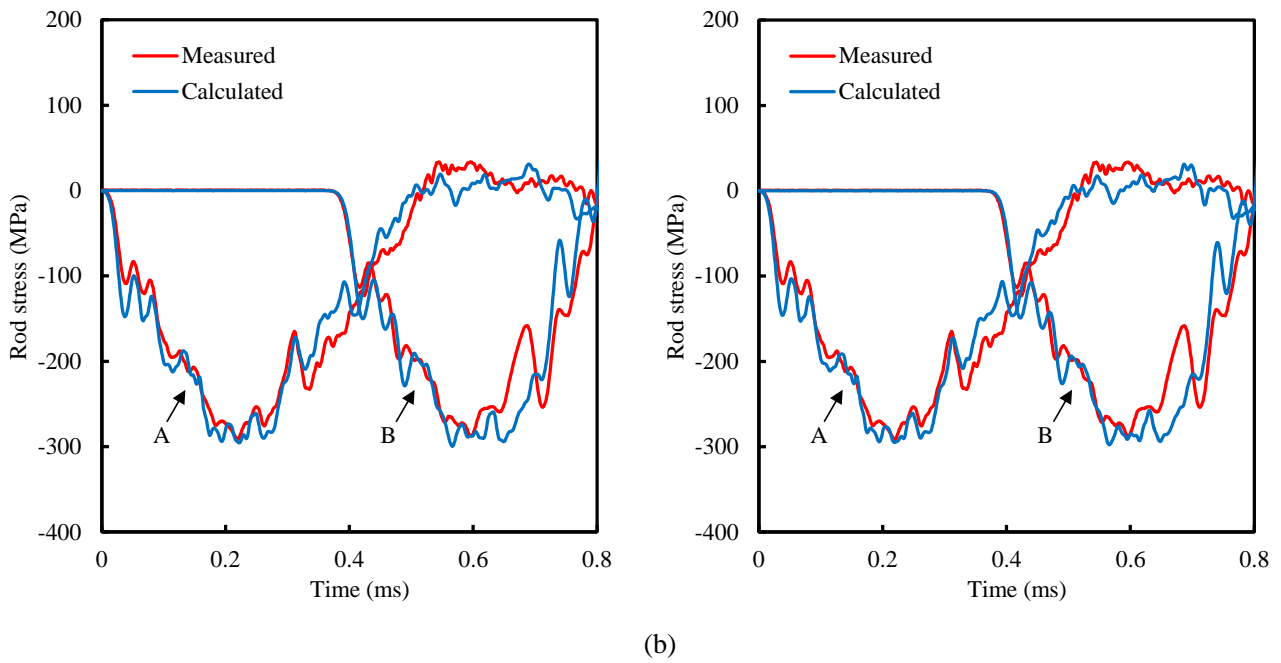


Fig. 3.4 (Continued) Comparison between the measured (red) and calculated (blue) rod stresses. The used model is the axisymmetric finite element model. The calculated rod stresses in the left and right figures are computed with the coarse-mesh and fine-mesh axisymmetric finite element models, respectively. (a) Variable time step size = $1 \mu\text{s} \sim 10 \mu\text{s}$. (b) Variable time-step size = $0.1 \mu\text{s} \sim 1 \mu\text{s}$. (c) Variable time-step size = $0.05 \mu\text{s} \sim 0.5 \mu\text{s}$.

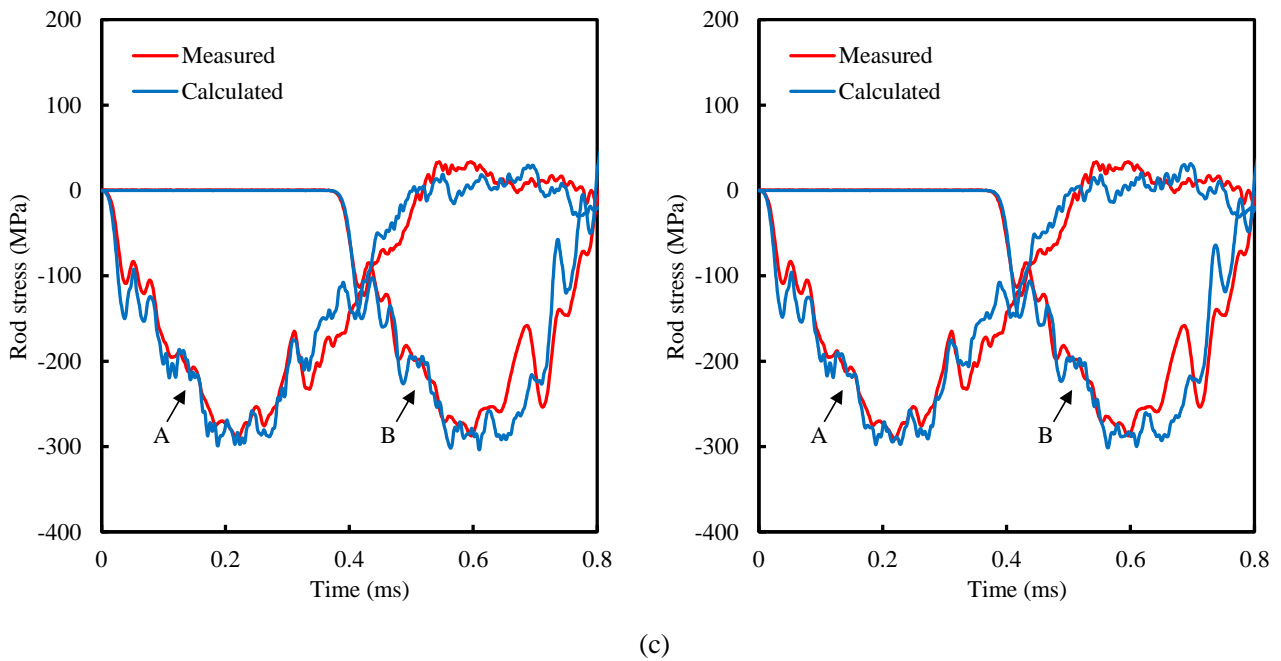
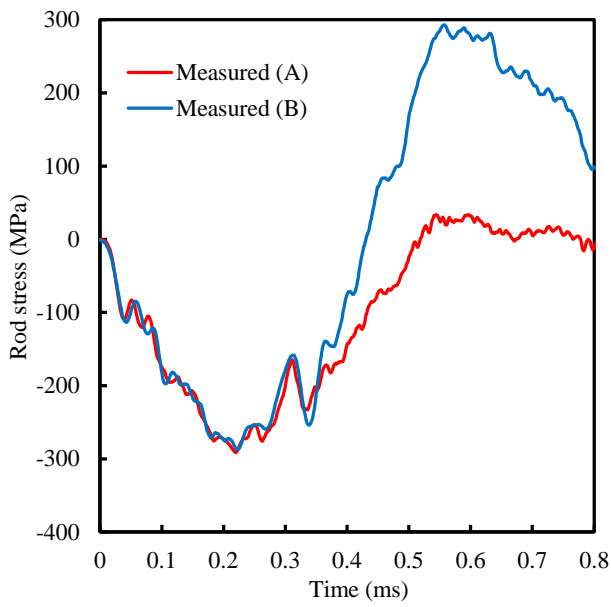
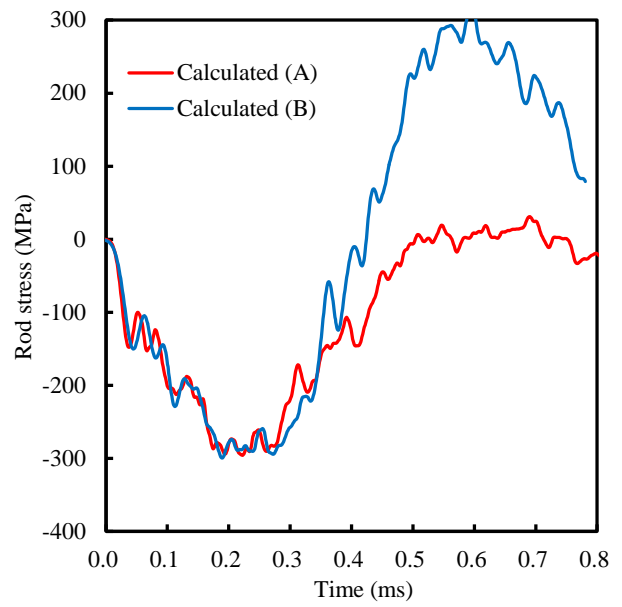


Fig. 3.4 (Continued) Comparison between the measured (red) and calculated (blue) rod stresses. The used model is the axisymmetric finite element model. The calculated rod stresses in the left and right figures are computed with the coarse-mesh and fine-mesh axisymmetric finite element models, respectively. (a) Variable time step size = $1 \mu\text{s} \sim 10 \mu\text{s}$. (b) Variable time-step size = $0.1 \mu\text{s} \sim 1 \mu\text{s}$. (c) Variable time-step size = $0.05 \mu\text{s} \sim 0.5 \mu\text{s}$.



(a)



(b)

Fig. 3.5 Comparison of rod stress at both A and B. The rod stress at B were shifted 0.376 ms horizontally. Rod stress in (a) and (b) are measured waves (Fukui et al. 2010) and computed ones based on the 3D axisymmetric finite element model, respectively.

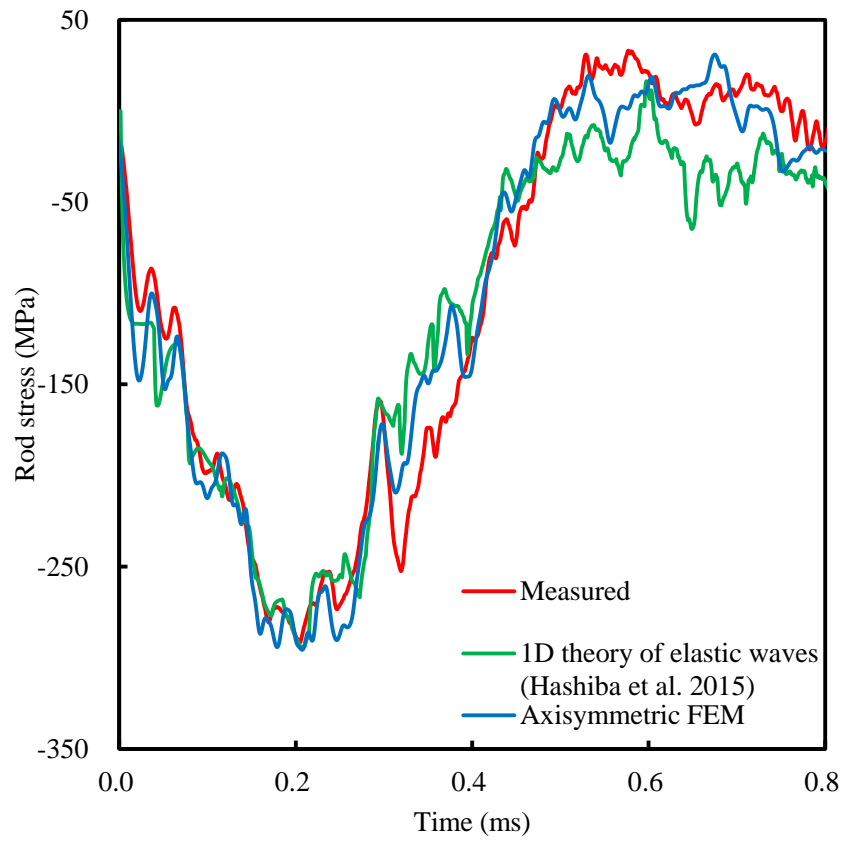


Fig. 3.6 Comparison among the measured (red), calculated with 1D model (green) and calculated with the axisymmetric finite element model (blue) waves.

Chapter 4 Force-penetration curves of a button bit generated during impact penetration into rock

4.1 Introduction

Numerical simulation is an effective approach to estimate the performance and efficiency of percussion rock drills (Lundberg and Okrouhlik 2006). The force-penetration relationship at the bit end affects the simulation results of the rock drill body and damper system, the piston stroke and speed, and blows frequency. The penetration per unit time depends on both the piston speed and blows frequency. Therefore it is important to know accurate force-penetration curves with a bit during impact penetration into rock. Many studies have been conducted on the impact penetration behavior of wing, conical and wedge bits (Simon 1964; Hustrulid and Fairhurst 1971a, 1971b, 1972a, 1972b; Goldsmith and Wu 1981; Karlsson et al. 1989). However, to date, little knowledge has been published about the penetration behavior of the button bit, which is commonly used for hard rock (Carlsson et al. 1990; Saksala et al. 2014).

Goldsmith and Wu (1981) conducted impact penetration tests with conical and wedge bits, and obtained force-penetration curves for them. In the tests, bit force was measured with strain gauges attached near the end of the bit, and penetration was measured with a capacitive displacement sensor attached to the rod. Recently, Saksala et al. (2014) conducted impact penetration tests on three button tips embedded into the end of a rod (a special triple-button bit) using the same measurement method as Goldsmith and Wu (1981). This measurement method requires strain gauges to be attached near the end of the bit for eliminating the influence of elastic wave reflection between the bit and rod. Therefore the method cannot be used when the bit is in a deep borehole. As the displacement sensor is attached at a distance from the bit end, this causes measurement errors during penetration and there is low durability to elastic stress waves. Moreover, the measured bit force and penetration exhibit temporal differences in this method. To overcome these drawbacks, Karlsson et al. (1989) conducted impact penetration tests with a wedge bit. They attached strain gauges to a rod at two points at a distance from the bit end, and calculated the bit force and penetration from the measured rod stress. This method, known as the two-point strain measurement (TPSM) method, was proposed by Lundberg and Henchoz (1977), and used in impact penetration tests by Karlsson et al. (1989).

Carlsson et al. (1990) applied the TPSM method to impact penetration tests with a button bit, and succeeded in obtaining force-penetration curves for the bit. Although the results are valuable for an actual button bit, their equipment had three major differences from an actual rock drill. 1) The piston in their equipment was a solid cylinder having the same diameter as the rod, while the piston in an actual rock drill has an intricate shape. 2) The piston collided directly with the rod in their equipment, whereas the piston in an actual rock drill collides with a shank rod that is connected to an extension rod via a rod joint, and this collision between the piston and the shank rod in an actual rock drill generates intricately shaped elastic waves. 3) The rod in their equipment was a solid cylinder, while an actual rod is a hollow cylinder (for flushing). The smaller cross-sectional area of the rod causes a larger difference in acoustic impedance between a rod and bit, and a higher wave reflection at the boundary. To increase the knowledge on the force-penetration curves during percussive rock drilling, it is important to assess the applicability of the TPSM method, to investigate the difference from simplified components, and to obtain precise force-penetration curves, using the same components in an actual rock drill.

In this study, the impact penetration behavior of a button bit was investigated by means of laboratory tests. Unnatural fluctuations were observed in the force-penetration curves calculated from the rod stress as measured with the TPSM method. Thereafter the reason for this was elucidated, and a data correction method was proposed using a numerical simulation. The correction method was applied to the measured rod stress, and accurate force-penetration curves with a button bit were obtained from the impact penetration tests.

4.2 Problems in the calculation of a force-penetration curve

Fig. 4.1 shows a set of rod stresses measured at *A* and *B* with blue and red solid curves, respectively, in the SBIP test mentioned in Section 2.4.4. In this study, the time when the elastic wave arrived at *A* was set to the origin. The rod stress measured at *B* is left-shifted by 0.376 ms along the horizontal axis, and shown with a broken curve. The compressive rod stress was measured at *B* 0.376 ms after being measured at *A*, and the elastic wave velocity 5080 m/s was obtained by dividing the distance of 1910 mm by the arrival time difference of 0.376 ms between *A* and *B*. The rod stress measured at *B* was overlapped with the elastic wave reflected at the bit end after about 0.7 ms. Although the temporal change in rod stress at *B* is similar to that at *A* before 0.3 ms, the high-frequency components do not

closely agree with each other, which could be caused by frequency dispersion or the three-dimensional effect of elastic wave propagation (Kolsky 1963). Because Eq. (2.8) assumes that the rod stresses at A and B perfectly correspond to each other, the difference in rod stresses probably produces some calculation errors.

The rod and bit are subdivided into elements in the calculation with the TPSM method mentioned in Section 2.4.5. Fig. 4.2 shows a schematic illustration and two calculation models for the rod and bit. The rod and bit are connected with external and internal threads, small sections of which are in contact with each other, and the rod end is in firm contact with the bit, as shown in Fig. 4.2 (a). Stress waves propagate mainly through the contact face not through the threads. Threaded bit model in Fig. 4.2 (b) assumes that the threaded portion of the bit is separate from the rod, and can be used in the simulation of elastic wave propagation in Section 4.3. However, the temporal change in the strain on the threaded portion of the bit, which cannot be measured in the SBIP test, is required for the calculation of force-penetration curves with the TPSM method. Strain measurement at the bit is more difficult than at the rod due to the complex and non-axisymmetric geometry of the bit. Therefore unified bit model in Fig. 4.2 (c), which unifies rod and bit, was used to calculate force-penetration curves with the TPSM method in the same way as Carlsson et al. (1990). The length of an element was set to 5.08 mm, through which the elastic wave at a velocity of 5080 m/s propagates in 1 μ s, and the length is much shorter than the wave length of about 2.5 m.

Fig. 4.3 (a) shows the bit force F and the penetration u , respectively, in Eq. (2.12), calculated with the TPSM method. The rod stresses at A and B in the experiment, shown with blue and red solid curves, respectively, in Fig. 4.1, were input, and unified bit model was used in the calculation of Fig. 2.11 (b). The elastic wave passed through A and B , and arrived at the bit end after about 0.5 ms. The curve of the bit force, the blue curve in Fig. 4.3 (a), shows many fluctuations before the arrival of the elastic wave, which are caused by the difference in the stresses measured at A and B , the solid blue and broken red curves in Fig. 4.3. After the arrival of the elastic wave, the penetration increases smoothly. In contrast, the bit force shows a bumpy curve, which is caused by not only the differences in the stresses measured at A and B , but also by the mismatch between the actual bit and unified bit model used in the calculation. Fig. 4.3 (b) shows the force-penetration curve with a blue curve, which has many large fluctuations. It is impossible to obtain properties the slope, peak force and penetration from the curve.

Carlsson et al. (1990) reported “the threaded combination of rod and bit behaves nearly as a homogeneous elastic rod,” which was probably due to the slightly simpler components they used compared to those in this study. They conducted their tests with a Sandvik standard rod-bit system, but the system includes a cylindrical piston and excludes a shank rod and a rod joint. The same components as an actual rock drill, which generate intricately shaped elastic waves, were used in this study, and therefore it was difficult to obtain force-penetration curves with the TPSM method.

4.3 Consideration of the calculation method of a force-penetration curve with numerical simulation

A new calculation method to obtain a force-penetration curve from the measured rod stresses in the SBIP test was investigated by using a numerical simulation based on the theory of elastic wave propagation. The elastic wave propagation from A to B was simulated on the assumption of a predetermined force-penetration curve, and the calculation method was examined to obtain the curve from the rod stresses at A and B in the simulation.

The rod stress at B was simulated using Eq. (2.9) from the rod stress measured at A on the assumption that the force-penetration relation at the bit end is the broken black curve in Fig. 4.3 (b), which has slopes of 250 MN/m in loading and 1250 MN/m in unloading. Threaded bit model in Fig. 4.2 (b) was used in the simulation due to its similarity to an actual rod and bit. The simulated result is shown with a green curve in Fig. 4.4, which closely agrees with the rod stress measured at B , shown with a red curve. One-dimensional wave propagation was assumed in the simulation, and therefore the rod stress at B left-shifted by 0.376 ms, perfectly corresponding to the rod stress at A before the arrival of the elastic wave reflected at the bit end.

Fig. 4.5 shows the bit force and penetration with thick red curves calculated with the TPSM method. The rod stresses at A and B in the simulation shown with blue and green curves in Fig. 4.4 were input, and unified bit model was used. As shown in Fig. 4.5 (b), the penetration closely agrees with the result calculated from the rod stresses at A and B in the experiment shown with a blue curve. As shown in Fig. 4.5 (a), the bit force is zero before around 0.5 ms when the elastic wave arrives at the bit end, which is different from the result shown with a thick blue curve. This is because the temporal changes in the rod stresses at A and B in the simulation closely agree with each other

before the arrival of the elastic wave reflected at the bit end. However, after 0.5 ms the bit force has similar fluctuations to the result shown with a thick blue curve. Accordingly the force-penetration curve, the red curve in Fig. 4.6, also fluctuated and is far from the assumed curve, the broken black curve. The fluctuations in the blue curves in Figs. 4.5 (a) and 4.6 are caused by the difference between an actual bit and unified bit model, as mentioned in Section 4.2. In contrast, the fluctuations in the red curves in the figures are caused by the difference between threaded bit model in the simulation of the rod stress at B and unified bit model in the calculation of the force-penetration curve. If the same model, such as unified bit model, is used in the calculations of rod stress at B and the force-penetration curve, the fluctuations do not appear in the curves. However, threaded bit model could not be used in the calculation of the force-penetration curve because the stress on the thread portion of the bit could not be measured in the SBIP test, as mentioned in Section 4.2.

To eliminate the fluctuations in the curves, a free bit end (FBE) test was simulated, in which the piston collides with the shank rod with the bit as a free end. The rod stress at B was simulated by Eq. (2.9) from the rod stress measured at A on the assumption of the FBE test. Threaded bit model in Fig. 4.2 (b) was used in the simulation. The simulated result is shown with a black curve in Fig. 4.4, which shows a larger tensile wave reflected at the bit end than that in the SBIP test, shown with a green curve.

Fig. 4.5 (a) shows the bit force with a thin red curve calculated with the TPSSM method. The rod stresses at A and B in the simulation, shown with blue and black curves, respectively, in Fig. 4.4 were input, and unified bit model was used. After the arrival of the elastic wave at the bit end, the bit force in the FBE test should be zero, but exhibits similar fluctuations to that in the SBIP test shown with a thick red curve. As mentioned above, the fluctuations are caused by the difference between threaded bit model in the simulation of the rod stress at B and unified bit model in the calculation of the force-penetration curve. Because the fluctuations are probably generated by the same cause in both the simulations of the FBE and SBIP tests, the author expects that the fluctuations can be eliminated by subtracting the bit force in the FBE test from that in the SBIP test. Figs. 4.5 (a) and 4.6 show the bit force and force-penetration curve with black curves corrected with the subtraction. The figures show that the many fluctuations in the bit force and force-penetration curve are eliminated with the correction. Comparing the corrected and assumed force-penetration curves, the solid and broken black curves in Fig. 4.6 the curves are close to each other.

This section demonstrated an example of numerical simulation on the assumption of a predetermined force-penetration curve. Additional calculations showed that the correction method could be applied to the force-penetration curves ranging from soft to hard rocks. The results of the numerical simulation indicate that the bit force calculated with the TPSM method in the SBIP test can be corrected by subtracting the bit force in the FBE test. The correction method is applied when the contact condition between the rod and bit, which affects the elastic wave propagation, is similar in both the SBIP and FBE tests. The rod stress at B in both the SBIP and FBE tests was calculated from the same rod stress measured at A in the numerical simulation. In contrast, the rod stress at A varies with each blow, and this variation needs to be verified in the application of the correction method to the actual SBIP test.

4.4 Results and discussion of the SBIP tests

4.4.1 Force-penetration curves

An FBE test was conducted, and rod stress was measured in the same way as in the SBIP test. Fig. 4.7 shows the three results in the SBIP tests and a result in the FBE test so the author can examine the variation from blow to blow. The blue curves are the same as the rod stresses measured at A and B in Figs. 4.1 and 4.4. The rod stresses before the arrival of the elastic waves reflected at the bit end, 0-1.2 ms at A and 0-0.8 ms at B , are similar in both the SBIP and FBE tests. The small differences in the rod stresses at A or B between tests are probably caused by the presence or absence of thrust force, or by the variation in piston velocity in each blow. As shown by the colored curves, the rod stress at B varied with blows after about 0.8 ms, when the reflected wave overlaps. This variation with blows is probably caused by the contact conditions between the bit and rock, or by a fault in the rock; for example, the tensile wave reflected at the bit end becomes large when the bit is not in close contact with rock.

The bit forces were calculated from the four results in Fig. 4.7 using unified bit model with the TPSM method, and they are shown in Fig. 4.8 (a). The calculated bit forces closely agree with each other before about 0.7 ms, as expected from the high reproducibility in Fig. 4.7. Differences between the SBIP and FBE tests, and variations with blows in the SBIP tests are observed after 0.7 ms, but the fluctuations are similar to each other. The bit forces in the SBIP tests were corrected by subtracting the bit force in the FBE test, and they are shown in Fig. 4.8 (b). Many fluctuations were eliminated, as was the

case in the numerical simulation. The force-penetration curves before and after the correction is shown in Figs. 4.9 (a) and (b), which shows a significant reduction in fluctuations in the curves. The procedure is shown as correction in Fig. 4.10. The correction method eliminated the fluctuations caused by the error factors such as the mismatch between the actual bit-rod connection and unified bit model, the frequency dispersion and three-dimensional effect of elastic wave propagation. However, unnatural changes in the slopes just before the peaks are observed, as circled in Figs. 4.8 (b) and 4.9 (b). If the changes in the slopes of the force-penetration curves are caused by rock chipping, the changes occur at random times. However, Fig. 4.8 (b) shows that abrupt changes in the slopes are observed at the same time, and therefore the correction is probably insufficient for some reason.

To understand the reason, the bit force in the FBE test, the black curve in Fig.4.8 (a), is shown with a thin blue curve in Fig. 4.5 (a). As mentioned in Section 4.3, the black curve in Fig. 4.5 (a) is the difference between the thick and thin red curves calculated from the stresses at *A* and *B* in the simulation, and the curve has no fluctuations. In contrast, the blue curve in Fig. 4.8 (b) is the difference between the thick and thin blue curves in Fig. 4.5 (a) calculated from the stresses at *A* and *B* in the experiment, and the curve has many fluctuations. The small peaks in Fig. 4.5 (a) closely agree with each other in the thick blue and red curves, but not in the thin blue and red curves. This is probably because the elastic wave propagation at the connection between the rod and bit changes in the SBIP and FBE tests due to the change in the contact conditions. In view of these results, the thin red curve in Fig. 4.5 (a) was subtracted from the colored curves in Fig. 4.8 (a) between 0.8 and 1.0 ms when the bit force is high in the SBIP tests. The corrected bit forces and force-penetration curves are shown in Figs. 4.8 (c) and 4.9 (c), respectively, which show that the fluctuations and abrupt changes before the peaks are eliminated from Figs. 4.8 (b) and 4.9 (b). The procedure is shown as additional correction in Fig. 4.10. The additional correction with threaded bit model is just for the threaded bit-rod connection. The correction method was conceived using the simulation for the blue curve in Fig. 4.7, which shows the reflected wave mainly compressive. The method could be applied to the red and green curves which show larger tensile reflected waves, as expected from the numerical simulation.

The corrected force-penetration curves in the SBIP tests indicate that the curves are concave upward and that the slope is much larger in unloading than in loading. Even though actual rock drill components were used in this

study, the authors believe that the curves are more precise than those with the standard rod-bit system in Carlsson et al. (1990), in which large fluctuations were observed near the origin. Previous studies showed that the force-penetration curves for granite in static penetration tests with a button tip (Miller 1968) and a conical tip (Dutta 1972; Lundberg 1974) are not smooth due to rock chipping in comparison with the curves in Fig. 4.9 (c). Okubo et al. (1995) reported that the force-penetration curve for granite with a button bit in a static penetration test had three abrupt changes in the slope before reaching the peak force, and that these changes were probably caused by rock chipping. The force-penetration curves are smoother in the SBIP tests than those in static penetration tests, which indicates that impact penetration is not accompanied by large rock chipping. The mechanism of impact and static penetration behavior is an issue to be resolved in a future study.

4.4.2 Impact penetration behavior

Force-penetration curves were obtained using the correction method in Fig. 4.9 (c) from the 42 SBIP tests, except for the ninth test for which there was a failure in measurement. The curves do not show large fluctuations and are similar to the three curves in Fig. 4.9 (c). As shown in Fig. 4.11, the following data were calculated: peak force, maximum, final and elastic penetrations; and three energies: E_1 (crushing energy), E_2 (elastic strain energy) and E (the sum of the energies).

The changes in the data with blows are shown in Fig. 4.12. The peak force is shown in Fig. 4.12 (a). The data increase and decrease alternately with blows. It is noteworthy in the simulation that the force-penetration curves are not straight but concave upward in both loading and unloading.

The three penetrations (maximum, final and elastic) are shown in Fig. 4.12 (b), in which only the elastic penetration is its threefold value.

The three energies (E_1 , E_2 and E) are shown in Fig. 4.12 (c), in which only E_2 is its twofold value. In the SBIP test, E_1 cannot be obtained from the difference between the input and reflected elastic wave energies on the rod because the elastic waves overlapped at both A and B . It is a significant achievement in this study that the author obtained these energies from the integral of the force-penetration curves.

The data obtained from the force-penetration curves are listed in Table 4.1.

The SBIP tests were conducted under constant conditions, with the coefficient of variation being about 3 % for the impact energy calculated from the rod stress measured at *A*. The coefficients of variation for the data in Table 4.1 are much larger than that of the input energy. It is probable that the contact conditions between the bit and rock vary with blows, and that they affect the large variation in the initial slope. The other factors for the variation are probably variations in rock properties and damage to the rock caused by blows. The peak force and penetrations show an alternate increase and decrease, which indicate that high and low degrees of damage alternately occur in rock with blows. In the SBIP tests, the bit was rotated 25.7 for each blow, and therefore the bit made one rotation every 14 blows. However, a periodic trend is not observed, which is probably because the damage is spread around the penetration by tips, and because the slope of the rock surface varies even if the tips penetrate at the same locations. A single force-penetration curve was used in previous drilling simulations, and a simulation with consideration of the variation in the curves will be discussed in Chapter 6.

4.5 Conclusions

In this chapter, the impact penetration behavior of a button bit was investigated based on the SBIP tests introduced in Section 2.4.4. SBIP tests provided highly reproducible results under constant blow conditions and with tightening of the threads after each blow. Unnatural fluctuations were observed in the force-penetration curves calculated with the TPSM method. This is probably due to not only the differences in the rod stresses measured at the two points on the rod, but also to the mismatch between the actual bit and the calculation model. The data correction method, in which the bit force calculated in the FBE test is subtracted from that in the SBIP test, was proposed using a numerical simulation.

The correction method was applied to the measured rod stresses, and the force-penetration curves were improved remarkably. However, the slopes of the curves changed unnaturally just before the peaks, which was probably due to the change in the contact conditions at the connection between the rod and bit in the SBIP and FBE tests. Thereafter, the bit force calculated in the simulation of the FBE test was subtracted from the bit force calculated from the measured rod stresses in the SBIP test when the bit force was high as circled in Fig. 4.8 (b) in the SBIP test. The additional correction with threaded bit model is just for the threaded bit-rod connection used in this study. The corrected force-penetration curves are smoother in the SBIP tests

than those in static penetration tests in previous studies, which indicates that impact penetration is not accompanied by large rock chipping.

The peak force, slopes, penetrations and three types of energies were obtained from the force-penetration curves in more than 40 SBIP tests. The variations in the force-penetration curves are probably caused by the contact conditions between the bit and rock, the rock properties and damage to the rock with each blow. The data correction method proposed in this chapter is based on the precise testing results and not on the precise calculation model. The important issues in future studies are to conduct the SBIP tests with the bits different in size and threads, to examine the effects of the shape of the rod and bit on the force-penetration curves, and to investigate the applicability of the method to the drilling components of different manufacturers. In situ rock drilling does not provide precise drilling data under constant conditions, and therefore it is useful to predict the elastic wave propagation and penetration behavior with precise calculation models.

References

Carlsson J., Sundin K.G., Lundberg B. (1990): A method for determination of in-hole dynamic force-penetration data from two-point strain measurement on a percussive drill rod. *Int. J. Rock Mech. Min. Sci. & Geomech. Abstr.*, vol. 27, pp. 553-558.

Dutta P. K. (1972): A theory of percussive drill bit penetration, *Int. J. Rock Mech. Min. Sci.*, vol. 9, pp. 543-567.

Goldsmith W., Wu W. Z. (1981): Response of rocks to impact loading by bars with pointed ends, *Rock Mech*, vol. 13, pp. 157-184.

Hustrulid W. A., Fairhurst C. (1971): A theoretical and experimental study of the percussive drilling of rock part I - theory of percussive drilling, *Int. J. Rock Mech. Min. Sci.*, vol. 8, pp. 311-333.

Hustrulid W. A., Fairhurst C. (1971): A theoretical and experimental study of the percussive drilling of rock part II - force-penetration and specific energy determinations, *Int. J. Rock Mech. Min. Sci.*, vol. 8, pp. 335-356.

Hustrulid W. A., Fairhurst C. (1972): A theoretical and experimental study of the percussive drilling of rock part III - experimental verification of the mathematical theory, *Int. J. Rock Mech. Min. Sci.*, vol. 9, pp. 417-429.

Hustrulid WA, Fairhurst C. (1972): A Theoretical and Experimental Study of the Percussive Drilling of Rock Part IV - application of the Model to Actual Percussion Drilling, *Int. J. Rock Mech. Min. Sci.*, vol. 9, pp. 431-449.

Karlsson L. G., Lundberg B., Sundin K. G. (1989): Experimental study of percussive process for rock fragmentation, *Int. J. Rock Mech. Min. Sci. & Geomech. Abstr.*, vol. 26, pp. 45-50.

Lundberg B., Henchoz A. (1977): Analysis of elastic waves from two-point strain measurement, *Experimental Mechanics*, vol. 17, pp. 213-218.

Lundberg B. (1974): Penetration of rock by conical indenters, *Int. J. Rock Mech. Min. Sci. & Geomech. Abstr.*, vol. 11, pp. 209-214.

Lundberg B. (1982): Microcomputer simulation of stress wave energy transfer to rock in percussive drilling, *Int. J. Rock Mech. Min. Sci. &*

Geomech. Abstr., vol. 19, pp. 229-239.

Lundberg B., Okrouhlik M. (2006): Efficiency of a percussive rock drilling process with consideration of wave energy radiation into the rock, *Int. J. Impact Eng.*, vol. 32, pp. 1573-1583.

Miller M. H., Sikarskie D. J. (1968): On the penetration of rock by three-dimensional indentors, *Int. J. Rock Mech. Min. Sci.*, vol. 5, pp. 375-398.

Kolsky H. (1963): *Stress waves in solids*. Chapter III, New York, Dover Publications Inc.

Okubo S., Ota A., Akiyama M., Fukui K. (1995): Static penetration test with a button bit, *Proceedings of the fall meeting of MMIJ 1995*, pp. 174 (in Japanese).

Saksala T., Gomon D., Hokka M., Kuokkala V. T. (2014): Numerical and experimental study of percussive drilling with a triple-button bit on kuru granite, *Int. J. Impact Eng.*, vol. 72, pp. 56-66.

Simon R. (1964): Transfer of the stress wave energy in the drill steel of a percussive drill to the rock, *Int. J. Rock Mech. Min. Sci.*, vol. 1, pp. 397-411.

Table 4.1 Data obtained from the force-penetration curves in the SBIP tests

		Average	Standard deviation	Coefficient of variation (%)
Peak force F_{max} (kN)		457	45.1	9.88
Penetration (mm)	Maximum u_m	2.15	0.236	11.0
	Final u_f	1.79	0.272	15.2
	Elastic u_e	0.364	0.0582	16.0
Energy (J)	E	274	22.5	8.21
	$E1$	219	25.9	11.8
	$E2$	54.8	13.1	23.8

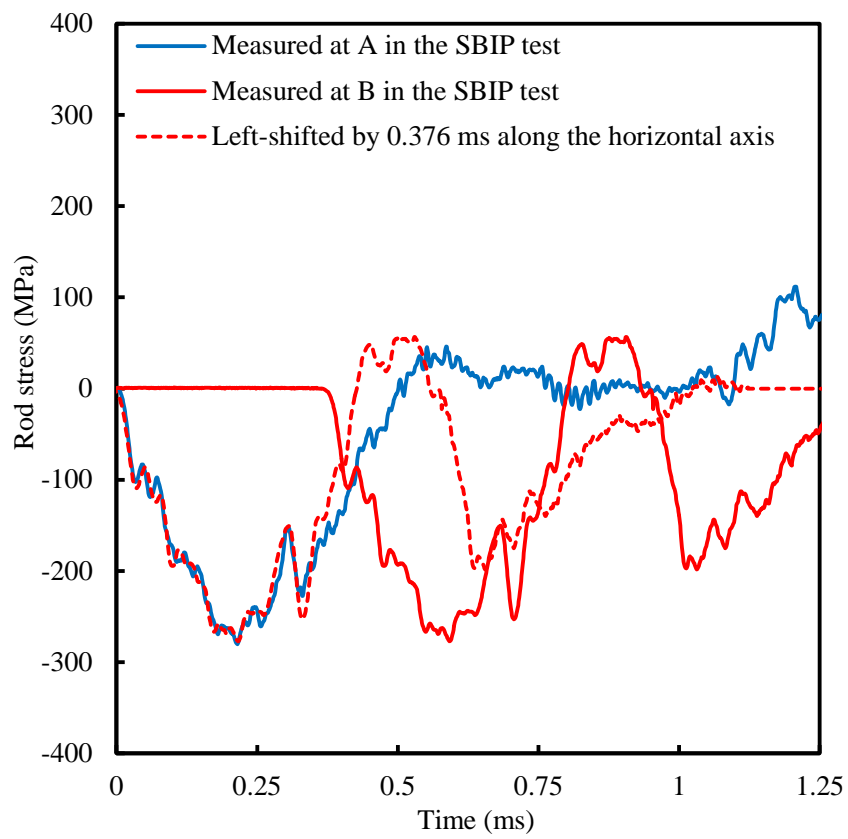
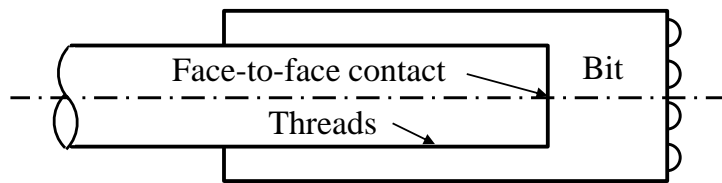
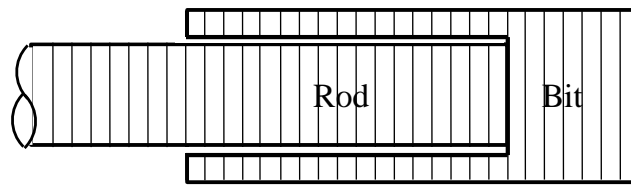


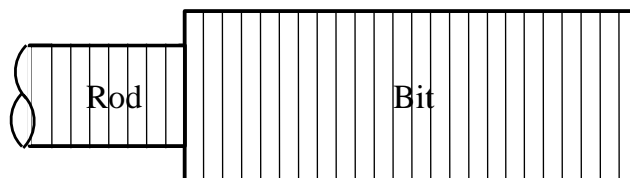
Fig. 4.1 Rod stresses measured at *A* and *B* in the SBIP test.



(a)

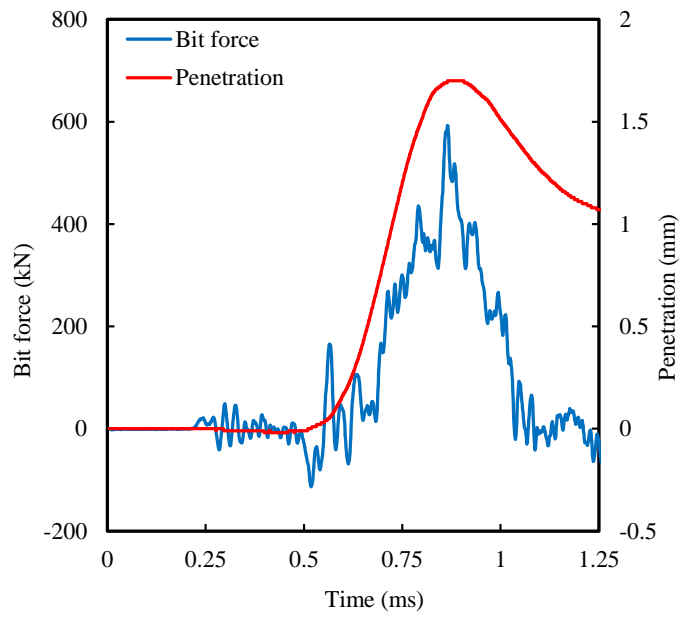


(b)

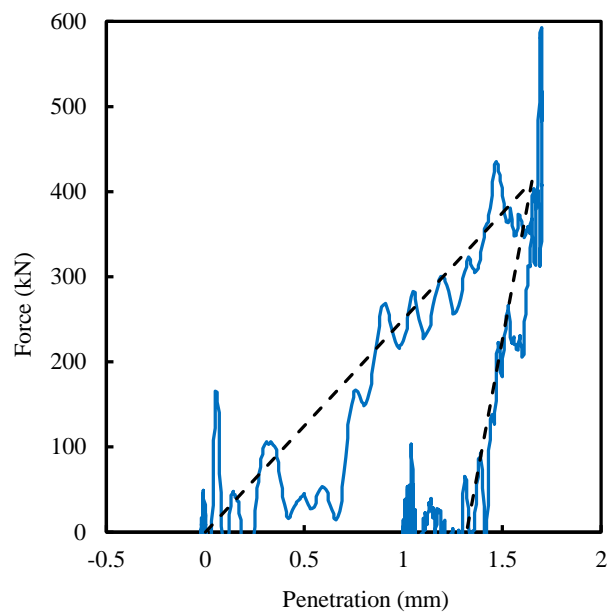


(c)

Fig. 4.2 Schematic illustration and calculation models of a rod and bit. (a) Schematic illustration. (b) Threaded bit model. (c) Unified bit model.



(a)



(b)

Fig. 4.3 Bit force and penetration calculated with the TPSM method. Unified bit model and the rod stresses measured at *A* and *B* in the SBIP test shown in Fig. 4.1 were used in the calculation. (a) Temporal change of the bit force and penetration. (b) Force-penetration curves. The broken black curve was used in the simulation of the rod stress at *B* in Section 4.3.

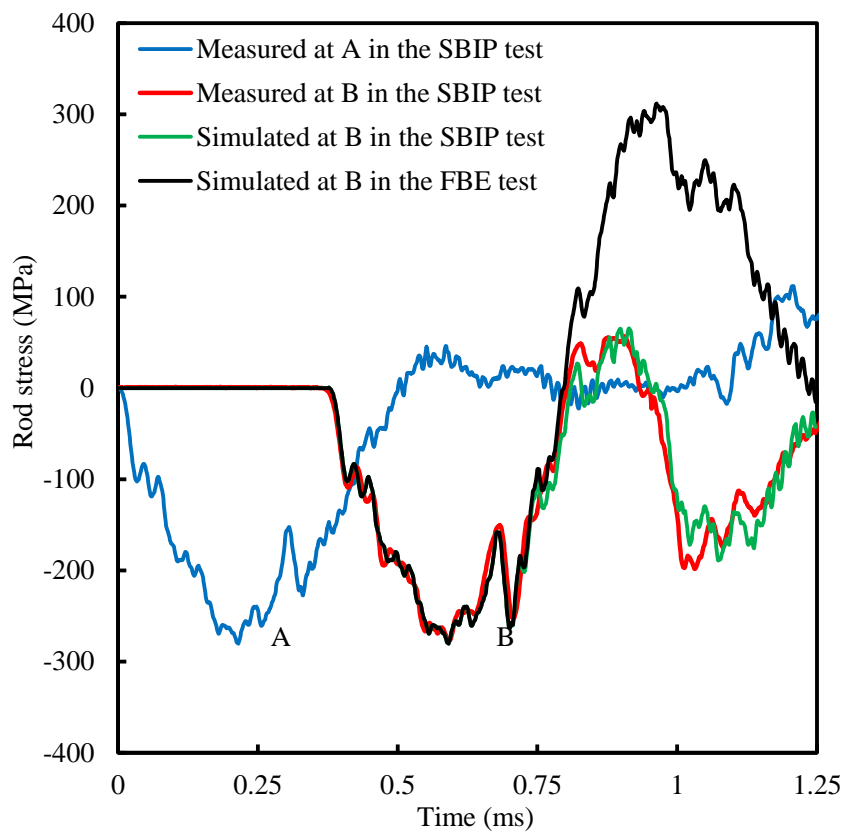
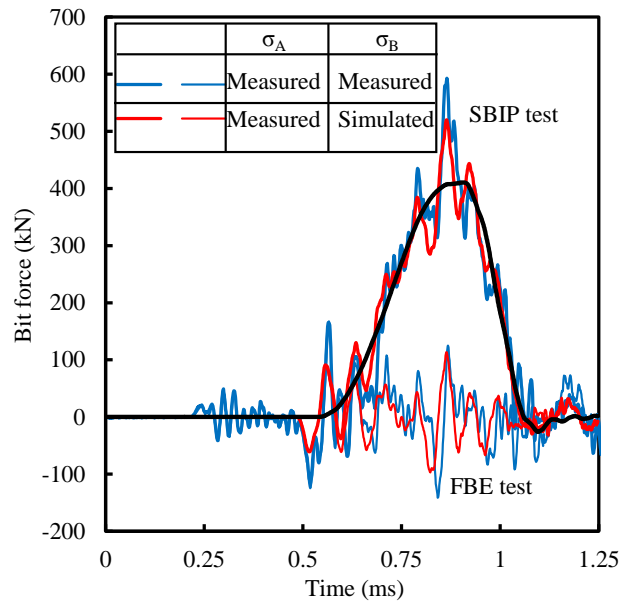
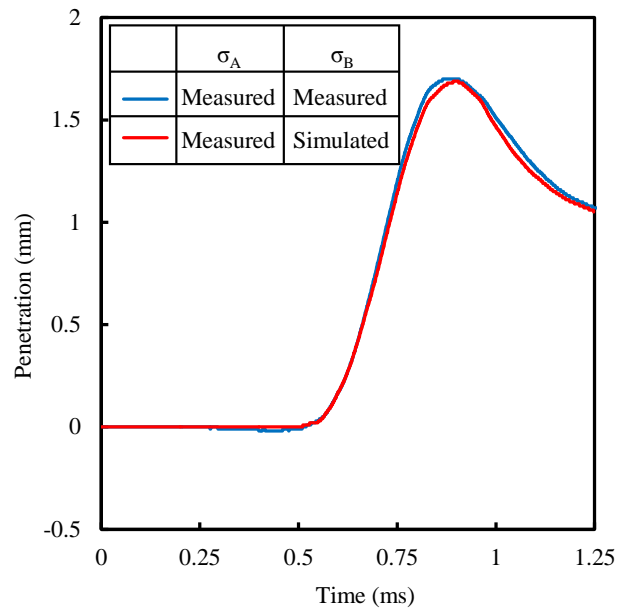


Fig. 4.4 Rod stresses at *A* and *B* in the experiment and simulation. The force-penetration curve shown with a broken black curve in Fig. 4.3 (b) was assumed in the simulation of the rod stress at *B* in the SBIP test.



(a)



(b)

Fig. 4.5 Bit forces and penetrations calculated with the TPSM method. Unified bit model and the rod stresses at A and B in the table were used in the calculation. (a) Bit force in the SBIP and FBE tests. The thick blue curve is the same as the blue curve in Fig. 4.3 (a). The black curve indicates the difference between the thick and thin red curves. (b) Penetration in the SBIP test. The color of the curves corresponds to that of the curves in (a). The blue curve is the same as the red curve in Fig. 4.3 (a).

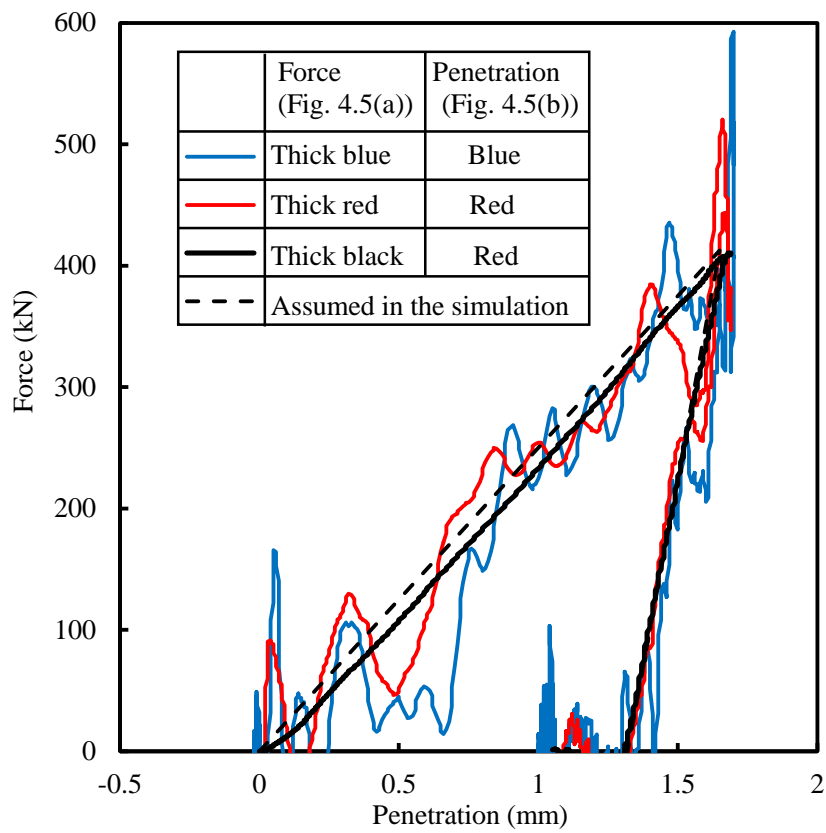


Fig. 4.6 Force-penetration curves obtained from Fig. 4.5. The solid blue and broken black curves are the same ones in Fig. 4.3 (b).

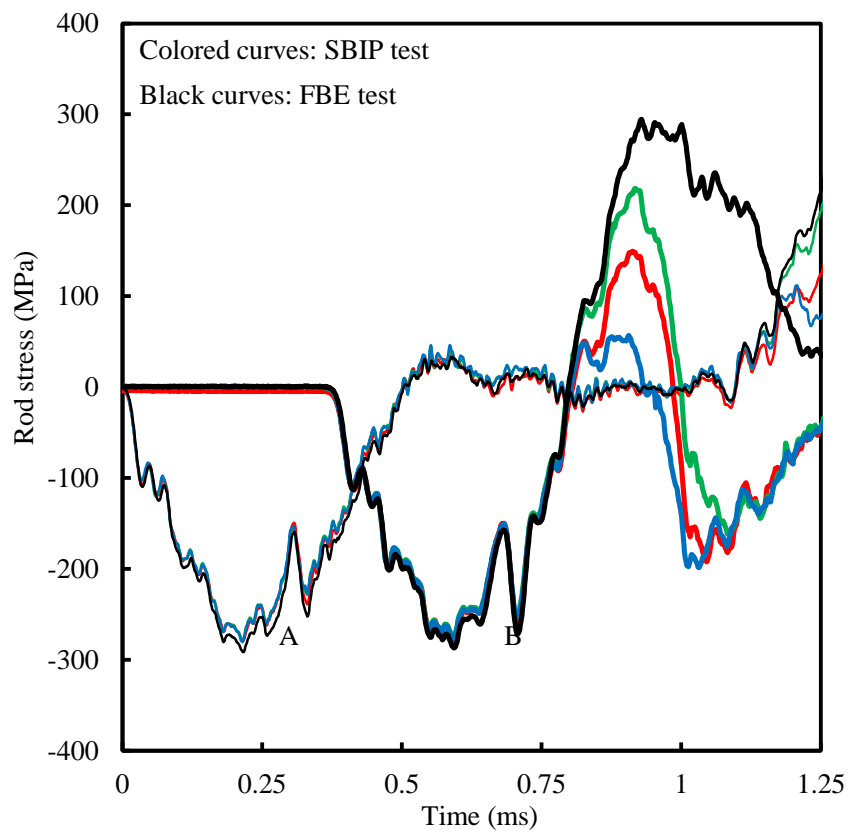
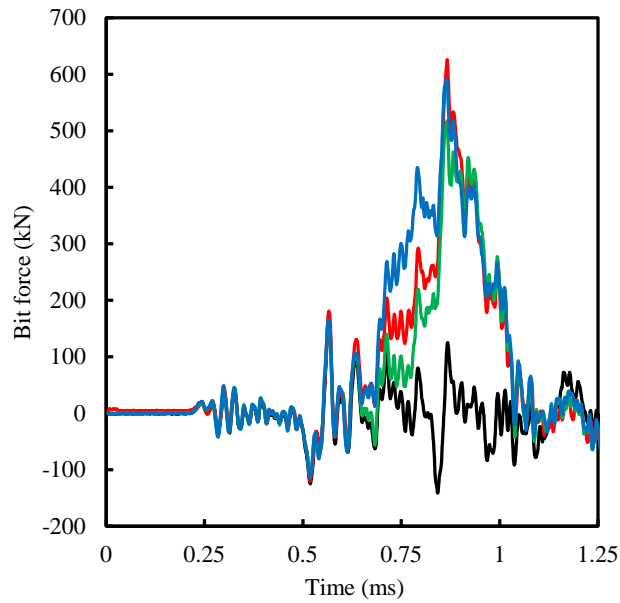
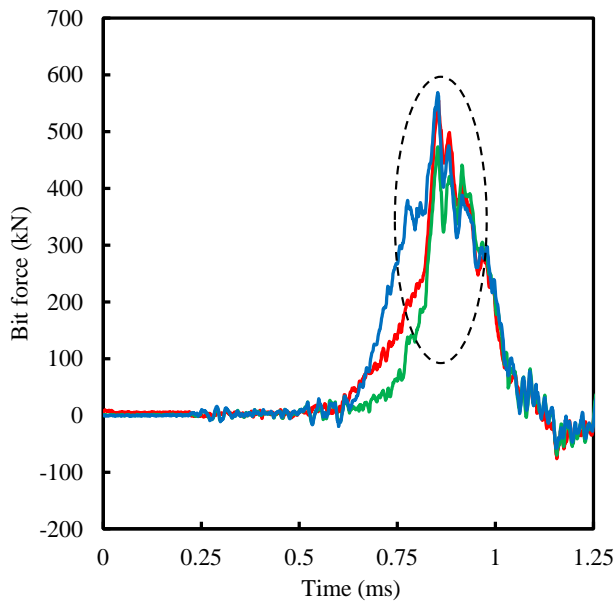


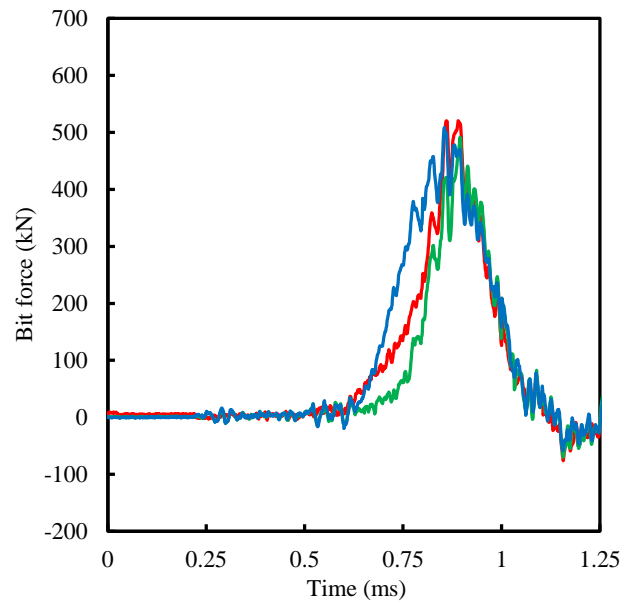
Fig. 4.7 Rod stresses measured at *A* and *B* in three SBIP and an FBE tests. The rod stresses at *A* and *B* are shown with thin and thick curves, respectively.



(a)



(b)



(c)

Fig. 4.8 Bit force calculated with the TPSM method. The color of the curves corresponds to that of the curves in Fig. 4.7. (a) Calculated results with unified bit model. The colored and black curves indicate the results in three SBIP and an FBE tests, respectively. (b) Results after correction. The curves in this figure indicate the difference between the bit forces shown with colored and black curves in Fig.4.8 (a). (c) Results after additional correction. Before 0.8 ms and after 1.0 ms, the curves in this figure are the same as those in Fig.4.8 (b). Between 0.8 and 1.0 ms, the curves in this figure indicate the difference between the bit forces shown with colored curves in Fig.4.8 (a) and a thin red curve in Fig. 4.5 (a).

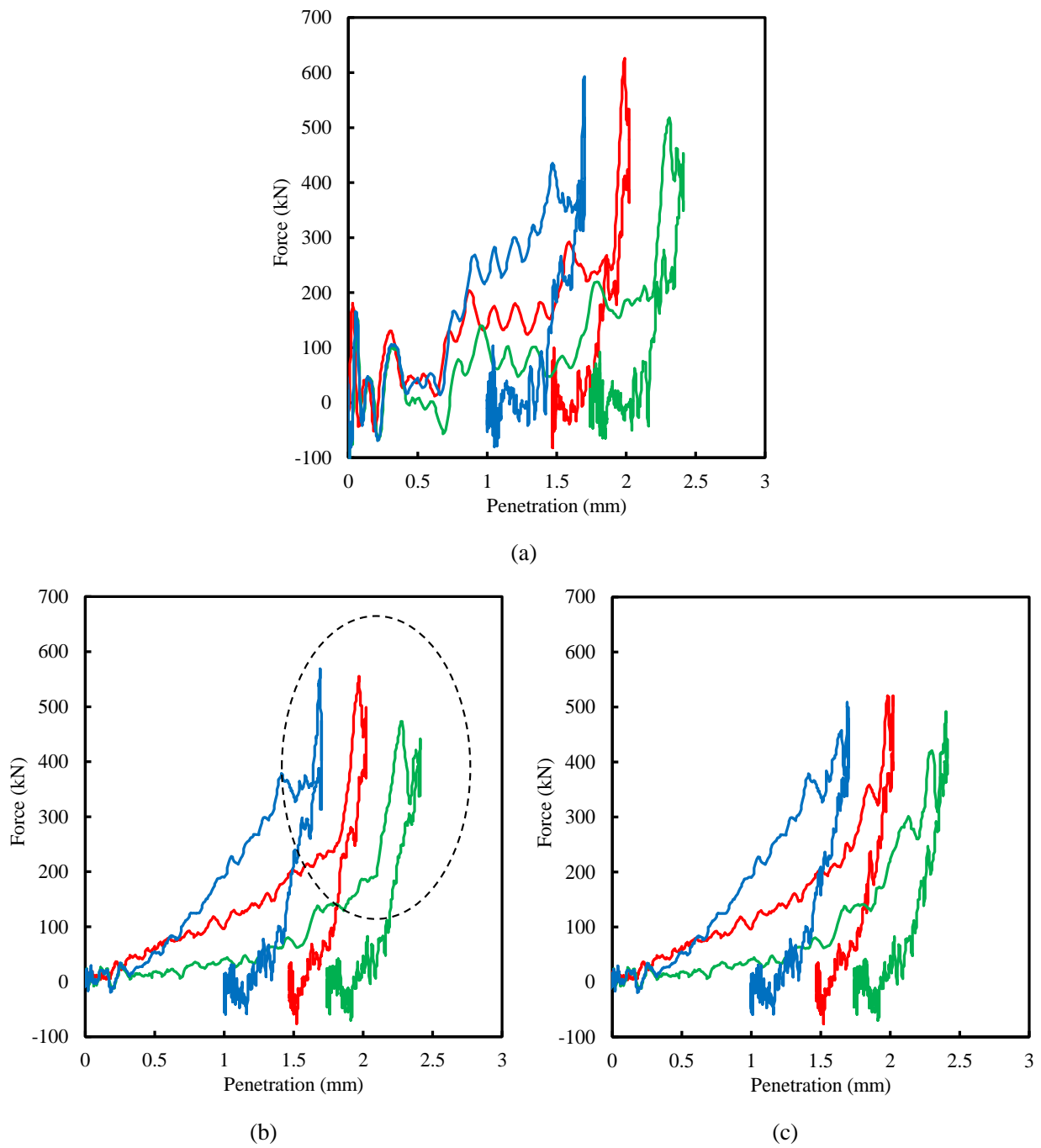


Fig. 4.9 Force-penetration curves calculated with the TPSM method. The color of the curves corresponds to that of the curves in Figs. 4.7 and 4.8. (a) Calculated results with unified bit model. The bit forces are shown with colored curves in Fig. 4.8 (a). (b) Results after correction. The bit forces are shown in Fig. 4.8 (b). (c) Results after additional correction. The bit forces are shown in Fig. 4.8 (c).

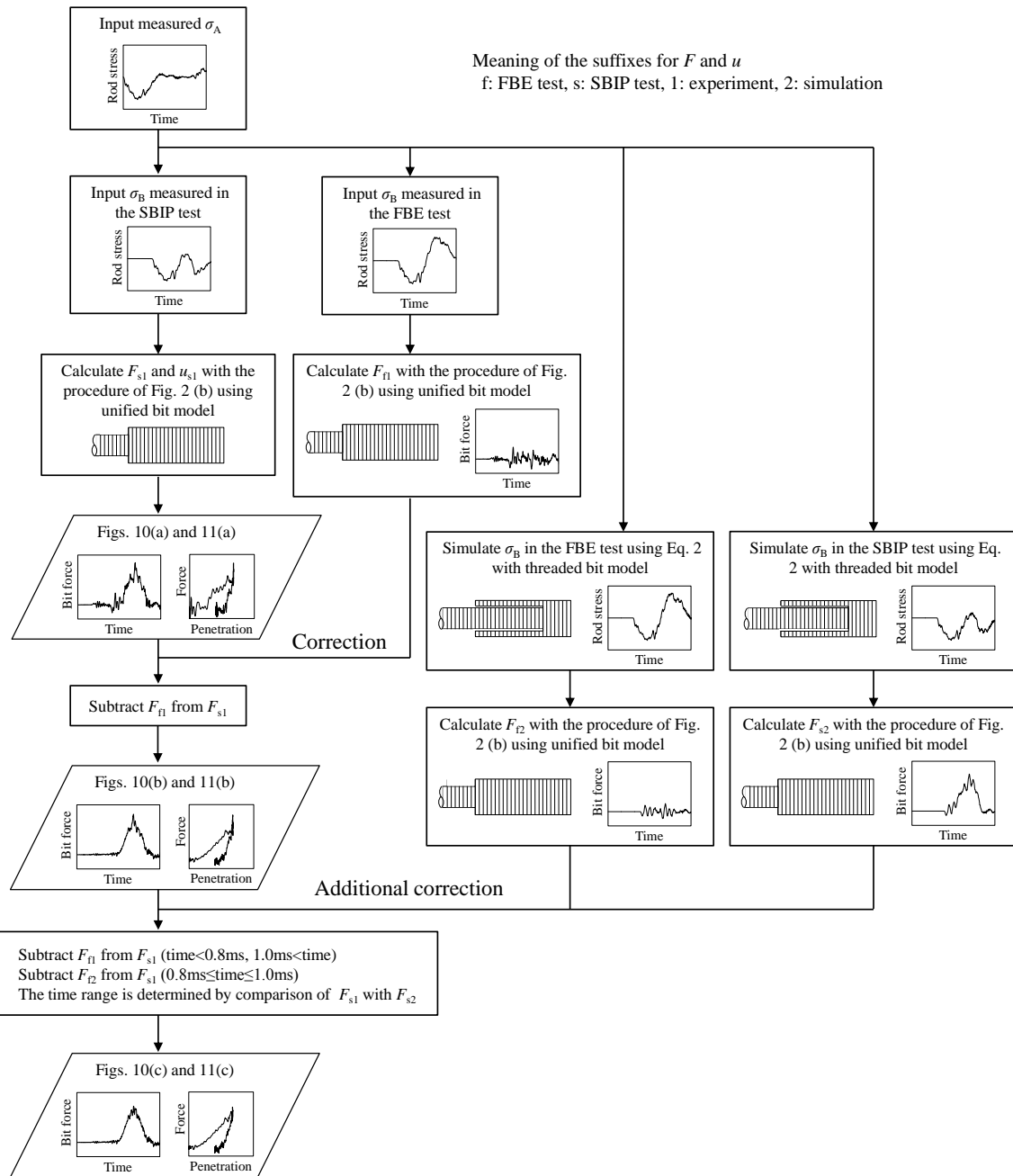


Fig. 4.10 Procedure of the correction method for a force-penetration curve.

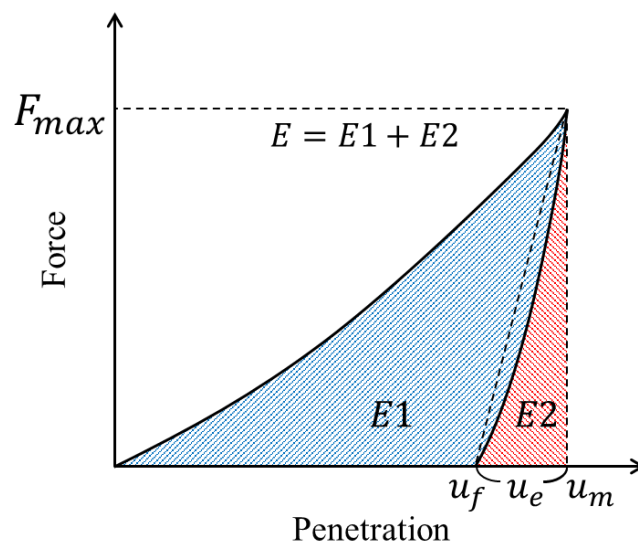
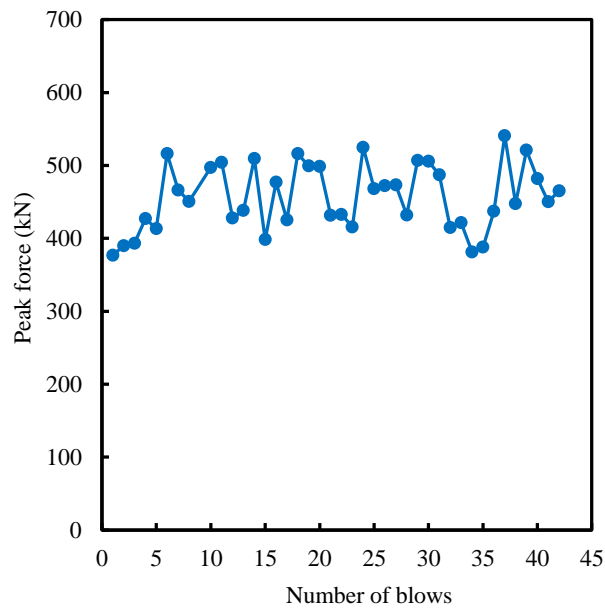
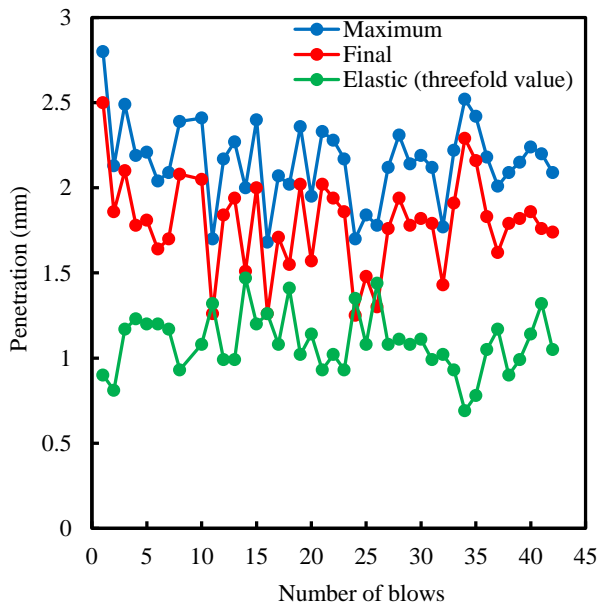


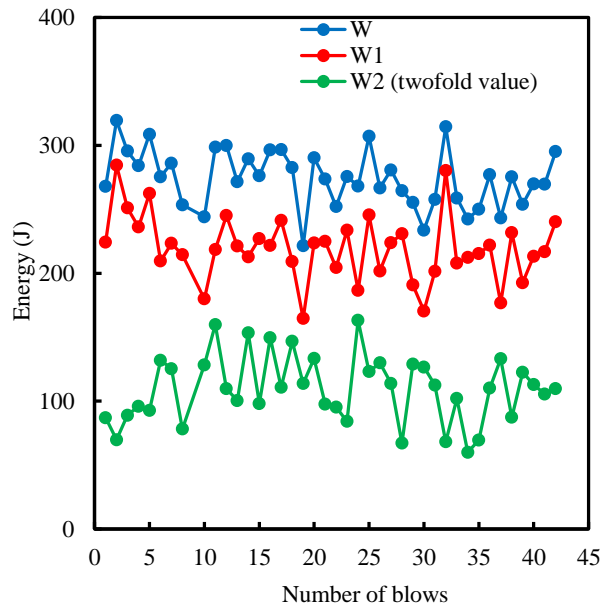
Fig. 4.11 Schematic illustration of a force-penetration curve. F_{max} is peak force. u_m , u_f and u_e are maximum, final and elastic penetrations, respectively. $E1$, $E2$ and E are energies calculated from the shaded areas.



(a)



(b)



(c)

Fig. 4.12 Data obtained from the force-penetration curves for each blow in the SBIP tests. (a) Peak force. (b) Maximum, final and elastic penetrations. (c) Three types of energies, E_1 , E_2 and E .

Chapter 5 Effect of bit configuration in impact penetration tests with button bits

5.1 Introduction

As previously mentioned in Chapter 2, the basic mechanism of rock fragmentation under percussive drilling is indentation loading during repeated impacts which results in the penetration forces needed for the rock failure. The magnitude of the forces affects the drilling performance and is governed by the geometry of the inserts or cutters on the drill bit (Ajibose 2015). A thorough understanding of the bit-rock interaction is of considerable importance in improving hydraulic rock drills, especially in drill bit design.

Research conducted by Lundberg (1973a, b), Paul and Sikarskie (1965), Li and Gu (1994), Karlsson et al. (1989) and Goldsmith and Wu (1981) on rocks showed that the relationship between the bit force F and the penetration u of the indenter was represented as Fig. 5.1. The relationship was approximated for the loading and unloading phase as:

$$F_{rock} = \begin{cases} Ku & \text{for loading} \\ F_{max} - \gamma K(u_{max} - u) & \text{for unloading} \end{cases} \quad (5.1)$$

where K is the penetration resistance produced by penetrating or indenting rock per unit depth and γ is the unloading rate constant.

In this chapter, the impact penetration behavior of button bits into rock was investigated for building the bit-rock interaction model. Impact penetration tests on Inada granite were carried out with six rod-bit configurations which were composed of four types of button bits and two types of rods. In the calculation of force-penetration curves from the measured rod strains, the bit model constructed from the acoustic impedance was simplified, and the empirical data correction method proposed in Chapter 4 was applied.

In Chapter 4, the empirical data correction method was successfully applied for improving the force-penetration curves derived from the SBIP tests with the rod-bit configuration of T38-64 (with the bit diameter of 64 mm). In this chapter, to evaluate the applicability of the method, it is further extended to be used to calculate force-penetration curves derived from the SBIP tests with other rod-bit configurations. Based on the

obtained accurate force-penetration curves for all rod-bit configurations, the effects of shape of rod and bit (e.g., rod diameter, bit diameter) on the impact penetration behavior of button bits are discussed.

5.2 Impact penetration tests with various rod-bit configurations

The impact penetration tester, the experimental procedure and method of impact penetration tests were already described in Chapter 2. In this chapter, the SBIP tests were conducted, not only with the rod-bit configuration of T38-64, but also with other rod-bit configurations. Two types of rods and four types of button bits were used to constitute six rod-bit configurations. The internal and external diameters of the thin rod were 39 mm and 14.3 mm, respectively. Those of the thick rod were 46.2 mm and 15.8 mm. Both the thin and the thick rods were 3,660 mm in length. The thin rod can be connected to the button bits with the diameters of 64 mm, 76 mm, and 89 mm through T38 threads. The thick rod can be connected to the button bits with the diameters of 76 mm, 89 mm, and 102 mm through T45 threads. Table 5.1 lists all rod-bit configurations used in the impact penetration tests. In the table, T38-76 means the thin rod with the T38 threads connected to the button bit with the diameter of 76 mm. The bit shown in Fig. 5.2 has four face tips with the diameter of 11 mm and 8 gauges tips with the diameter of 12 mm.

5.3 Simplified modeling method for button bits

In Chapter 4, the two bit models shown in Fig. 5.3 (b) and (c) were used to calculate force-penetration curves from the measured rod strains. It is necessary to construct the acoustic impedance profile for the bit. However, it is difficult to accurately construct the profile corresponding to their geometries due to their complicated geometries, especially at the bit end where the button tips were embedded. A simplified modeling method associated to constructing the acoustic impedance profile for the bit were proposed, and discussed.

In the simplified modeling method, the acoustic impedance for each segment in the bit model were assumed to be a constant, as illustrated in Fig. 5.3 (d), and based on the assumption the constant acoustic impedance can be calculated as follows

$$Z = \frac{AE}{c} = \frac{mc}{l} \quad (5.2)$$

where A is the cross-sectional area, E is the Young's module, and c is the

elastic wave speed. m is the effective mass of the bit model, which includes the bit mass and the mass of the rod end inside the bit. The mass of the rod end inside the bit is calculated by the density, external and internal radiuses of the rod. l is the bit length (excluding the tip length). The effect of not considering the tip length on stress wave propagation is relatively small. In the method, the acoustic impedances of the bit model can be easily constructed only by measuring the length and mass of the bit.

The bit model used for the bit force correction shown in Fig. 5.3 (c) was simplified into the bit model shown in Fig. 5.3 (e). That is, the front portion of the bit model is the same as that shown in Fig. 5.3 (d), but the thread portions of the rod and the bit in the bit model were separated from each other. The validation of the simplified bit models will be discussed in Section 5.4.

5.4 Experimental results

The bit forces and penetrations were calculated by the TPSM method introduced in Section 2.4.5 and then improved by the empirical data correction method proposed in Chapter 4. In Fig. 5.4, the blue solid and red dash curves represent the bit forces and penetrations calculated with the bit models of Fig. 5.3 (b) and (c) as well as with the bit models of Fig. 5.3 (d) and (e), respectively. The experimental results for calculating the bit force and penetration were obtained from the SBIP tests with the rod-bit configuration of T38-64. The time when the measured strain began to increase since stress waves arrived at the point A was set to be the origin. The blue and red curves are almost overlapped with each other. It is shown that there was no significant effect of the simplified modeling method for button bits on the accuracy of calculated results. In the chapter, the bit model shown in Fig. 5.3 (d) was used for calculating the bit force and penetration, and the bit model shown in Fig. 5.3 (e) was used in the data correction method proposed in Chapter 4 for improving force-penetration curves.

In Chapter 4, only experimental data obtained from the SBIP tests with the rod-bit configuration of T38-64 were processed. In the chapter, those from the SBIP tests with all rod-bit configurations listed in Table 5.1 were processed. Fig. 5.5 shows the bit forces and force-penetration curves of the four results in the 48 SBIP tests with the rod-bit configuration of T38-76. As shown in Fig. 5.5 (a), the bit forces begin to increase after stress waves arrived at the bit end and then sharply decrease after the peak. Before the peak, several unnatural abrupt changes in the slope of the force-penetration curves are observed and indicated by black arrows in the

figure. The changes should occur randomly if the changes in the slope are caused by rock chipping. However, the abrupt changes are occurred at the same time. Therefore, it is speculated that the correction was probably insufficient for the force-penetration curves. Nonetheless, as the case of the rod-bit configuration of 38-64 in Chapter 4, the calculation errors in force-penetration curves are also basically eliminated for other rod-bit configurations. The same tendency that the bit forces increase with small changes and approximately linearly decrease with penetration after their peak is found. The force-penetration curves varied with each blows are observed in Fig. 5.5 (b).

In Fig. 5.6, the force-penetration curves from the same rod-bit configuration are shifted left by $u_m - \bar{u}_m$ to make their maximum penetration u_m align to the average maximum penetration \bar{u}_m for studying the tendency of these curves. Although force-penetration curves as shown in Fig. 5.5 (b) vary with each blow, an overall tendency can be observed from Fig. 5.6. In loading phase, the force-penetration curves for all rod-bit configurations are not straight but are concave-upward. In unloading phase, the force-penetration curves decrease linearly after the peak. The force-penetration curves of T45-76 and T45-89 have not shown here, because the force-penetration curves of T45-76 are close to those of T38-76, and the force-penetration curves of T45-89 are close to those of T38-89. Stress wave transmission and reflection characteristics at the rod-bit connection are affected by the rod diameter under the condition of the same bit diameter, but the effect is relatively small.

The master curves corresponding to Eq. (5.3) when $b = 1.5, 2$ and 3 are plotted in Fig. 5.6,

$$F = au^b \quad (5.3)$$

Comparing the portion of force-penetration curves before the peak with the master curves, it is found that the master curve of $b = 1.5$ is close to the upper bound, while that of $b = 3$ is close to the lower bound. The master curves of $b = 2$ is close to the mean value. The a values calculated by fitting curves with Eq. (5.3) when $b = 2$, were listed in Table 1. The a values of T38-64, T38-76 and T45-76 are almost 90 kN/mm^2 , while those of T38-89, T45-89 and T45-102 are almost 160 kN/mm^2 .

Fig. 5.7 shows the relationship between a and b . The values of the two parameters were determined by fitting curves to experimental data with Eq. (5.3). The force-penetration curves from the rod-bit configurations of T38-64, T38-76 and T45-76, with blue colors, all of which have 12 button

tips on the bit, have a similar tendency. Those from the rod-bit configurations of T38-89, T45-89 and T45-102, with red color, all of which have 14 button tips, have a similar tendency. There is a large variation in b and its mean value is about 2. There is a variation in a even when b is fixed. The experimental data points shown in blue colors are basically above those shown in red color.

Fig. 5.8 shows the relation between the maximum penetration u_m and the final penetration u_f . u_f is the penetration when the bit force becomes zero after it reached the peak. Fukui et al. (2010) reported there was a linear relationship between the u_m and the u_f for T38-64. In this study, the linear relationship between the two parameters for other rod-bit configurations was also obtained and expressed as the Eq. (5.4), which was obtained by the least square method (LSM)

$$u_f = 1.1u_m - 0.56 \quad (5.4)$$

Thus, the final penetration for each blow can be read from Fig. 5.5 (b), or estimated by Eq. (5.4). For each rod-bit configuration, the borehole depth $\sum u_b$ is smaller than its cumulative final penetration $\sum u_f$. Because the contact position of the button tips on rock changed per blow with the bit rotation. As shown in Fig. 2.11 (b), the distance of the back end of the bit to the rock surface L was measured before the next blow started. The borehole depths for all rod-bit configurations are shown in Fig. 5.9. The horizontal axis represents the cumulative angular rotation of the bit during the SBIP tests. It can be seen that the borehole depths linearly increases with the increase of rotation degree. The borehole depths for different rod-bit configurations are almost the same to each other, except that for the rod-bit configuration of T45-102. The borehole depth for T45-102 is smaller than those for the other rod-bit configurations, which is because there was obvious difference in impact velocity of piston (impact energy) between T45-102 and other rod-bit configurations. The variation in the borehole depths reflected the difference.

Fig. 5.10 shows the relationship between the maximum penetration u_m and the change u_b in the borehole depth with each blow in order to eliminate the effect of the variation in impact energy with blows. The data points are the means for each rod-bit configuration. In addition, data obtained from consecutive percussive drilling with a worn button bit (Fukui et al. 2008) are also shown in the figure. The relationship between the two parameters in this study is on the extension line of Fukui et al. (2008), which is expressed as follows

$$u_b = 0.26u_m \quad (5.5)$$

Meanwhile, the slight difference in the relationship between this study and Fukui et al. (2008) was found, and that was because the used button bits, experimental methods and so on were different with each other. In Fukui et al. (2008) the used button bit was a worn bit while in this study that was a new one. The SBIP tests were conducted in this study while consecutive penetration drilling was conducted in Fukui et al. (2008).

The specific energies (SE) for all rod-bit configurations were calculated and listed in Table 5.1. The specific energy, defined as the energy required to excavate a unit volume of rock, is well-known to be effective for the estimation of the efficiency of an excavation method (Teale 1965). The volume is equal to the bit diameter multiplied by the borehole depth. The energy per blow is the area surrounded by the force-penetration curve in Fig. 5.5. The total energy is the cumulative energy per blow. As listed in Table 5.1, the SEs for T38-64, T38-76 and T45-76 are almost 100 MPa while those for T38-89, T45-89 and T45-102 are almost 80 MPa.

5.5 Discussion

Fig. 5.6 shows the bit force in loading phase, the portion from the origin to the peak, is approximately proportional to the square of the penetration even though there are small changes in each force-penetration curve and variation in force-penetration curve with each blow in the SBIP tests. In the case of the contact of a sphere on a half-space, the exponent of the power relationship between the bit force and the penetration is equal to 1.5 based on the Hertzian contact theory for elastic deformation, and is equal to 1 for plastic deformation. The obtained experimental result from impact penetration tests with a button tip on granite is very close to the theoretical value. Okubo et al. (1992) obtained a linear relationship between the bit force and the penetration from both dynamic and static penetration tests. Ajibose et al. (2015) found a power relationship between the bit force and the penetration with an exponent of 1.45 ± 0.05 . However, the aforementioned experimental results were obtained from the penetration tests with a button tip. In the case of the impact penetration tests with button bits which have many button tips, the number of button tips contacting with the rock surface increases with the increase of the penetration. Fig. 5.11 shows the schematic illustration of an extreme case. The thin lines represent the force-penetration curves in loading phase of each tip. The linear relationship between the tip force and the penetration is adopted based on Okubo et al. (1992). It is assumed that the tips contact with the rock surface in order whenever the penetration increases by a

fixed amount. The bold line is the force-penetration curve of a button bit which is the sum of the thin lines, and consequently the bit force in loading phase is approximately proportional to the square of the penetration, which explains the trend of the force-penetration curves shown in Fig. 5.6. If most of the button tips on the bit end initially contact on rock surface, the exponent of the power law is close to 1. In contrast, if the interval after the next tip contacting on the rock surface becomes large, the exponent of the power law will be probably large than 2. The variation in b with blows shown in Fig. 5.7 illustrates the contact condition of tips on rock surface varied with each blow.

Next, let us consider the variation of a when b is fixed. As mentioned in Section 5.4, it is observed that the more the button tips on the bit, the larger a is from comparison of the experimental results of T38-64, T38-76 and T45-76, which have 12 tips, to those of T38-89, T45-89 and T45-102, which have 14 tips. The larger the tip diameter is, the larger the slope of force-penetration curve (thin line in Fig. 5.11) of a tip is, which is another important reason why a of T38-89, T45-89 and T45-102 were larger than those of T38-64, T38-76 and T45-76. In addition, the smaller the interval between the thin curves, that is, the smaller irregularity in the bottom of the borehole is, the larger a is. The effect of the number of tips on the value of a is observed from the experimental results. The factor related to contact condition of tips on rock surface will be added into numerical simulation of percussive drilling with data accumulation in future work. The three-dimensional shape of bottom of the borehole will be measured.

Okubo et al. (1995) observed changes in the loading phase of force-penetration curves in quasi-static penetration tests with a button bit on Inada granite and speculated that the changes were caused by rock chipping. The changes resulted in a 60 percent decline in bit force when the peak was almost 100 kN. On the other hand, abrupt changes illustrated in Fig. 5.5 with the black arrows are not caused by rock chipping, but are caused by calculation error. The calculation error could not be corrected by the data correction method proposed in Chapter 4. Besides the abrupt changes caused by calculation error, changes of dozens of kN in the loading phase of force-penetration curves are also observed in the force-penetration curves of impact penetration tests. The amplitude of the changes is smaller than the peak, but are the same level of the changes observed in the quasi-static penetration tests. It is difficult to distinguish between the changes caused by rock chipping and the changes caused by calculation error. In quasi-static penetration test, the rock chipping can be captured by naked eye. However, in impact penetration test, it is necessary to use high-speed camera for capturing the rock chipping.

Fukui and Okubo (1994) showed there existed a good correlation between the non-dimensional specific energy (SE) and the particle size distribution. The non-dimensional specific energy is the ratio of specific energy to uniaxial compression strength. The non-dimensional SEs for T38-64, T38-76 and T45-76 are about 0.68 while those for T38-89, T45-89 and T45-102 are about 0.54. A slight difference between them is observed. In future studies, the particle size distribution of detritus generated from the impact penetration tests with button bits will be discussed.

These findings will contribute to improving the simulation of consecutive percussive drilling, which will be later discussed in Chapter 6. In previous studies (Lundberg et al. 1982, 1985, 1986, 1987; Okubo et al. 1991, 1997; Simon 1964; Hustrulid et al. 1971a, 1971b, 1972a, 1972b), the force-penetration curve was simplified to the bilinear model as shown in Fig. 5.1 because accurate force-penetration curve for impact penetration tests with button bits was not obtained. Based on the accurate force-penetration curves obtained in this study, the relation between the bit force and the penetration in loading phase is changed from the linear relation to the power relation with an exponent of 2. The relation between the bit force and the penetration in unloading phase still remains the linear relationship. The final penetration can be estimated by Eq. (5.4). The change in the borehole depth can be estimated by Eq. (5.5), which is close to the assumption ($u_b = 0.3u_m$) made in Okubo and Nishimatsu (1991). The aforementioned assumptions associated to the penetrations and the changes in the borehole depth with each blow are constant, so a simulation considering the variations will be necessary in future work. The change in force-penetration curve with each blow can be reproduced by varying a and b in Eq. (5.3) as in Fig. 5.7. In addition, as shown in Fig. 5.9, the change in the borehole depth is not a constant, it varied with each blow. It is necessary to conduct simulation of consecutive percussive drilling with consideration of the change in the borehole depth in future work.

5.6 Conclusions

In this chapter, impact penetration tests on Inada granite were carried out with six rod-bit configurations which were composed of four types of button bits and two types of rods. The bit model constructed from the acoustic impedance was simplified and the empirical data correction method proposed in Chapter 4 was applied to calculate force-penetration curves of all the rod-bit configurations.

The force-penetration curves for the six rod-bit configurations showed that

the bit force in loading phase was approximately proportional to the square of the penetration. However, the exponents of the power relationship between the bit force and the penetration was affected by the tips-rock contact condition. The curves in unloading phase had a linear relationship between the bit force and the penetration. The final penetration for each blow had a linear relation with the maximum penetration. The borehole depth was also proportional to the maximum penetration.

The effect of rod diameter on the force-penetration curve was not obviously observed under the condition of the same bit diameter. In practice, increasing the rod diameter will increase the cost, but the problems related to the durability, bending and flushing will be improved. For increasing the bit diameter or the number of button tips on the bit, the bit force per unit penetration increased while the specific energy decreased. However, the effect of number of tips on force-penetration curves has not quantitatively discussed. The effect of face and gauge tips on the force-penetration curve is also an unsolved issue.

In Chapter 6, the new bit-rock interaction model will replace the bit-rock interaction model of the Okubo-Nishimatsu's model. The variation in the contact status between the bit and the rock during consecutive percussive drilling will also be considered in numerical simulation.

References

Ajibose O. K., Wiercigroch M., Akisanya A. R. (2015): Experimental studies of the resultant contact forces in drillbit–rock interaction, *Int. J. Mech. Sci.*, vol. 91, pp. 3-11.

Carlsson J., Sundin K. G. and Lundberg B. (1990): A method for determination of in-hole dynamic force-penetration data from two-point strain measurement on a percussive drill rod, *Int. J. Rock Mech. Min. Sci.*, vol. 27, pp. 553-558.

Fukui K., Okubo S. (2004): Estimation of size effects in rock strength based on specific energy, *J. of MMIJ*, vol. 120, pp. 555-559 (in Japanese).

Fukui, K., Abe, H., Koizumi, M., Tomosada, H., Okubo, S. (2007): Attenuation of Rod Stress in Percussive Long-hole Drilling, *J. of MMIJ*, vol. 123, pp. 152-157 (in Japanese).

Fukui K., Abe H., Koizumi M., Tomosada H. and Okubo S. (2008): Force-penetration curves with a worn button bit in the percussive long-hole drilling, *J. of MMIJ*, vol. 124, pp. 785-793 (in Japanese).

Fukui K., Okubo S., Koizumi M., Shioda A., Matsuda T. and Fukuda S. (2010): Force-penetration curves with a button bit in the percussive drilling, *J. of MMIJ*, vol. 126, pp. 512-518 (in Japanese).

Goldsmith W., Wu W. Z. (1981): Response of rocks to impact loading by bars with pointed ends, *Rock Mech.* vol. 13, pp. 157-184.

Hustrulid W. A., Fairhurst C. (1971): A theoretical and experimental study of the percussive drilling of rock part I - theory of percussive drilling, *Int. J. of Rock Mech. Min. Sci.*, vol. 8, pp. 311-333.

Hustrulid W. A., Fairhurst C. (1971): A theoretical and experimental study of the percussive drilling of rock part II - force-penetration and specific energy determinations, *Int. J. of Rock Mech. Min. Sci.*, vol. 8, pp. 335-356.

Hustrulid W. A., Fairhurst C. (1972): A theoretical and experimental study of the percussive drilling of rock part III - experimental verification of the mathematical theory, *Int. J. of Rock Mech. Min. Sci.*, vol. 9, pp. 417-429.

Hustrulid W. A., Fairhurst C. (1972): A theoretical and experimental study of the percussive drilling of rock part IV - application of the model to

actual percussion drilling, *Int. J. of Rock Mech. Min. Sci.*, vol. 9, pp. 431-449.

Japanese society of tribologists (2001): *Tribology handbook*, Yokendo Ltd., Tokyo, pp. 10-15 (in Japanese).

Karlsson L. G., B. Lundberg B. and Sundin K. G. (1989): Experimental study of a percussive process for rock fragmentation, *Int. J. Rock Mech. Min. Sci. & Geomech. Abstr.*, vol. 26, pp. 45-50.

Lundberg B. (1973): Energy transfer in percussive rock destruction I – comparison of percussive methods, *Int. J. Rock Mech. Min. Sci. & Geomech. Abstr.*, vol. 10, pp. 381-399.

Lundberg B. (1973): Energy transfer in percussive rock destruction II – supplement on hammer drilling, *Int. J. Rock Mech. Min. Sci. & Geomech. Abstr.*, vol. 10, pp. 401-419.

Lundberg B., Henchoz A. (1977): Analysis of elastic waves from two-point strain measurement, *Experimental Mechanics*, vol. 17, pp. 213-218.

Lundberg B. (1982): Microcomputer simulation of stress wave energy transfer to rock in percussive drilling, *Int. J. Rock Mech. Min. Sci. & Geomech. Abstr.*, vol. 19, pp. 229-239.

Lundberg B. (1985): Microcomputer simulation of percussive drilling, *Int. J. Rock Mech. Min. Sci. & Geomech. Abstr.*, vol. 22, pp. 237-249.

Lundberg B. and Karlsson L. G. (1986): Influence of geometrical design on the efficiency of a simple down-the-hole percussive drill, *Int. J. Rock Mech. Min. Sci. & Geomech. Abstr.*, vol. 23, pp. 281-287.

Lundberg B. (1987): Efficiency of percussive drilling with extension rods, *Int. J. Rock Mech. Min. Sci. & Geomech. Abstr.*, vol. 24, pp. 213-222.

Okubo S. and Nishimatsu Y. (1991): Computer simulation of percussive drilling, *J. of MMIJ*, vol. 107, pp. 209-214 (in Japanese).

Okubo S., Nishimatsu Y., Akiyama M. and Tatsumi T. (1992): Study on impact penetration test of rock, *J. of MMIJ*, vol. 108, pp. 134-140 (in Japanese).

Okubo S., Ota A., Akiyama M. and Fukui K. (1995): Static penetration test

with a button bit, Proceedings of the fall meeting of MMIJ, pp. 174 (in Japanese).

Okubo S. (1997): Effects of thrust on rock-drill performance—computer simulation of percussive drilling (2nd report), J. of MMIJ, vol. 113, pp. 613-618.

Okubo S. and K. Fukui K. (2000): Numerical simulation of drilling with button bit, J. of MMIJ, vol. 116, pp. 988-993.

Simon R. (1964): Transfer of the stress wave energy in the drill steel of a percussive drill to the rock, Int. J. of Rock Mech. Min. Sci., vol. 1, pp. 397-411.

Teale R. (1965): The concept of specific energy in rock drilling, Int. J. Rock Mech. Min. Sci., vol. 2, pp. 57-73.

Table 5.1 Conditions and results of the impact penetration tests.

Configuration	Rod		Bit		Test condition			Test result	
	Extremal diameter (mm), internal diameter (mm), and threads type	Diameter (mm)	Face tip number – diameter (mm)	Gauge tip number – diameter (mm)	Bit rotation per blow (°)	Number of blows	a (kN/mm ²) in Eq. (7) when $b=2$	Specific energy (MPa)	
T38-64	φ39.0, φ14.3 and T38	64	4-φ10	8-φ11	25.7	43	93.4	101	
T38-76	φ39.0, φ14.3 and T38	76	4-φ11	8-φ12	22.5	48	81.8	108	
T45-76	φ46.2, φ15.8 and T45						98.7	102	
T38-89	φ39.0, φ14.3 and T38	89	6-φ12	8-φ14	20	54	174.2	73	
T45-89	φ46.2, φ15.8 and T45						161.7	80	
T45-102	φ46.2, φ15.8 and T45	102	6-φ12	8-φ14	18	60	143.9	80	

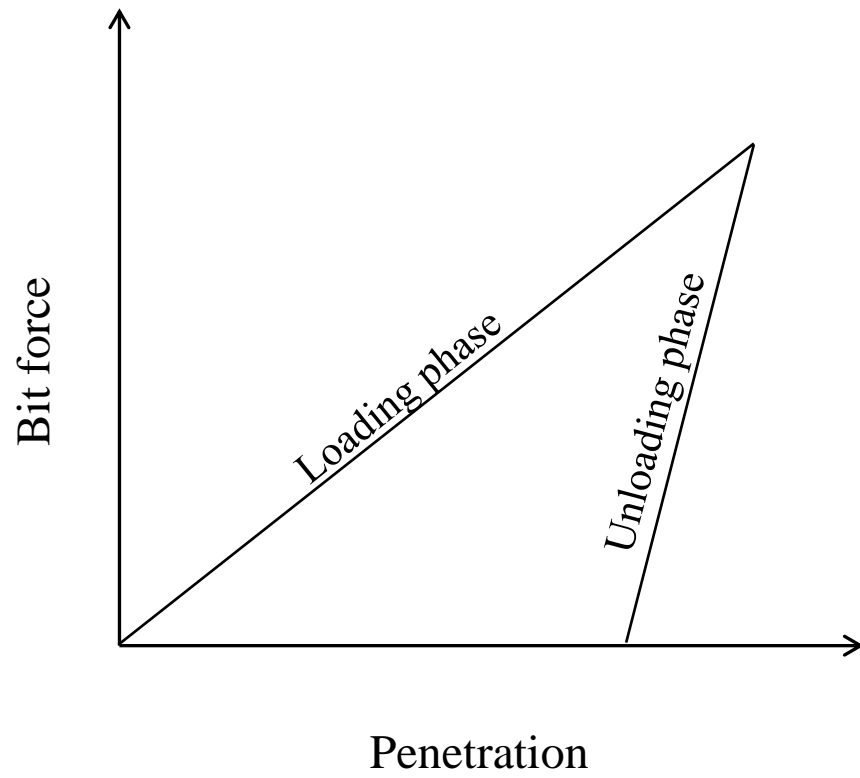


Fig. 5.1 Force-penetration curve assumed in previous numerical simulations.

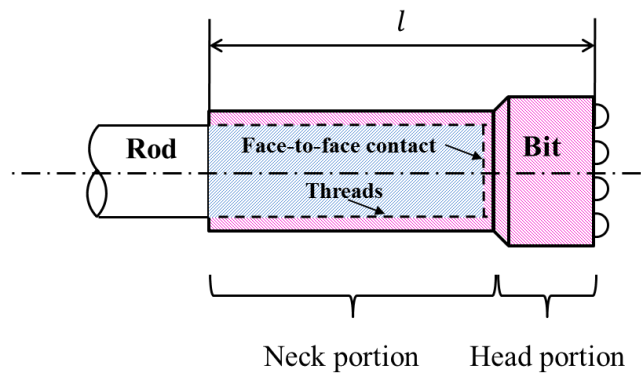


(a) Front view

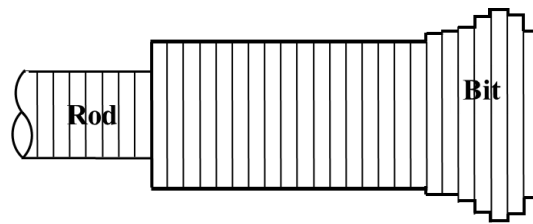


(b) Behind view

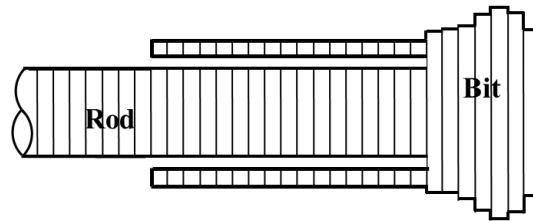
Fig. 5.2 Photographs of the button bit used in the rod-bit configuration of T38-76.



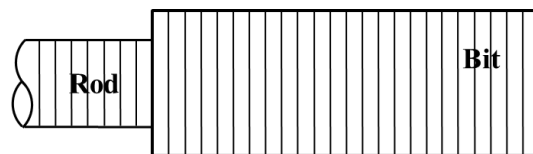
(a)



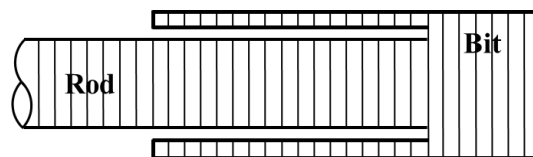
(b)



(c)



(d)



(e)

Fig. 5.3 Schematic illustration of a rod and bit, as well as its numerical models for calculating force-penetration curves. (a) Schematic illustration. (b) Original bit model. (c) Original slit bit model. (d) Simplified bit model. (e) Simplified slit bit model.

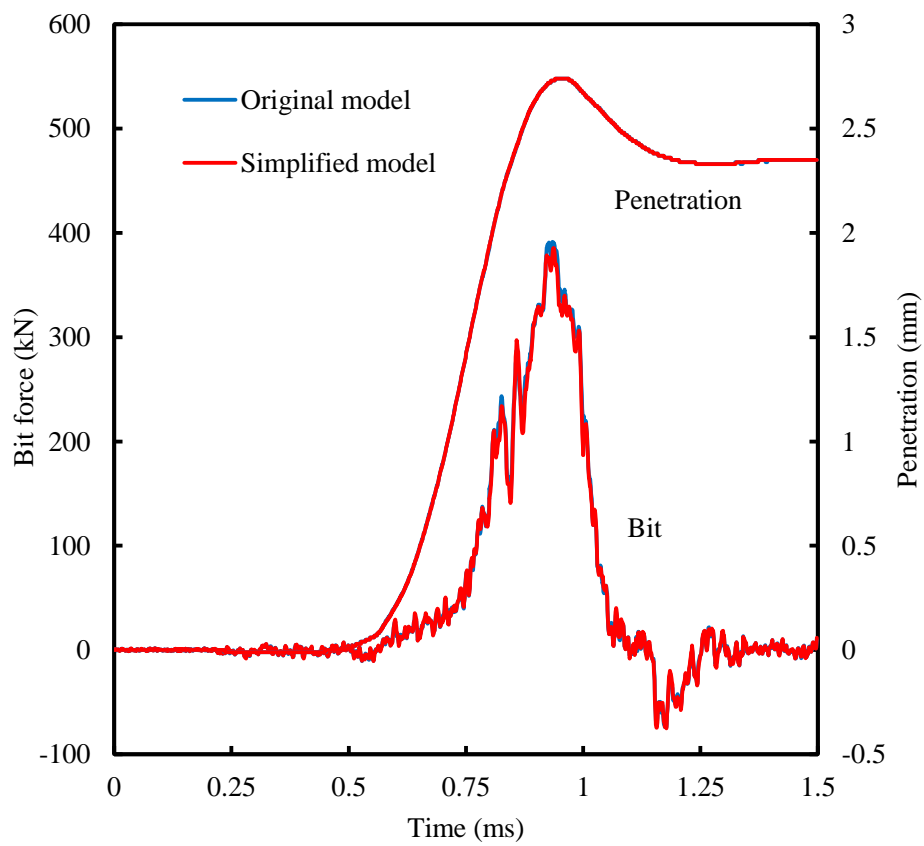
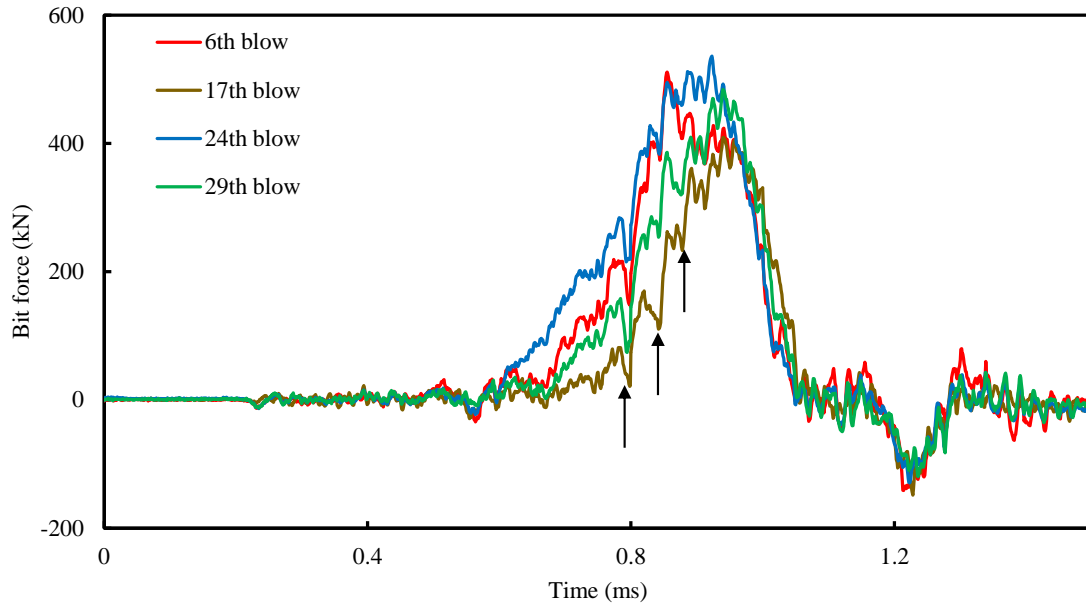
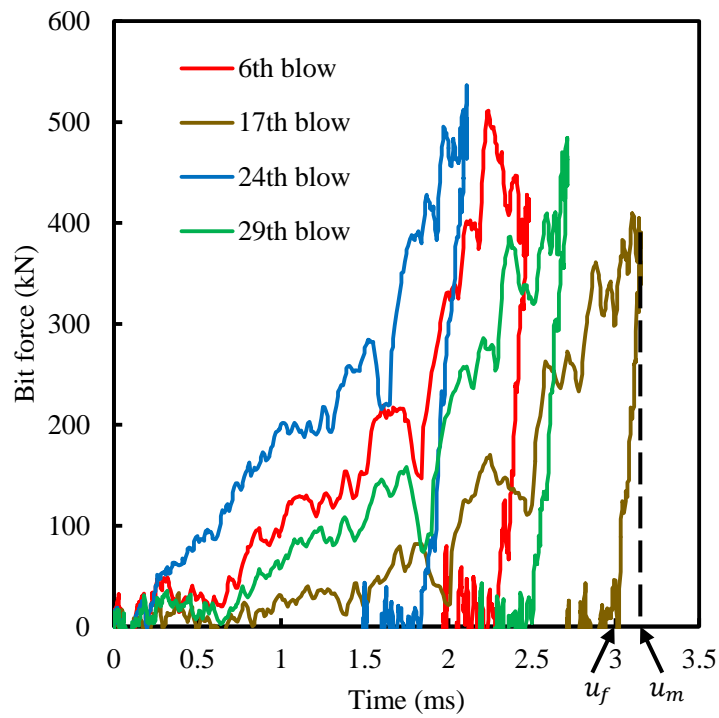


Fig. 5.4 Bit forces and penetrations calculated with the original and simplified models. The original models indicate the ones in Fig. 5.3 (b) and (c). The simplified models indicate the ones in Fig. 5.3 (d) and (e). The rod-bit configuration is T38-64.

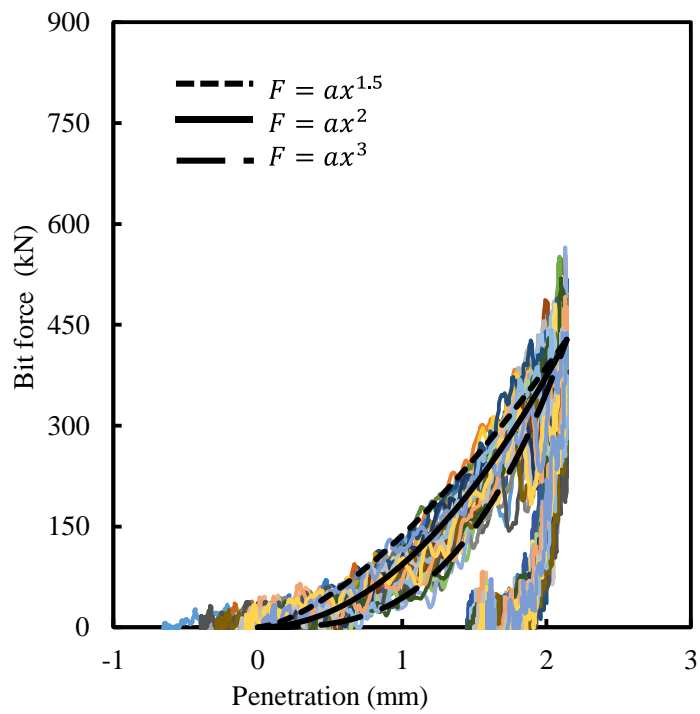


(a)

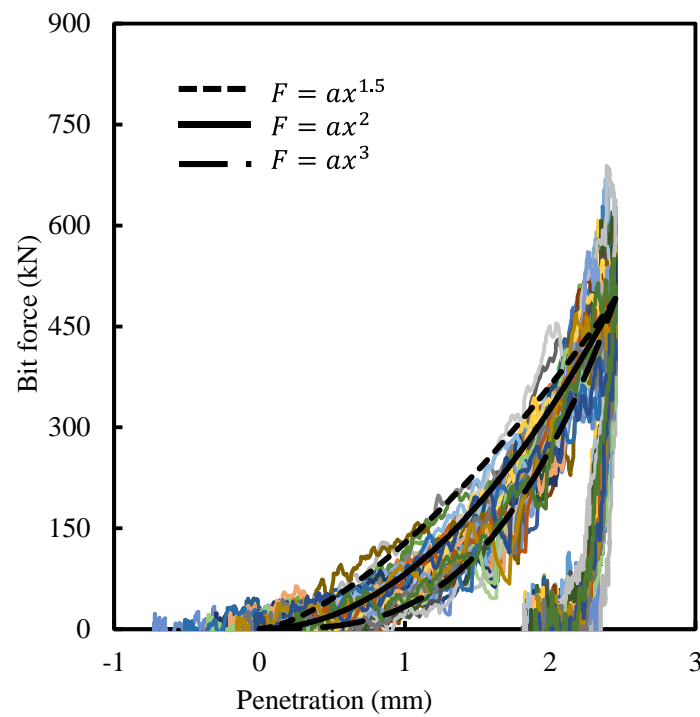


(b)

Fig. 5.5 Representative results with the rod-bit configuration of T38-76. (a) Bit forces. The arrows indicate the abrupt changes of bit forces. (b) Force-penetration curves. u_m and u_f indicate the maximum and final penetrations.

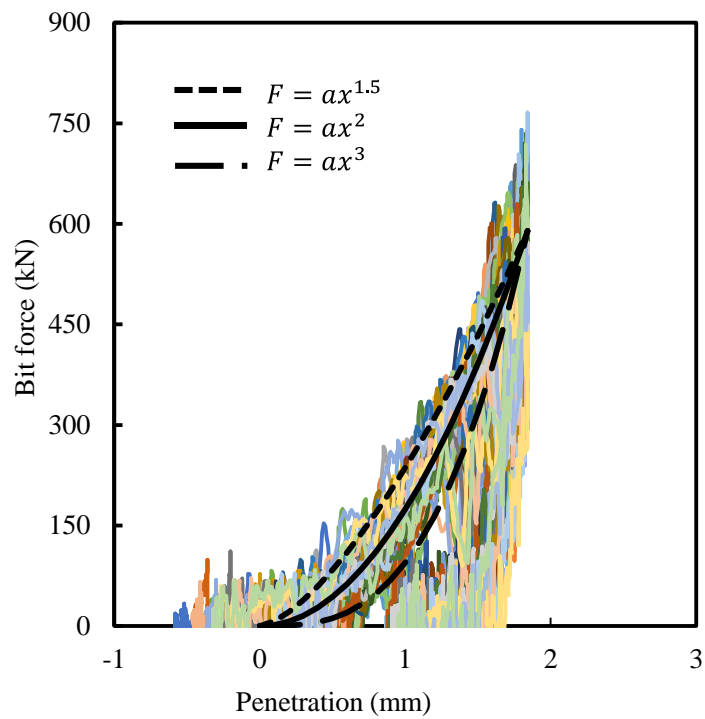


(a)

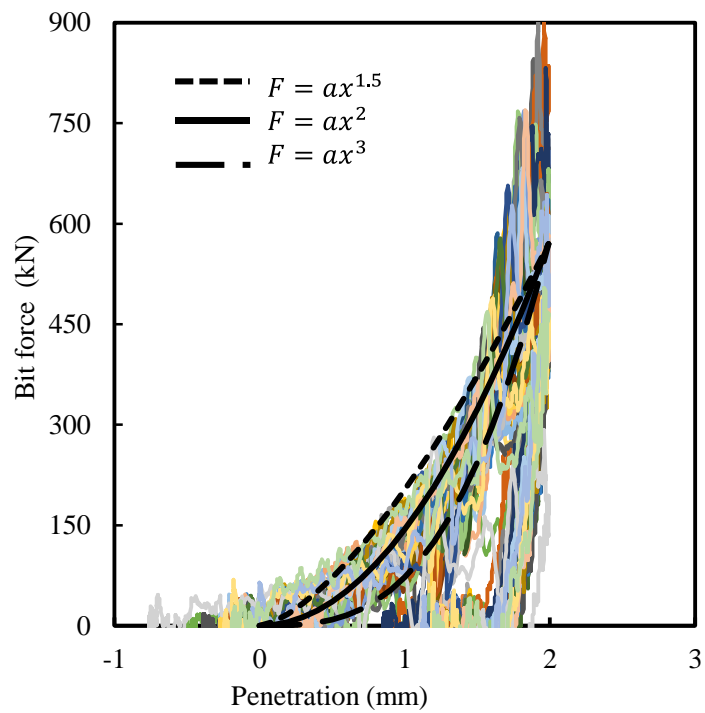


(b)

Fig. 5.6 Force-penetration curves with the four rod-bit configurations. The curves were shifted horizontally so that the maximum penetrations correspond to their mean value. F and x indicate the bit force and penetration, respectively. (a) T38-64. (b) T38-76. (c) T38-89. (d) T45-102.



(c)



(d)

Fig. 5.6 (Continued) Force-penetration curves with the four rod-bit configurations. The curves were shifted horizontally so that the maximum penetrations correspond to their mean value. F and x indicate the bit force and penetration, respectively. (a) T38-64. (b) T38-76. (c) T38-89. (d) T45-102.

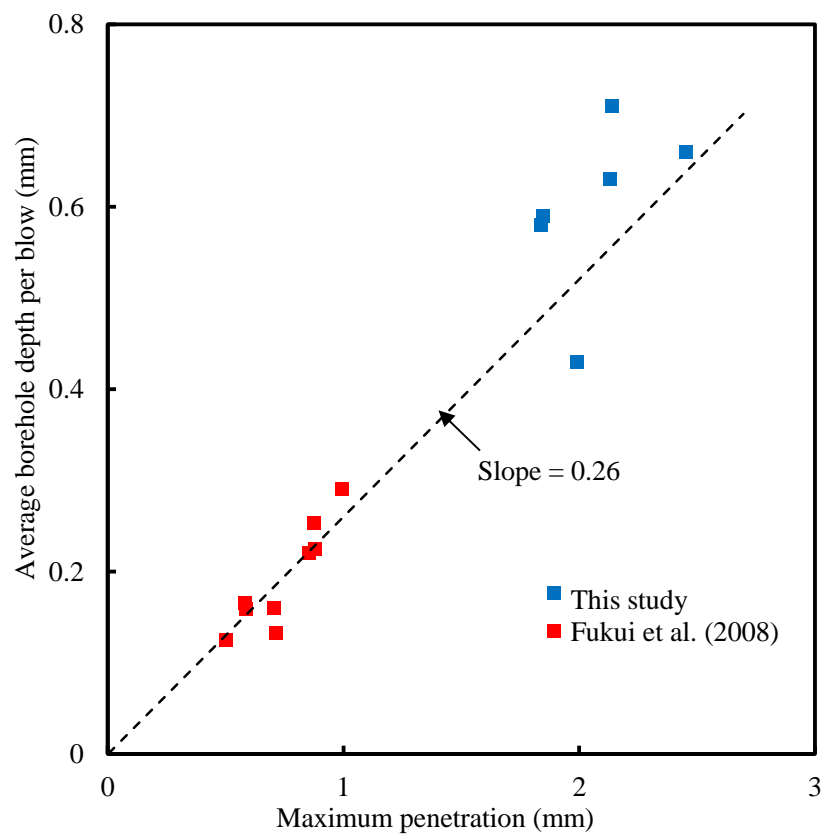


Fig. 5.7 Relation between a and b in Eq. (5.3) derived from the force-penetration curves.

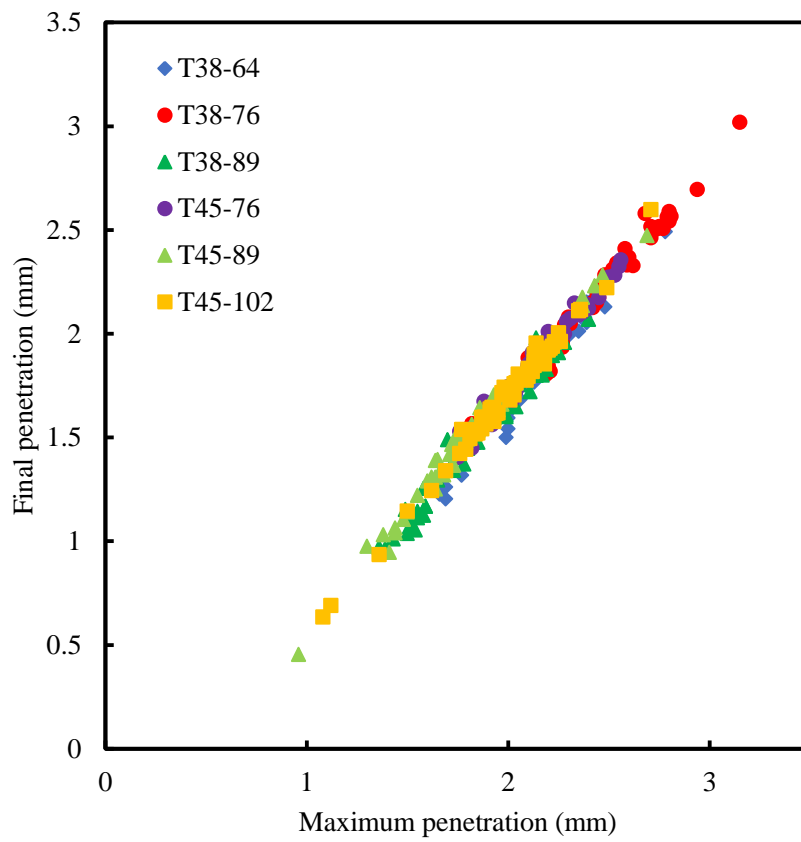


Fig. 5.8 Relation between the maximum and final penetrations obtained from the force-penetration curves for the six rod-bit configurations.

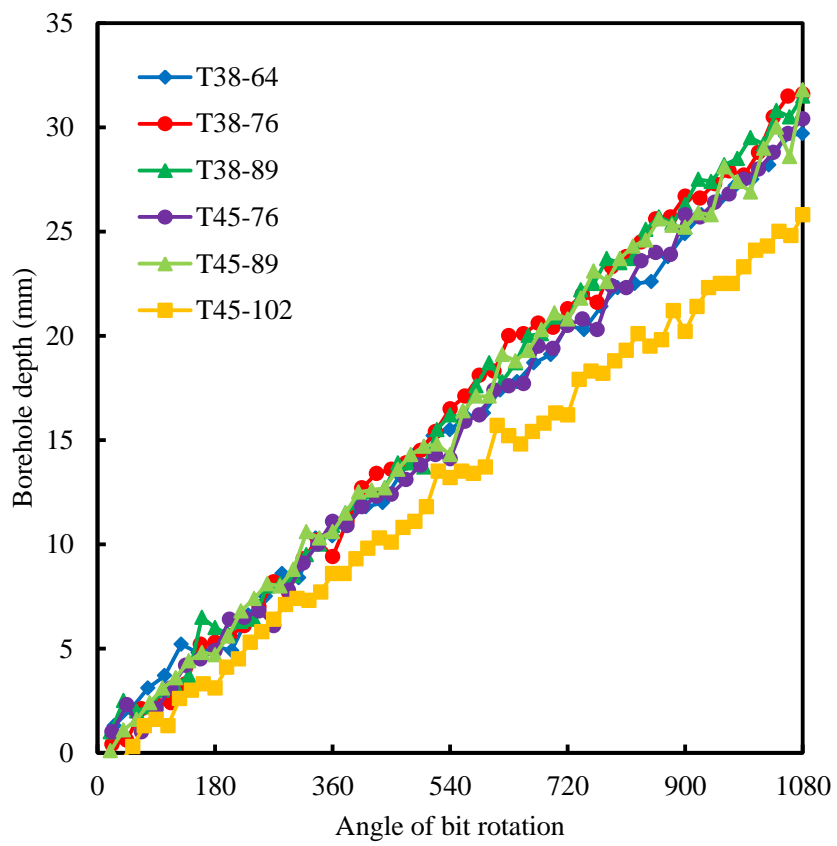


Fig. 5.9 Comparison of borehole depth for the six rod-bit configurations.

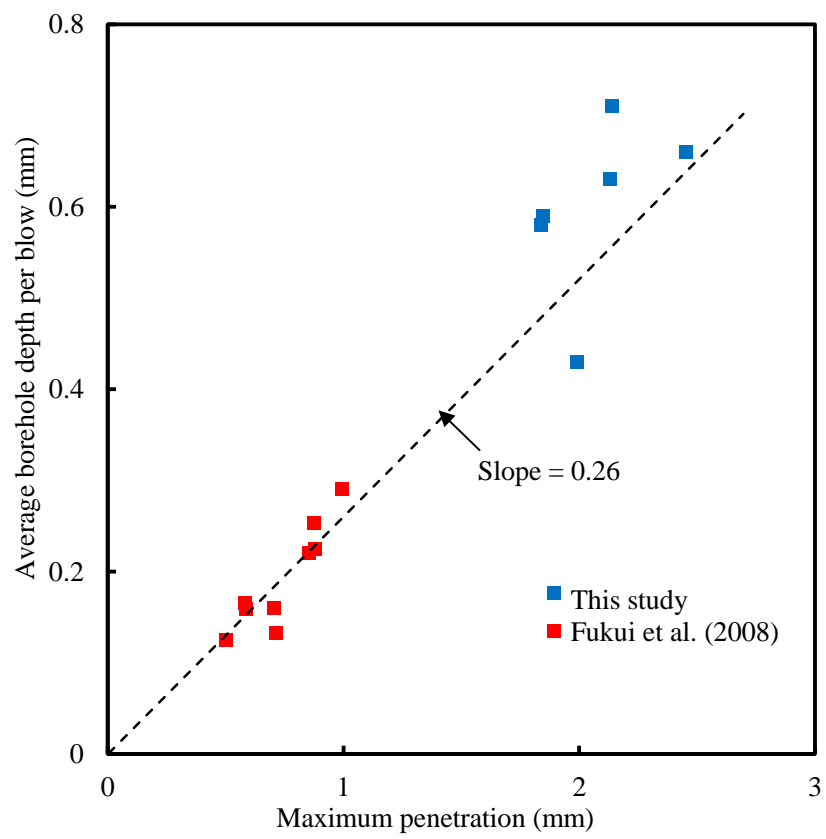


Fig. 5.10 Relationship between the average borehole depth per blow and maximum penetration obtained in Fukui et al. (2008) and this study.

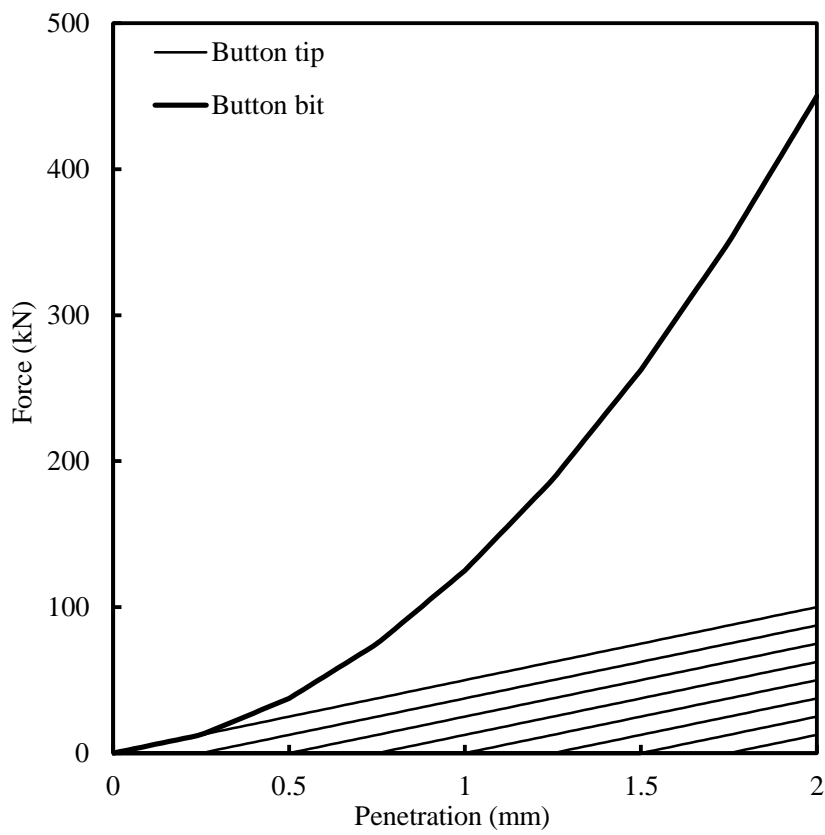


Fig. 5.11 Schematic illustration of force-penetration curves for button tips and a button bit. The thick curve is the sum of the thin curves which show delays due to the contact with rough rock surface.

Chapter 6 Numerical simulation of consecutive percussive drilling

6.1 Introduction

It is necessary to conduct simulation of consecutive percussive drilling for analyzing the long-term response of a hydraulic rock drill under variable drilling conditions. Okubo and Nishimatsu (1991) proposed a comprehensive consecutive percussive drilling model, which is composed of stress wave generation in a rock drill body, wave propagation in a rod and bit penetration into rock. However, there are still many factors and equipment not considered or simplified in comparison with actual rock drills. For example, in the model, the shapes of the piston, the shank rod, the rod and the bit were simplified as circular cylinders with uniform cross-sectional areas; The shank rod, rod and the bit were taken as a whole and the sleeve-type rod joint between the shank rod and the rod and the threaded connection between the rod and the bit were omitted; The bit was set to be always in contact with the rock and the relationship between the penetration and the bit force was not changed with each blow. Hirano et al. (2014) improved the aspects of the Okubo and Nishimatsu's model associated with the rock drill body and the hydraulic circuits within the rock drill body, as well as built a numerical model for the damper system.

The aspects of the model on the stress wave propagation in rods and rod joints as well as the bit-rock interaction were improved in this study based on the results of Chapters 3, 4 and 5. Based on the result of Chapter 3, the acoustic impedances of the piston, shank rod, rod and the bit were set to be consistent with their actual shape and size, and the sleeve-type rod joint was modeled as the CI + spring model. Based on the result of Chapters 4 and 5, the relationship between the force and the penetration during the loading phase in bit-rock interaction was changed from the linear to nonlinear relationship.

In addition, the parameters representing force-penetration curves and the change in the borehole depth with each blow were investigated. In numerical simulation of consecutive percussive drilling, the variation of the force-penetration curves and the change in the borehole depth with each blow were combined into the new numerical model.

6.2 Modeling of consecutive percussive drilling

The aspects of the Okubo-Nishimatsu's model involved in the stress wave propagation and in the bit-rock interaction were improved based on the result of Chapters 3, 4 and 5. The aspects of the model associated with the rock drill

body and the hydraulic circuit within the rock drill body were improved by Hirano et al. (2014). A new consecutive percussive drilling model was implemented with the aid of SimulationX, which is a commercial one-dimensional computer-aided engineering (1D-CAE) software produced by the ITI Company.

6.2.1 Modeling of the rock drill body

As shown in Fig. 6.1, the aspects of the rock drill body and hydraulic circuits within the rock drill body were improved by Hirano et al. (2014) with the aid of SimulationX. The rock drill body consists of a valve, a piston, a damper system, hydraulic circuits, high and low pressure accumulators, pump and tank. The thrust force F_t was applied to the rock drill body through the oil. The detail description with respect to the rock drill body was omitted due to no permission to transfer.

6.2.2 Modeling of the piston

As shown in Fig. 6.2, the stress wave propagation generated by the repeated impact of the piston on the shank rod was calculated based on the 1D theory of elastic waves, which was already introduced in Chapter 3. The piston was divided into L_p segments with the same length of ΔL . The acoustic impedance of the piston was set to be consistent with the actual product. The impact between the piston and the shank rod was considered as the spring model discussed in Chapter 3 and the impact force F_{psr} was applied to the element at the front end of the piston ($i = L_p$) as follows

$$-F_{psr} = p(t - \Delta t, i) + n(t, i) \quad (6.1)$$

The hydraulic force F_{pf} acting on the piston in the front chamber of the piston is applied on the element ($i = L_{pf}$) at the center of the front of the piston. To guarantee the continuity of the displacement at the interface of two adjacent elements, the following equations are established

$$\begin{aligned} p(t, i + 1) &= p(t - \Delta t, i) - 0.5F_{pf} \\ n(t, i) &= n(t - \Delta t, i + 1) + 0.5F_{pf} \end{aligned} \quad (6.2)$$

The hydraulic force F_{pr} acting on the piston in the rear chamber of the piston is applied to the element at the center of the rear of the piston in the same way as the force F_{pf} .

6.2.3 Modeling of the shank rod, rod and the bit

The stress wave propagation in the shank rod, rod and the bit is calculated in

the same way as the piston. The shank rod, rod and the bit were divided into L_{sr} , L_r and L_b segments with the same length of ΔL , respectively. The thrust force F_d from the rock drill body was acted on the back end of the shank rod as follows

$$-(F_{psr} + F_d) = p(t, i) + n(t - \Delta t, i) \quad (6.3)$$

where $i = L_{sr0}$ represents the segment at the back end of the shank rod. The sleeve-type rod joint used to connect the rod to the shank rod was modeled as the CI + spring model which have already discussed in Chapter 3. The force F_{srr} acting between the shank rod and the rod was expressed as

$$F_{srr} = -K_s(u_{rb} - u_{srf}) \quad (6.4)$$

where u_{rb} and u_{srf} are the displacements of the back end of the rod and the front end of the shank rod, respectively. K_s is the spring constant between the shank rod and the rod. The equations of the elements at the front end of the shank rod ($i = L_{sr}$) and at the back end of the rod ($i = L_{r0}$) are as follows with consideration of the attenuation rate β ,

$$\begin{aligned} -F_{srr} &= \beta p(t - \Delta t, i) + n(t, i) \\ -F_{srr} &= p(t, i) + \beta n(t - \Delta t, i) \end{aligned} \quad (6.5)$$

The rod-bit connection was modeled as the spring model. The force acting between the rod and the bit is calculated as follows

$$F_{rb} = -K_{rb}(u_{bb} - u_{rf}) \quad (6.6)$$

where K_{rb} is the spring constant between the rod and the bit. u_{bb} and u_{rf} are displacements of the back end of the bit ($i = L_{b0}$) and the front end of the rod ($i = L_r$), respectively. The front end of the bit ($i = L_b$) received the resistance F_{rock} from the rock.

6.2.4 Modeling of the bit-rock interaction

The relationship between the resistance F_{rock} and the bit penetration u obtained in Chapter 5 was adopted. As shown in Fig. 5.6, the force-penetration curves were convex downward in the loading phase and were linear in the unloading phase, which were expressed as follows

$$F_{rock} = \begin{cases} au^b & \text{for loading} \\ c(u - u_f) & \text{for unloading} \end{cases} \quad (6.7)$$

where a and c are penetration resistances in the loading and unloading phases, respectively. The penetration resistance c can be determined after the maximum bit force F_m , the maximum penetration u_m and the final penetration u_f are known.

$$c = F_m / (u_m - u_f) \quad (6.8)$$

u_f is determined based on the linear relationship between the maximum and final penetrations shown in Fig. 5.8 in Chapter 5.

$$u_f = 1.1u_m - 0.5 \quad (6.9)$$

6.2.5 Modeling of the variation in force-penetration curves with blows

There is a variation in the force-penetration curves with each blow during consecutive percussive drilling, which was because the contact conditions between the button tips and the rock surface varied with each blow. It is necessary to conduct a numerical simulation under variable drilling conditions for performance prediction of a rock drill under actual drilling conditions.

The shape of a force-penetration curve during loading phase is determined by the a and b of Eq. (6.7). Thus, the variation in force-penetration curves can be implemented by varying the a and b . Fig. 6.3 shows the variation of b with each blow. The value of b for each blow was calculated by fitting the Eq. (6.7) to the force-penetration curves obtained from the SBIP tests with the rod-bit configuration of T38-64 conducted by Fukui et al. (2010). Fig. 6.4 shows a normal probability plot of b . The linearity of the plotted data indicates that the b follows a normal distribution with the average μ and standard deviation σ listed in Table 6.1. The probability density $f(b)$ of the normal distribution is as follows

$$f(b) = \frac{1}{\sqrt{2\pi\sigma^2}} \exp\left(-\frac{(b - \mu)^2}{2\sigma^2}\right) \quad (6.10)$$

The cumulative distribution function $F(b)$ of the $f(b)$ is

$$F(b) = \int_{-\infty}^b f(b)db = \int_{-\infty}^u \frac{1}{\sqrt{2\pi}} \exp\left(-\frac{u^2}{2}\right) du = \Phi(u) \quad (6.11a)$$

$$u = \frac{b - \mu}{\sigma} \quad (6.11b)$$

A certain correlation between a and b was observed in Fig.5.7 of Chapter 5. Thus, b is randomly varied following the normal distribution and then a is determined by the correlation between the two parameters.

$$a = \frac{338}{b^2} \quad (6.12)$$

6.2.6 Modeling of the change u_b in the borehole depth with each blow

In consecutive percussive drilling with a rock drill, the borehole depth $\sum u_b$ increased with the increase of the advance of the bit. Fig. 6.6 shows the change u_b in the borehole depth, the maximum penetration u_m and the ratio r of u_b to u_m with each blow. As introduced in Section 2.4.4, the change u_b was the difference in the measured L before and after each blow. Fig. 6.5 illustrates schematic of the bit penetration into the rock with the bit rotation. It can be seen that the change u_b in the borehole depth with each blow is different to the final penetration u_f for each blow due to the bit rotation.

Fig. 6.7 shows a normal probability plot of r . The linearity of the plotted data indicates that the r follows a normal distribution with the average and standard deviation listed in Table 6.1. The probability density $f(r)$ of the normal distribution with the average μ and standard deviation σ is as follows,

$$f(r) = \frac{1}{\sqrt{2\pi\sigma^2}} \exp\left(-\frac{(r - \mu)^2}{2\sigma^2}\right) \quad (6.13)$$

and its cumulative distribution function $F(r)$ is

$$F(r) = \int_{-\infty}^r f(r)dr = \int_{-\infty}^u \frac{1}{\sqrt{2\pi}} \exp\left(-\frac{u^2}{2}\right) du = \Phi(u) \quad (6.14a)$$

$$u = \frac{r - \mu}{\sigma} \quad (6.14b)$$

The non-uniform change in the borehole depth with each blow can be implemented through randomly generating the ratio r based on the normal

distribution with the average and standard deviation listed in Table 6.1.

The retreat u_{back} of the bit is

$$u_{back} = u_f - u_b \quad (6.15)$$

In new calculation, the bit end was set to return to the borehole depth within the time t_{back} with the uniform speed \dot{u}_{back} .

$$\dot{u}_{back} = u_{back}/t_{back} \quad (6.16)$$

6.3 Calculation conditions and procedures

The simulation of consecutive percussive drilling was conducted without and with consideration of the changes in force-penetration curves and the borehole depth with each blow. General conditions are listed in Table 6.2 and the procedure is shown in Fig. 6.8. Chapter 3 pointed out that it is no need to set the time step too small. Therefore, the time step size Δt is 0.5 μ s and the total transient time is 0.2 s. More than 8 blows can be implemented during the 0.2 s. The procedure was repeated until the set time is over. The input and output parameters for each component of the hydraulic percussion rock drill were listed in Table 6.3.

The used rod-bit configuration is T38-64. The extension rod is a hollow cylinder, 3660 mm in length, with outer and inner diameters of 39 mm and 14.5 mm, respectively. The button bit with a nominal diameter of 64 mm has 10 carbide button tips, four of which are face tips and the other eight of which are gauge tips. The rod and the bit were connected to each other with the T38 threads. Fukui et al. (2007) reported that the impact energy almost lost 10 % at a rod joint. The attenuation ratio β at a rod joint was set to 95 % because the energy per blow is in proportion to the square of the rod stress (Beccu et al. 1990).

In the simulation case without consideration of the changes in force-penetration curves and the borehole depth with each blow during consecutive percussive drilling, b and r were set to the average values of 2.13 and 0.26, respectively. In contrast, the changes, b and r varied following normal random distributions in the simulation with consideration of the changes.

6.4 Calculation results

Figs. 6.9 (a) and (b) show simulated force-penetration curves during

consecutive percussive drilling without and with consideration of the changes in the force-penetration curves and the borehole depth with each blow, respectively. In Fig. 6.9 (a), the shape of force-penetration curves is the same but the amplitude of the bit force is slightly different due to the reason that the influence came from the rock drill body. In Fig. 6.9 (b), there exist obvious differences among the force-penetration curves due to the reason that the influence came not only from the rock drill body but also from the bit-rock contact conditions.

Figs. 6.10 (a) and (b) show the position-velocity (p-v) diagram of the piston without and with consideration of the changes in the force-penetration curves and the borehole depth with each blow, respectively. In the figure, points *A*, *B*, *C* and *D* represent the point of impact, the start point of the return stroke and the point of the maximum velocity in return stroke and the end of the return stroke, respectively. The piston accelerated forward from *D* to *A* and impacted on the shank rod at *A*. After the impact of the piston on the shank rod, the velocity of the piston dramatically dropped down, and the piston began to enter into the return stroke from *B*. The piston decelerated with the switch of hydraulic circuit by a valve at *C*. The velocity of the piston decreased to 0 at *A* and began to move forward again. Compared Fig. 6.11 (a) to (b), it can be seen that the piston stroke obviously changed with the variation in the bit-rock contact conditions with each blow.

Figs. 6.12 (a) and (b) show the bit displacements and the borehole depths without and with consideration of the changes in the force-penetration curves and the borehole depth with each blow, respectively. The initial position of the bit was set to be in contact with the rock. In the figures, the blue and red colors in the curve of the bit displacement indicate two contact states of the bit, penetration into rock and separation from the rock, respectively. The curve in green color indicates the borehole depth $\sum u_b$. The black arrows indicate the bit penetration into rock, which is caused by stress waves arriving at the bit. After that, the bit is probably separated from the rock between two adjacent penetrations of the bit because of the resistance from rock and the reflected waves. In general, the thrust force can help the bit to be contact with rock again before the stress waves generated from the next impact of the piston on the shank rod arrive at the bit. In Fig. 6.12 (b), the dashed circle shows that the mechanism failed probably due to the changes in the force-penetration curves and the borehole depth with each blow, which have not appeared in Fig. 6.12 (a). The penetration rates in Figs. 6.12 (a) and (b) are 25 mm/s and 35 mm/s, respectively.

6.5 Conclusions

In this chapter, the aspects of the Okubo-Nishimatsu's model associated to the stress wave propagation in rods and rod joints, and the bit-rock interaction model of consecutive percussive drilling were improved based on the results of Chapters 3, 4 and 5. The model was constructed with the aid of the 1D-CAE software. In particular, the acoustic impedances of the piston, shank rod, rod and bit in the improved model were set to be consistent with their actual shapes, and the rod joint model proposed by Chapter 3 was also added into the model. The relationship between the force and penetration in the bit-rock model was modified from the linear to the nonlinear relationship during the loading phase based on the experimental result of Chapter 5. In order to reproduce the variable bit-rock contact condition during consecutive percussive drilling, the variation of force-penetration curves and the change in the borehole depth with each blow were investigated. It is found that the parameter b representing the convexity varied with each blow following a normal distribution and the ratio r of the change in the borehole depth to the maximum final penetration varied with each blow following a normal distribution.

In the Okubo-Nishimatsu's model, there is no change in the bit-rock contact state because the bit was set to be always in contact with the rock. In the new model, the variation in the force-penetration curve and the change in the borehole depth with each blow were combined into the simulation of the consecutive percussive drilling. It is found that the piston stroke was affected by the variable bit-rock contact condition. In addition, the phenomenon that the bit end was free when the stress waves arrived at the bit appeared in the numerical results with the variable contact condition.

References

Fukui K., Abe H., Koizumi M., Tomosada H., Okubo S. (2007): Attenuation of rod stress in percussive long-hole drilling, J. of MMIJ, vol. 123, pp. 152-157.

Fukui K., Okubo S., Koizumi M., Shioda A., Matsuda T., Fukuda S. (2010): Force-penetration curves with a button bit in the percussive drilling, J. of MMIJ, vol. 126, pp. 512-518.

Hirano E., Koizumi M., Fukui K., Hashiba K: (2014): Performance evaluation of the percussive rock drill with 1D-CAE application, Proceedings of 2014 MMIJ symposium (Kumamoto), A7-14.

Okubo S. and Nishimatsu Y. (1991): Computer simulation of percussive drilling, J. of MMIJ, vol. 107, pp. 209-214.

Table 6.1 Averages and standard deviations of b and r

	Average	Standard deviation
b	2.13	0.57
r	0.34	0.26

Table 6.2 Input and output parameters of each components

Components	Input parameters	Output parameters
Piston	F_{psr}, F_{pf}, F_{pr}	u_{pf}
Shank rod, rod and bit	$u_{pf}, u_{buf}, F_{rock}, u_{back}$	F_{psr}, F_d, u_{bf}
Rock	u_{bf}	F_{rock}, l_{back}

Table 6.3 General conditions

Parameter	Value
Time step size Δt	0.5 μs
Piston	
Number of elements L_p	240
Index L_{pf} of the element applied by the force F_{pf}	100
Index L_{pr} of the element applied by the force F_{pr}	70
mass m_p	6.08 kg
Shank rod	
Number of elements L_{sr}	165
Rod	
Number of elements L_r	1481
Index L_{rm} of the element at the center of the rod	741
Bit	
Number of elements L_b	46
Index L_{rb} of the element applied by the force L_{rb}	34
Spring constants	
Between the piston and shank rod K_{psr}	10 GN/m
Rod joint K_s	1.0 GN/m
Between the rod and the bit K_{rb}	1.6 GN/m
Attenuation rate β	0.95

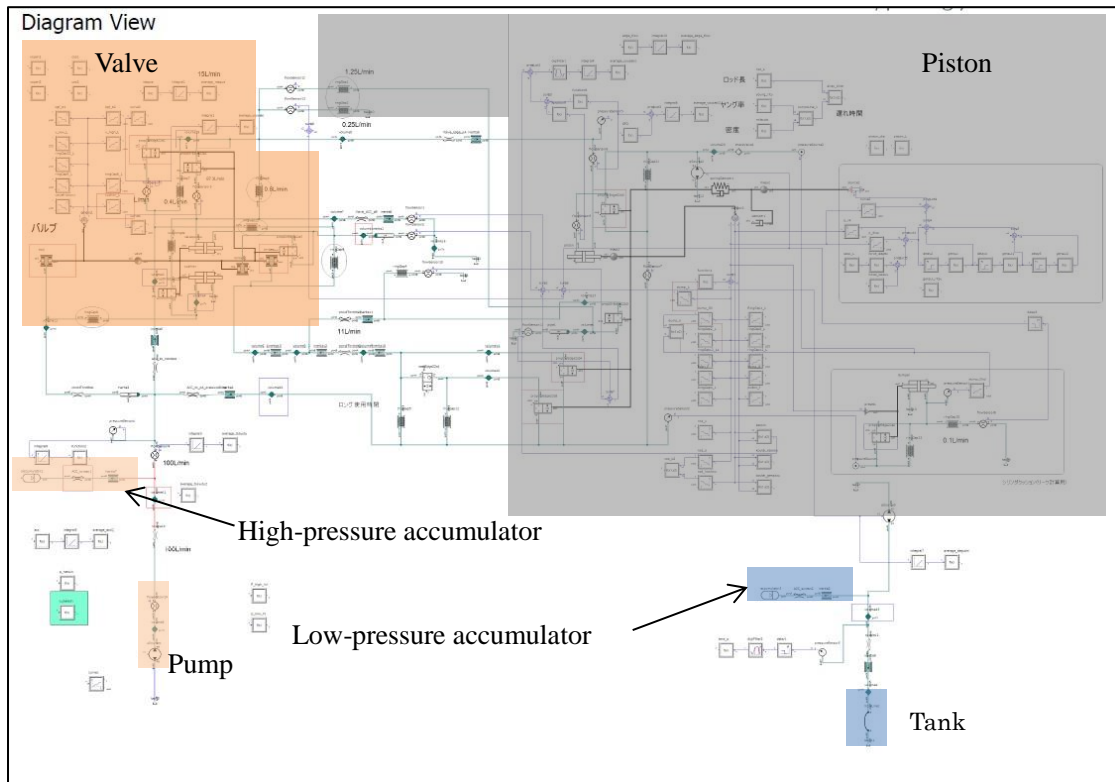


Fig. 6.1 1D-CAE model of the rock drill body (Hirano et al. 2014)

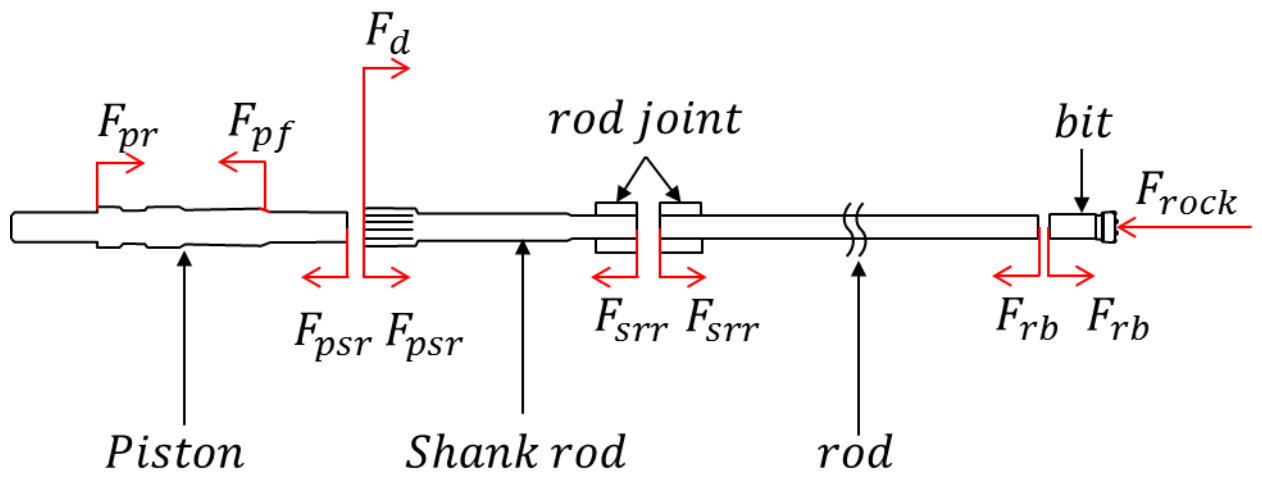


Fig. 6.2 1D-CAE model of components in the percussion system.

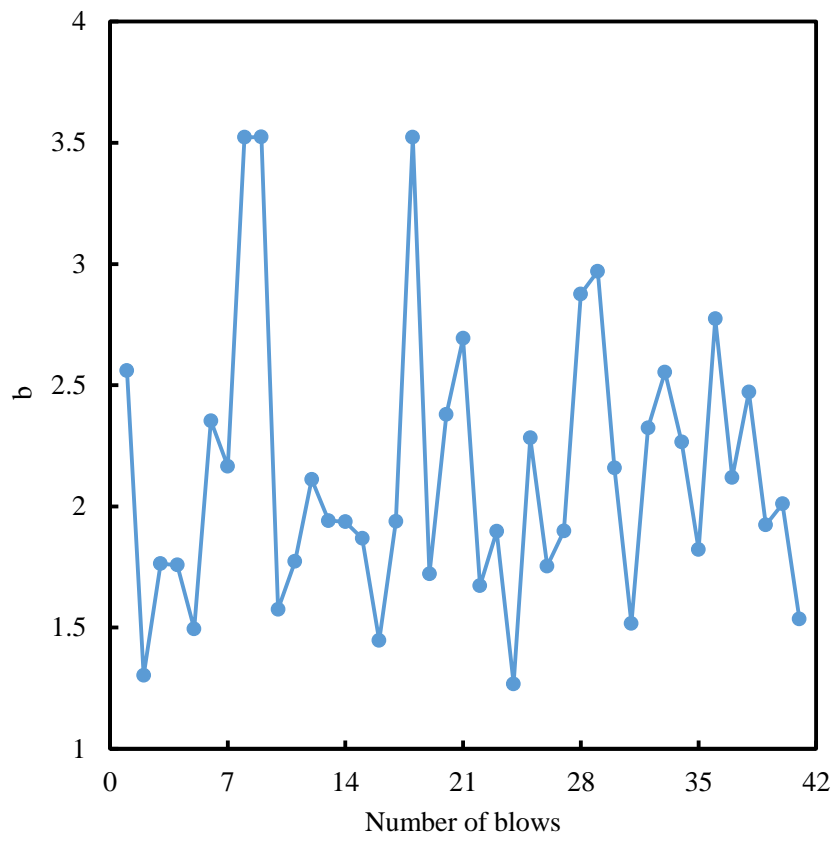


Fig. 6.3 Variation of b with each blow circle.

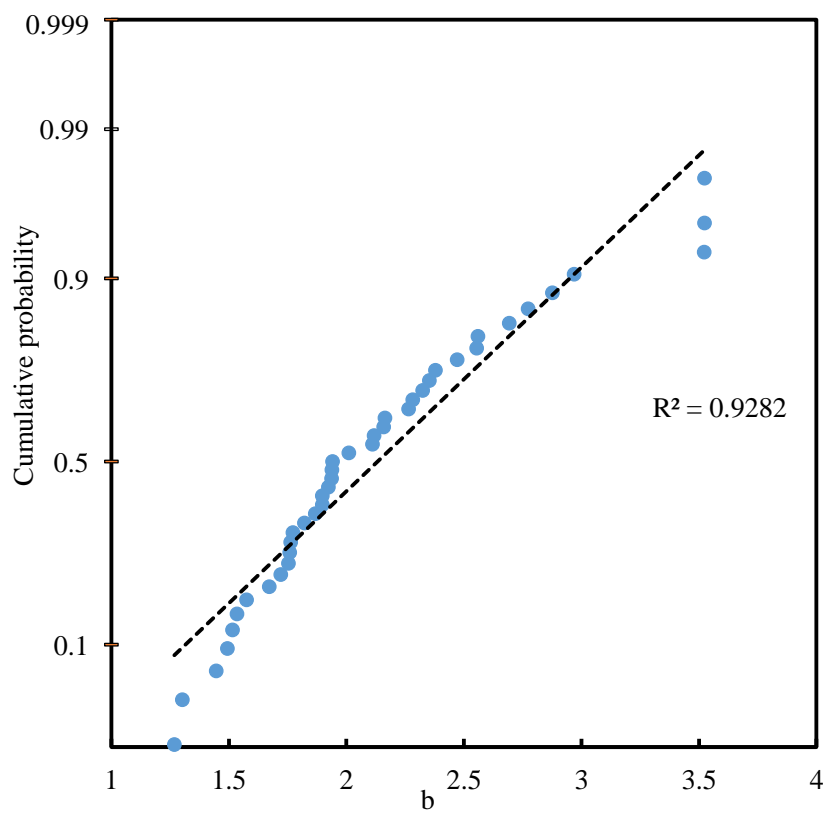


Fig. 6.4 Normal probability plot of b .

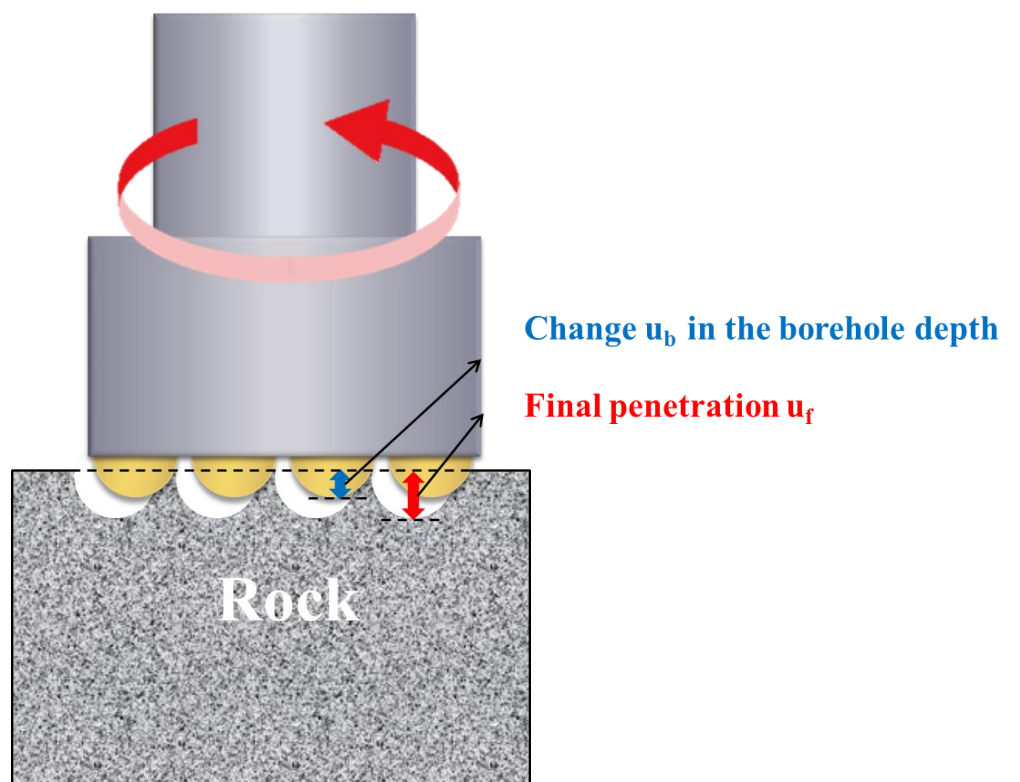


Fig. 6.5 Schematic of a bit-rock interaction with consideration of the bit rotation. The change u_b in the borehole depth and the final penetration u_f are shown with the blue and red double arrows, respectively.

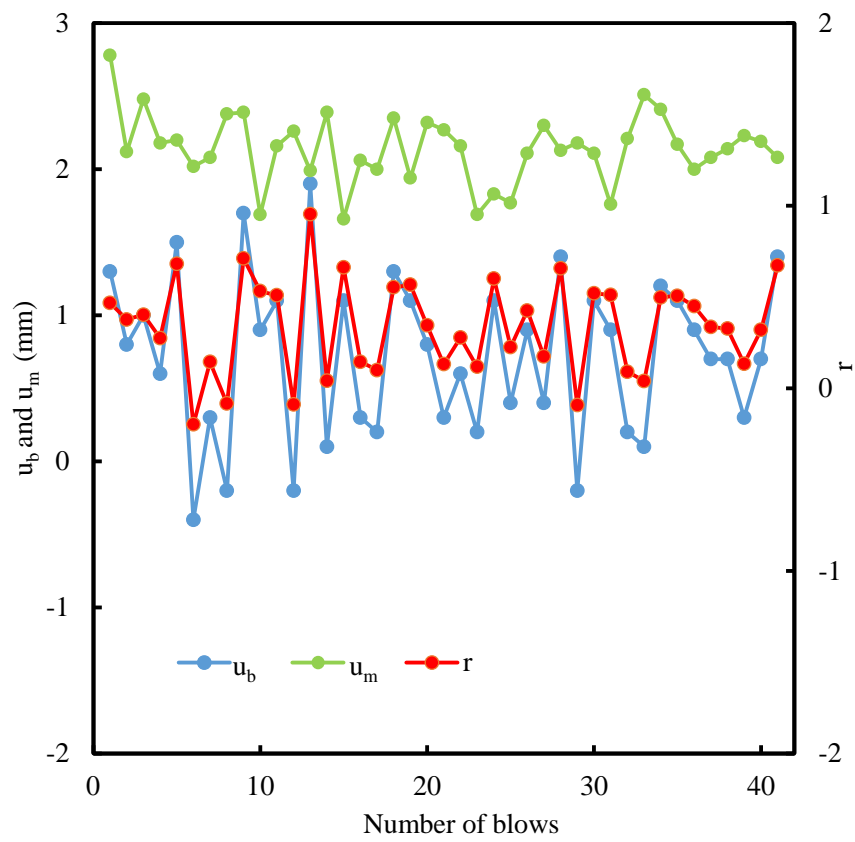


Fig. 6.6 Change u_b in the borehole depth, maximum penetration u_m and the ratio r of u_b to u_m with each blow.

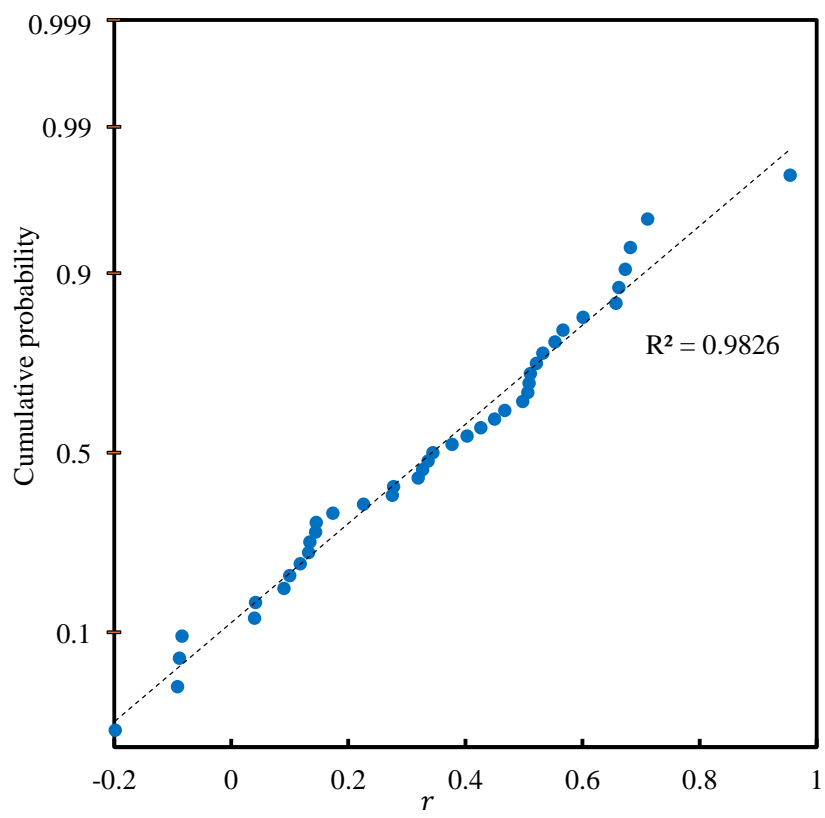


Fig. 6.7 Normal probability plot of r .

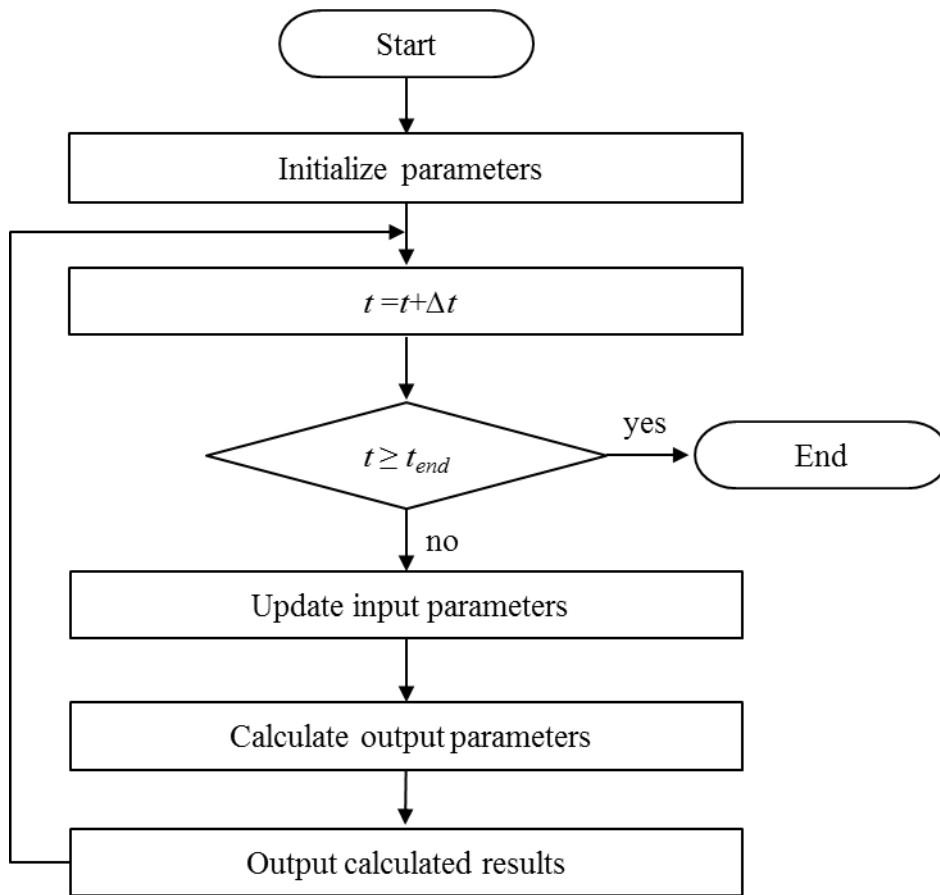
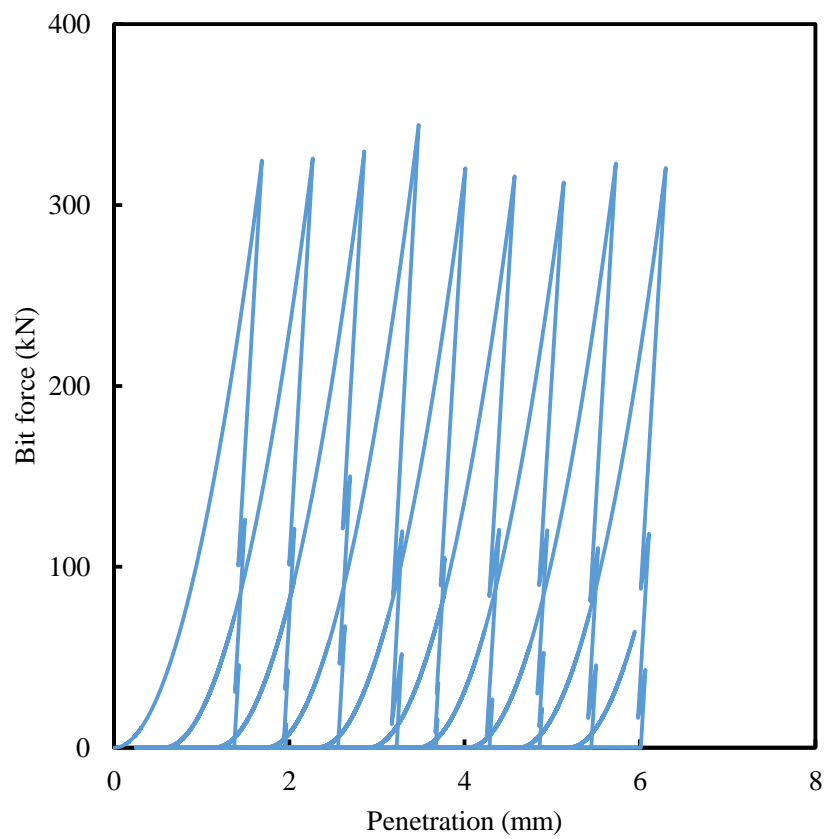
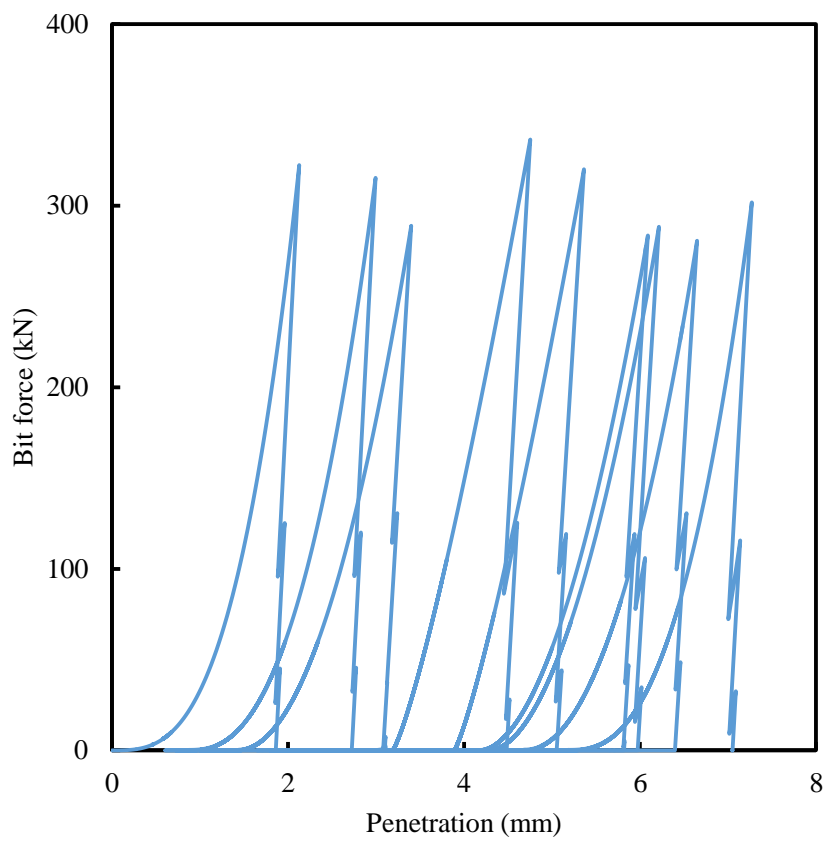


Fig. 6.8 Procedure of calculation for consecutive percussive drilling.



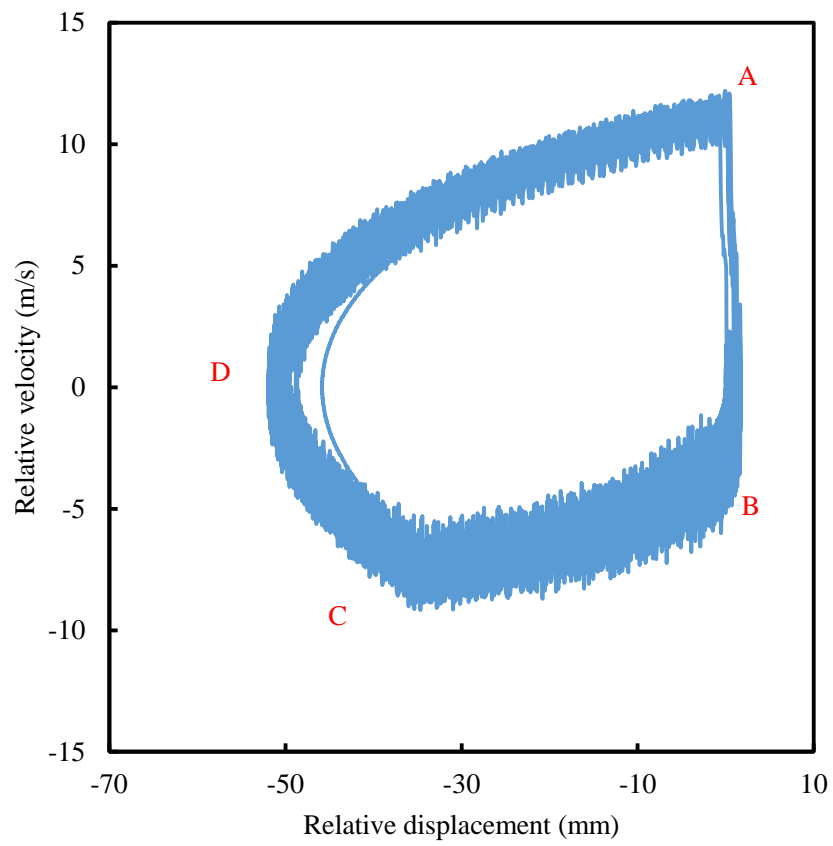
(a)

Fig. 6.9 Simulated force-penetration curves in consecutive percussive drilling (a) without and (b) with consideration of both the variation in the force-penetration curves and the change in the borehole depth with each blow.



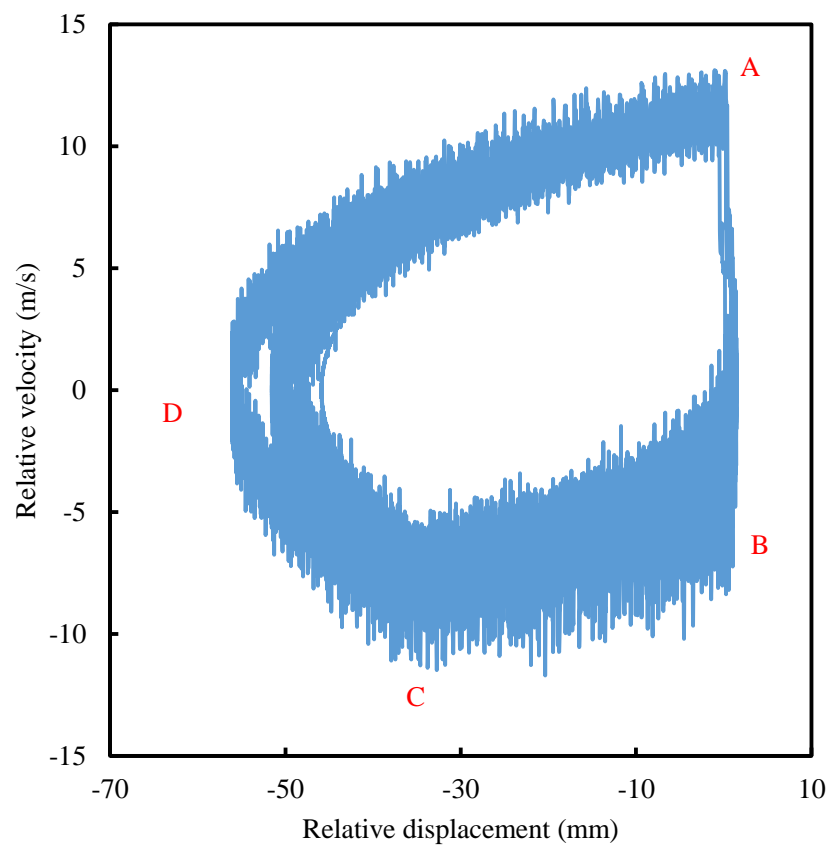
(b)

Fig 6.9 (Continued) Simulated force-penetration curves in consecutive percussive drilling (a) without and (b) with consideration of both the variation in the force-penetration curves and the change in the borehole depth with each blow.



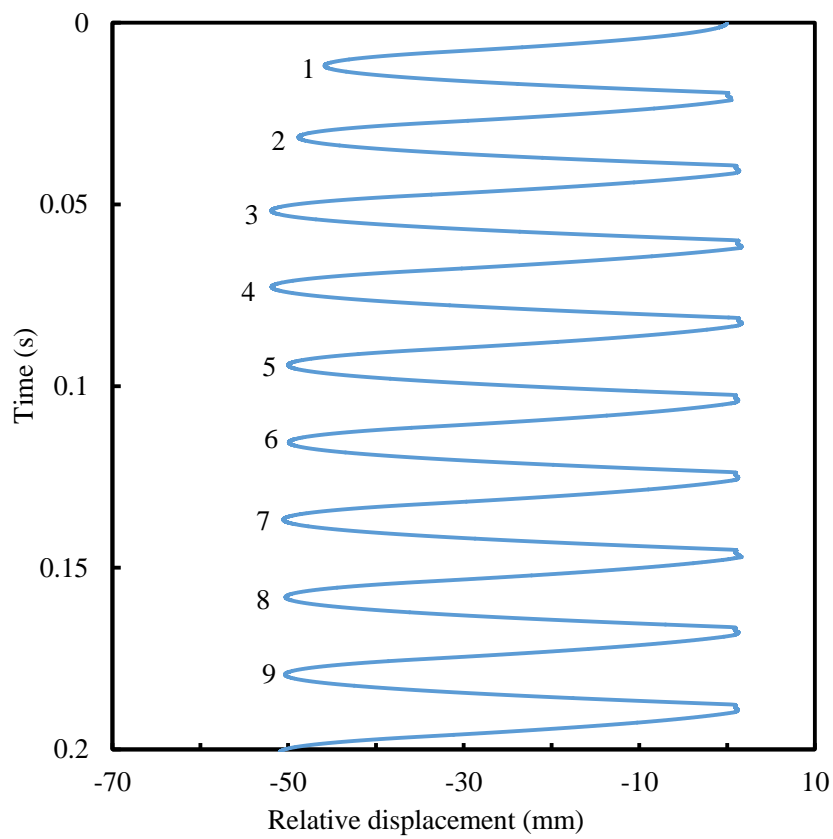
(a)

Fig. 6.10 Simulated p-v diagram of the piston (a) without and (b) with consideration of both the variation in the force-penetration curves and the change in the borehole depth with each blow.



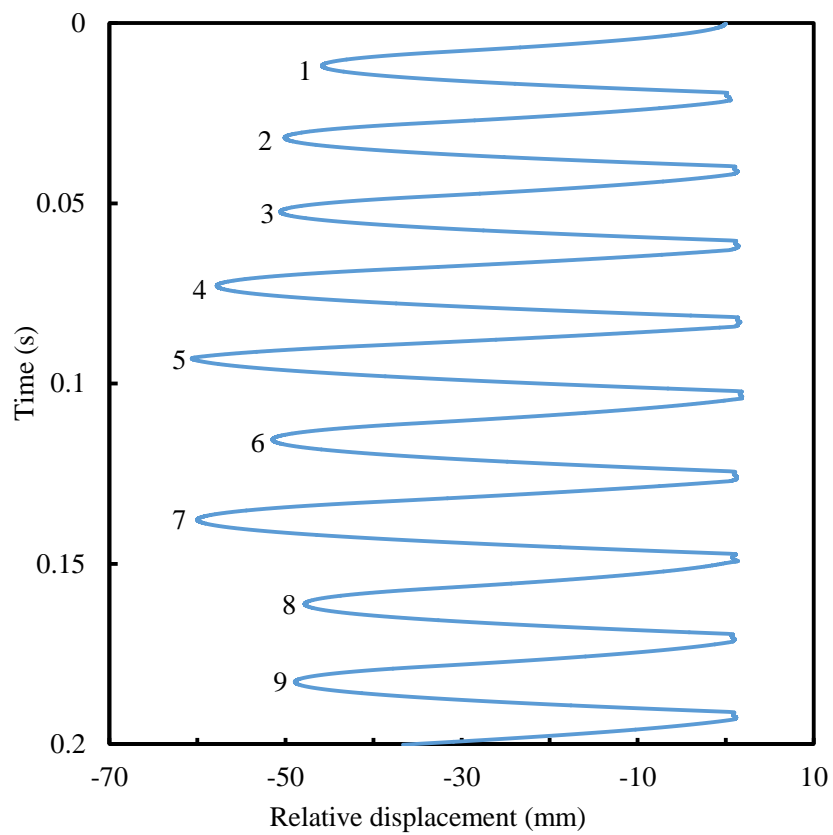
(b)

Fig. 6.10 (Continued) Simulated p-v diagram of the piston (a) without and (b) with consideration of both the variation in the force-penetration curves and the change in the borehole depth with each blow.



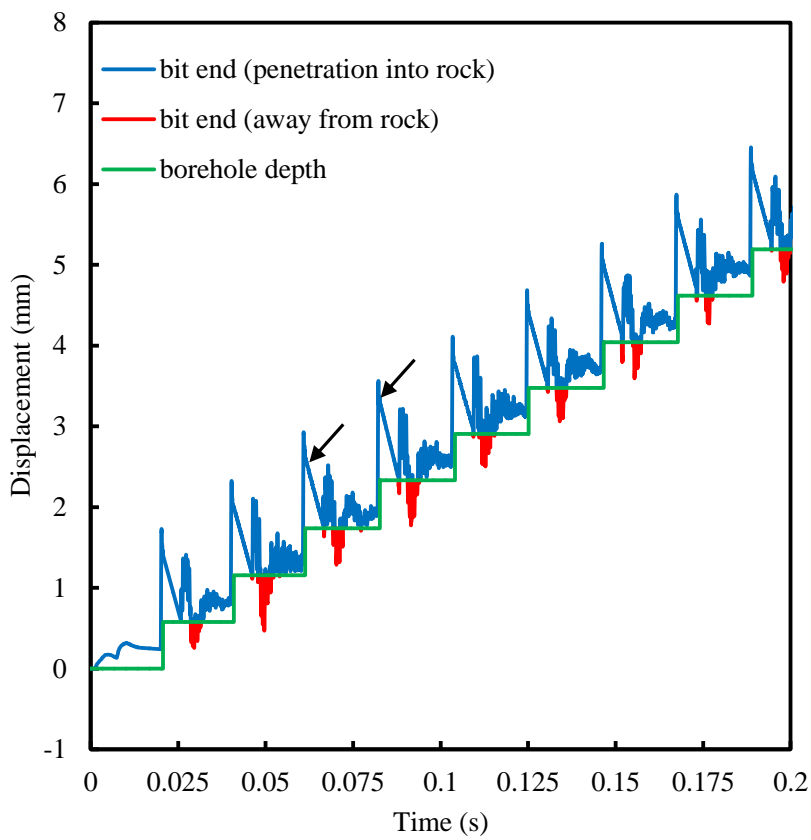
(a)

Fig. 6.11 Simulated piston stroke during consecutive percussive drilling (a) without and (b) with consideration of both the variation in the force-penetration curves and the change in the borehole depth with each blow. The numbers indicate the number of times of reciprocating motion of the piston.



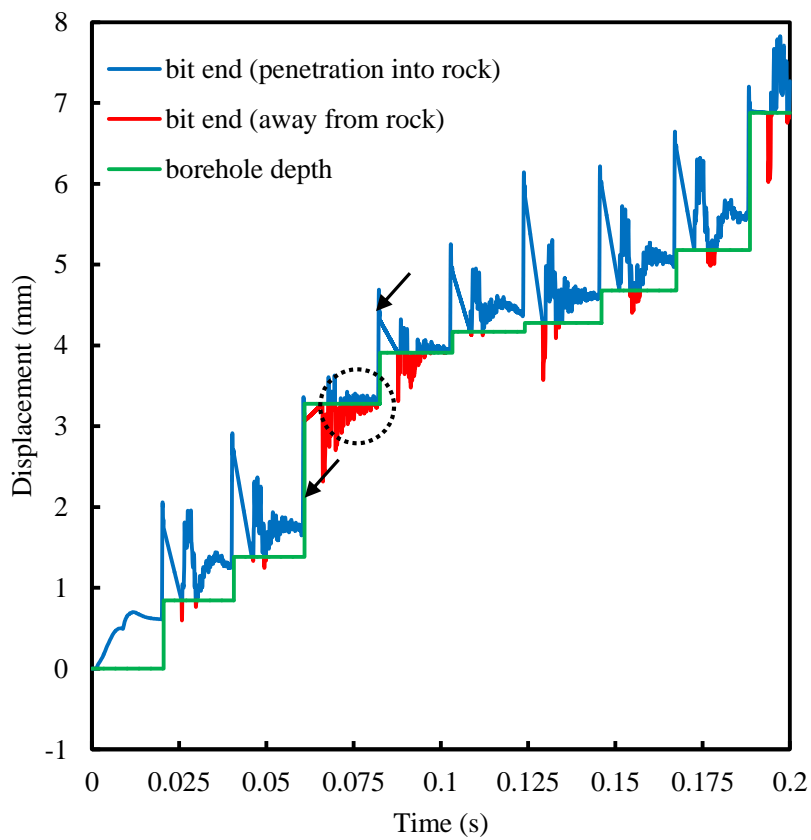
(b)

Fig. 6.11 (Continued) Simulated piston stroke during consecutive percussive drilling (a) without and (b) with consideration of both the variation in the force-penetration curves and the change in the borehole depth with each blow. The numbers indicate the number of times of reciprocating motion of the piston.



(a)

Fig. 6.12 Bit end displacement and borehole depth (a) without and (b) with consideration of both the variation in the force-penetration curves and the change in the borehole depth with each blow. The black arrows indicate the dramatic changes in the bit end displacement caused by the arrival of incident waves, which are generated from the impact of the piston on shank rod. The dashed circle shows the case that the bit is not in contact with rock, even until the next incident waves arrive.



(b)

Fig. 6.12 (Continued) Bit end displacement and borehole depth (a) without and (b) with consideration of both the variation in the force-penetration curves and the change in the borehole depth with each blow. The black arrows indicate the dramatic changes in the bit end displacement caused by the arrival of incident waves, which are generated from the impact of the piston on shank rod. The dashed circle shows the case that the bit is not in contact with rock, even until the next incident waves arrive.

Chapter 7 Conclusions

7.1 Conclusions

The hydraulic percussion rock drill is used in mining, oil and water well drilling and civil engineering, etc. The efficiency and penetration rate of the rock drill significantly affect the speed of construction and cost saving. In tunnel drilling, about 30 percent of the construction time is spent for drilling holes. The total cost consists of labor and various rental costs, which are almost proportional to the time. That is, cost reduction can be achieved by shortening the construction time. However, the drilling process with a hydraulic percussion rock drill is a very complex system which involved many components and interactions among them. The performance and efficiency of the rock drill are affected not only by the factors inside the machine, but also by the drilling conditions outside the machine. In this study, a more accurate numerical model of consecutive percussive drilling was constructed, which can be taken as a tool for performance evaluation and the design optimization of the rock drill. The numerical model was based on the Okubo-Nishimatsu's model and further modified in the aspects of the stress wave propagation in rods and rod joints and the bit-rock interaction. In addition, the variable bit-rock contact condition during consecutive percussive drilling was investigated, modeled and combined into the new model for making the simulation closer to reality.

In Chapter 1, the background, problems existed in the modern hydraulic percussion rock drills, motivations and aims and outline of the study were described. Percussive drilling is an important process involved in mining, oil and water well drilling and civil engineering. The performance and efficiency of the rock drill critically affect the construction speed and the cost. Thus, how to improve the performance by experimental and numerical method has been focused by many researchers.

In Chapter 2, the basic knowledge and previous study concerning the percussive drilling were reviewed. The basic knowledge included the classification of drilling methods, the basic mechanism of the percussive drilling, and experimental and two-point-strain-measurement methods.

In Chapter 3, the aspects of stress wave generation, propagation and attenuation in the Okubo-Nishimatsu's model were improved. The improved model which was based on the 1D theory of elastic waves accurately reproduced the stress waves measured in the drilling tests. In the improved model, the acoustic impedances of the piston, shank rod and rod were set to

be consistent with their actual shape and size, as well as the rod joint was modeled as the CI +spring model. In addition, the 1D and axisymmetric finite element models of percussive drilling were built to calculate stress waves. The numerical waves calculated with these models were compared with the measured waves. It is shown that the numerical results calculated with the axisymmetric finite element model were better than those calculated with 1D theory of elastic waves on reproducing the lateral-inertia effect but they were very close to each other. The numerical results of the axisymmetric finite element models were sensitive to the mesh scale and the time step size. A too small time step did not improve the simulation accuracy, but cause undesirable high-frequency vibrations in numerical results for the coarse-mesh scale. Thus, it is recommended to use the improved model for simulating stress wave propagation, that contribute to decreasing computational complexity and to saving computational time.

In Chapter 4, the impact penetration behavior of the button-bit with the diameter of 64 mm on Inada granite was investigated. Single-blow-impact-penetration (SBIP) tests provided highly reproducible results under constant blow conditions and with tightening of the threads after each blow. Unnatural fluctuations appeared in the force-penetration curves calculated with the two-point-strain-measurement (TPSM) method. This is probably due to not only the differences in the rod stresses measured at the two points on the rod, but also the mismatch between the actual bit and the calculation model. The data correction method was proposed, in which the bit force calculated in the Free-bit-end (FBE) test is subtracted from that in the SBIP test using a numerical simulation. The correction method was applied to the measured rod stresses, and the force-penetration curves were improved remarkably. However, the slopes of the curves changed unnaturally just before the peaks, which was probably due to the change in the contact conditions at the rod-bit connection in the SBIP and FBE tests. Thereafter, the bit force calculated in the simulation of the FBE test was subtracted from the one calculated from the measured rod stresses in the SBIP test when the bit force was high. The additional correction with threaded bit model is just for the threaded rod-bit connection used in this study. The corrected force-penetration curves are smoother in the SBIP tests than those in static penetration tests in previous studies, which indicate that impact penetration is not accompanied by large rock chipping. The variations in the force-penetration curves obtained from the more than 40 SBIP tests are probably caused by the contact conditions between the bit and rock, and the rock properties and the damage to the rock with each blow.

In Chapter 5, the impact penetration behavior of button bits into rock was investigated for modeling the bit-rock interaction under different rod-bit

configurations. Impact penetration tests on Inada granite were carried out with six rod-bit configurations which were composed of four kinds of button bits and two kinds of rods. In the calculation of force-penetration curves based on the measured rod strains, the bit model constructed from the acoustic impedances was simplified, and the empirical data correction method proposed in Chapter 4 was applied to all the rod-bit configurations. The force-penetration curves for the six rod-bit configurations showed that the bit force in loading phase was approximately proportional to the square of the penetration. The curves in unloading phase had a linear relation between the bit force and the penetration. The final penetration of each blow had a linear relation with the maximum penetration, and the measured changes in borehole depth with each blow were proportional to the maximum penetration. The effect of rod diameter on the force-penetration curves was not clearly observed. However, the bit force corresponding to the same penetration increased and the specific energy decreased with the increase in bit diameter or in numbers of button tips on the bit.

In Chapter 6, the new consecutive percussive drilling model which was based on the 1D theory of elastic waves and modified from the Okubo-Nishimatsu's model was proposed. The aspects of the original model involved in stress wave generation, propagation and attenuation, as well as the bit-rock interaction were improved on the basis of the results of Chapters 3, 4 and 5. The variation in the force-penetration curves and the change in the borehole depth with each blow were considered for reproducing the variable bit-rock contact condition during consecutive percussive drilling improvements. Any interest parameters can be constantly monitored and the p-v diagram can be accurately simulated. The new consecutive percussive drilling model makes it possible to evaluate the effect of thrust force and the effectiveness of the damper system on the bit-rock contact condition, because the change in the borehole depth was considered while drilling.

7.2 Future work

The proposed consecutive percussive drilling model in this study still has much room for improvement. For instance, in aspects of the modeling the bit-rock interaction, the effects of the face and gauge tips on the force-penetration curve have not been clarified and the quantitative relationship between the number of the button tips and the shape of force-penetration curve has not been given. In addition, the experimental data were only measured from the impact penetration tests on Inada granite. The impact penetration behavior of button bits on other types of rock is unknown. In future work, the impact penetration tests of button bits on other types of rock are necessary to improve the model.

The damper system has appeared in the new series of the hydraulic percussion rock drills produced by Furukawa Rock Drill Co. Ltd. However, the effectiveness of the damper system on the bit-rock interaction have not been verified in theory. In this study, the variation in the force-penetration curves and the change in the borehole depth have been combined into the new model, which makes it possible to investigate the effectiveness of the damper system on the bit-rock interaction during consecutive percussive drilling. In future work, the effect of the damper system on the drilling performance should be examined.

The hydraulic percussion rock drills are now used to drill holes with the diameter less than 150 mm. The drill-supplier plans to make the next generation of rock drills suitable for drilling large-diameter holes. It is necessary to conduct numerical simulation to predict and evaluate the performance of a rock drill when it drills large-diameter holes before making a prototype.

There are two ways to increase the power of a rock drill. One is to increase the energy per blow. However, the size of the energy per blow is limited by the strength of each component. The other is to increase the blow frequency. But the blow frequency is affected not only by the components inside the rock drill, but also by the drilling conditions outside the machine. Thus, in future work, more simulations of consecutive percussive drilling under different drilling conditions will be conducted to find a suitable way to increase the blow frequency.

Through improving the precision of partial models, the precision of the integrated consecutive percussive drilling model will be increased step by step. Finally, the numerical model can be used as an effective tool to evaluate the performance and efficiency of different rock drills and to guide the production optimization.